

***Mullite Whisker Enhanced Zirconia Toughened Alumina Ceramic
Matrix Composite for High Temperature Applications***

by

Taylor Robertson

A thesis submitted to the Faculty of Graduate and Postdoctoral Affairs in partial fulfillment
of the requirements for the degree of

Master of Applied Science

in

Materials Engineering

Carleton University

Ottawa, Ontario

©2014

Taylor Robertson

***Mullite Whisker Enhanced Zirconia Toughened Alumina Ceramic
Matrix Composite for High Temperature Applications***

by

Taylor Robertson

A thesis submitted to the Faculty of Graduate and Postdoctoral Affairs in partial fulfillment
of the requirements for the degree of

Master of Applied Science

in

Materials Engineering

Professor Xiao Huang, Thesis Supervisor

Dr. Rick Kearsy, Thesis Co-Supervisor

Professor Metin I. Yaras, Chair, Department of Mechanical and Aerospace Engineering

Abstract

Ceramic Matrix Composites (CMC) are an attractive material for high temperature applications because they possess many of the high temperature capabilities of monolithic ceramics but also have enhanced mechanical properties due to their multi-phase structure. Recent successes with incorporating SiC fibre reinforced high temperature CMCs into advanced gas turbines have caused a renewed interest in applying CMCs to other high temperature applications. In this work, an oxide based CMC is proposed as a more oxidation resistant and cost effective CMC. Zirconia Toughened Alumina (ZTA), as the matrix, has enhanced toughness, strength, and creep resistance over single phase alumina or zirconia. ZTA can further be enhanced by the incorporation of single crystal mullite whiskers due to their stability in oxidizing atmospheres at high temperatures. Mullite whiskers are grown through the molten salt method and incorporated into the ZTA matrix using a colloidal processing route. The composition of the ZTA matrix is 15 wt% yttria stabilized zirconia (YSZ), 85 wt% α -alumina. The mullite whiskers make up 20 vol% of the composite, yielding a final composition of 71.6 wt% α -alumina, 12.7 wt% YSZ, and 15.6 wt% mullite. The green compacts are fired in a two stage sintering process incorporating atmospheric pressure sintering to 92% density (to seal the pore channels) and then hot isostatic pressure sintering to full density. The mechanical test results show that baseline ZTA (ZTA_n) with final porosity of 13.2% has a flexural strength of 61.71 ± 0.99 MPa at room temperature and 52.34 ± 15.72 MPa at 1200°C, a fracture toughness of 5.02 ± 0.21 MPa·m^{1/2} and a hardness of 10.73 GPa. ZTA with whisker content (ZTA_w) with final porosity of 3.31% reached a flexural strength of 135.76 ± 1.30 MPa at room temperature, 80.52 ± 13.18 MPa at 1200 °C, a fracture toughness of 8.74 ± 0.24 MPa·m^{1/2} and a hardness of 11.99 GPa. The addition of whiskers to ZTA has improved room temperature flexural strength by 120.0%, flexural strength at 1200°C by 53.8%, fracture toughness by 74.1%; but the whiskers have little effect on the hardness. Although high temperature flexural strength was improved by the addition of whiskers, the

improvement to strength at high temperature was not as significant in ZTA_w. Degradation of large whiskers was found during cyclic oxidation of ZTA_w 1200 °C.

Acknowledgements

I would like to thank several people, without whom, this thesis wouldn't be complete. Foremost I would like to thank my supervisor Dr. Xiao Huang for her guidance, her patience and her unending support throughout my studies as well as providing the financial support which made this project possible. I would also like to thank my NRC supervisor Dr. Richard Kearsley for guiding me through the policies and procedures of the NRC, for all the help he provided at a moment's notice, and for his mentorship over the last two years.

At Carleton I would like to thank Fred Barrett and Steve Truttmann for their assistance with the learning and accessing the equipment I needed on campus. At the NRC I would like to thank Olga Lupandina, Ryan MacNeil, Luc Lafluer, and Rolf Floren for their assistance with the facilities, procedures and acting as a ready source of advice. I would also like to thank Dr. Qi Yang for providing assistance with the XRD scanner and giving me greater insight into its operation.

Finally, I would like to thank my family and friends for their love and counsel, and Erin Larkin for keeping me in a good humour as much as is possible during research.

Table of Contents

Abstract.....	iii
Acknowledgements.....	v
Table of Contents.....	vi
List of Figures.....	ix
List of Tables.....	xv
List of Symbols.....	xvi
List of Abbreviations.....	xviii
1.0 Introduction.....	1
2.0 Review of Literature.....	4
2.1 Gas Turbines.....	4
2.1.1 Evolution of High Temperature Section Materials.....	6
2.2 Desired Properties.....	8
2.2.1 Strength.....	8
2.2.2 Toughness.....	14
2.2.3 Corrosion and Oxidation Resistance.....	18
2.2.4 Creep Resistance.....	19
2.2.5 Fatigue Resistance.....	22
2.2.6 Thermal Shock and Thermal Fatigue Resistance.....	24
2.2.7 Statistical Analysis of properties.....	26

2.3 Composites.....	27
2.3.1 CFCCs.....	27
2.3.2 Discontinuous CMCs	43
2.3.3 Ceramic Matrix.....	49
2.3.4 Whiskers.....	54
2.4 Processing	57
2.4.1 Colloidal Mixture.....	57
2.4.2 Whisker Growth	61
2.4.3 Sintering	63
3. 0 Summary and Thesis Objectives	73
4.0 Materials and Experimental Procedures.....	75
4.1 Materials Selection	75
4.2 Molten Salt Method (MSM) Whisker Growth	75
4.3 Slurry Preparation and Consolidation.....	78
4.4 Sintering	79
4.5 Characterization.....	83
4.5.1 Powder Characterization	83
4.5.2 Microstructure of Sintered Samples	87
4.6 Room Temperature Testing	89
4.6.1 Strength.....	89

4.6.2 Fracture Toughness.....	90
4.7 High Temperature Testing	92
4.7.1 Strength.....	92
4.8 Cyclic Testing.....	93
5.0 Results and Discussion	95
5.1 Powder Characterization	95
5.1.1 Whisker Characterization.....	103
5.2 Microstructure of Sintered Samples	107
5.2.1 Porosity	107
5.2.2 Grain Size and Orientation.....	110
5.2.3 Crystal Structures of the Phases	115
5.2.4 EDS analysis results	122
5.3 Room Temperature Mechanical Properties.....	124
5.3.1 Room Temperature Flexural Strength of the Composites.....	125
5.3.2 Microhardness and Fracture Toughness of the Composites at Room Temperature	128
5.4 High Temperature Mechanical Properties.....	132
5.4.1 High Temperature Strength of the Composites.....	132
5.4.2 Thermal Cycling and Oxidation Resistance	134
6.0 Conclusion.....	148
7.0 Future Work	150

8.0 References	152
----------------------	-----

List of Figures

Figure 1: Overall cycle efficiency for simple cycle gas turbine [5]	1
Figure 2: Improvements to firing temperature of gas turbines through materials and cooling system engineering [5]	2
Figure 3: Ideal Brayton Cycle [12]	4
Figure 4: Improvements in firing temperatures of gas turbines [5]	5
Figure 5: Comparison of the development of aerospace and industrial gas turbine alloys [6].....	7
Figure 6: Strain vs. time showcasing the three regions of creep [12]	19
Figure 7: Strength of alumina-mullite-zirconia composites with various wt% SiC additions after 1 cycle thermal shock test	25
Figure 8: Bimodal particle distribution within an oxide/oxide CMC to ensure porosity [73].....	30
Figure 9: Basic electrophoretic deposition set up [74]	31
Figure 10: Cross section of WHIPOX oxide ceramic illustrating fibres, bimodal distribution of particles and porosity [76].....	32
Figure 11: WHIPOX winding steps, equipment above simplified representation below [75]	32
Figure 12: Relative fracture energies of interface to fibres vs. relative young's modulus of fibre to matrix and ductile brittle transition line [78].....	34
Figure 13: SEM image of melt infiltrated SiC/SiC CMC illustrating fibre coating [9]	36
Figure 14: SiC/SiC baseline production method adapted by NASA for their high temperature CMC program [81]	37

Figure 15: Production routes of GE's HiPerComp™ MI CMC, dark grey path is prepeg process and light grey is slurry cast [9] 38

Figure 16: Oxidation of B₄C phase forming a B₂O₃ oxide plug [83]..... 39

Figure 17: Alternating layers of SiC and B₄C self-healing matrix deposited through CVI [84]..... 40

Figure 18: Self-healing mechanism of Si-B-C, B₄C, SiC CMC Step 0) microcracks develop in the matrix Step 1) Oxygen and moisture ingress leads to the formation of oxides Step 2) oxide plug grows and fills the crack Step 3) crack is sealed by the oxide, there is high dissolving of the SiC fibre [85]..... 41

Figure 19: Different weaves of CMC fibre: tubes on the left exhibit 1D wound fibre, the tubes on the right exhibit a 2D braided weave structure [90]..... 43

Figure 20: Crack deflection along a multi layered interface [91]..... 44

Figure 21: Crack bowing: 1. crack approaches stiff inclusion. 2. extra crack energy is absorbed as the crack length increases while bowing around stiff inclusion. 3a. crack continues past inclusion by propagating cracks ahead of the inclusion and joining them. 3b. crack continues past inclusion by shearing it. 4. crack continues 47

Figure 22: Fibre pullout and crack bridging toughening mechanisms in CMCs [21] 47

Figure 23: Fracture toughness and strength of alumina matrix containing I) 0.30 μm II) 1.25 μm unstabilized zirconia particles as a function of the volume fraction of zirconia additions [54] [109]..... 52

Figure 24: Vol % inclusion of ZrO₂ in Al₂O₃ matrix plotted against a) strength and b) toughness [54] 53

Figure 25: a) Standard mullite structure b) mullite structure arranged around an oxygen vacancy [121] 55

Figure 26: Binary Phase Diagram of alumina-silica System [122] 56

Figure 27: Organic structure of Dextrin [126]..... 59

Figure 28: Zeta potential of ZTA mixture in aqueous solution with Dextrin as a dispersant [126] 59

Figure 29: Differential thermal analysis of Al₂(SO₄)₃, SiO₂, Na₂SO₄ in ratio 2:1:8 (S₁₂) and Al(OH)₃, SiO₂, Na₂SO₄ in ratio 2:1:8 (S₂₂) [130] 62

Figure 30: Thermo gravimetric analysis of $\text{Al}_2(\text{SO}_4)_3$, SiO_2 , Na_2SO_4 in ratio 2:1:8 (S_{12}) and $\text{Al}(\text{OH})_3$, SiO_2 , Na_2SO_4 in ratio 2:1:8 (S_{22}) [130]	62
Figure 31: Formation of mullite whiskers through MSM [131]	63
Figure 32: Alumina matrix reinforced with SiC whiskers with evidence of particulate contamination within the matrix [132]	64
Figure 33: ATZ reinforced with alumina whiskers [133]	65
Figure 34: Graphical representation of a computer algorithm used to estimate the 2D packing factor of whiskers within a matrix [134].....	65
Figure 35: Master sintering curve of 8% Ytria partially stabilized ZrO_2	70
Figure 36: Heating profile for MSM	76
Figure 37: Filter system used to remove liquid slurry and salt solution. As water runs through the aspirator on the right a vacuum is formed within the beacon to assist with filtering	77
Figure 38: Batch of filtered whiskers before ultrasonic treatment	78
Figure 39: Pressed green compact prior to sintering with diameter of 76.2 mm	79
Figure 40: (a) Original sinter profile for ZTA_n and ZTA_w (b) ZTA_n sample after sinter profile 1, with black carbon residue patches.....	81
Figure 41: Final sinter profile for ZTA_n and ZTA_w	82
Figure 42: ZTA powder color distribution and conversion to black and white for ZrO_2 particle size analysis	84
Figure 43: Outlines of particles counted for particle size analysis	85
Figure 44: a) line drawn on SEM image of ZTA and b) corresponding line plot of shading intensity where valleys occur at grain boundaries and peaks at zirconia grains.....	86
Figure 45: 3-point bending rig for room temperature flexural testing.....	89
Figure 46: Theoretical crack shape caused by a micro indentation [153]	91

Figure 47: High temperature 3-point bending fixture and surrounding furnace	93
Figure 48: Cyclic thermal test equipment a) samples cycling from the furnace, heat shield intact b) heat shield open showing samples on porous alumina slab.....	94
Figure 49: 85 wt.% Al ₂ O ₃ powder and 15 wt.% ZrO ₂ powder prior to ball milling. Zirconia agglomerates are circled in yellow	95
Figure 50: 85 wt% Al ₂ O ₃ powder and 15 wt% ZrO ₂ powder after 1 hour of ball milling.....	96
Figure 51: 85 wt% Al ₂ O ₃ powder and 15 wt% ZrO ₂ powder after 2 hours of ball milling.....	96
Figure 52: 85 wt.% Al ₂ O ₃ powder and 15 wt.% ZrO ₂ powder after 2 hours of ball milling shown with a color distribution to highlight the two phases (blue=alumina and yellow=zirconia black/grey=background)	97
Figure 53: 85 wt.% Al ₂ O ₃ powder and 15 wt.% ZrO ₂ powder after 8 hours of ball milling.....	97
Figure 54: 85 wt.% Al ₂ O ₃ powder and 15 wt.% ZrO ₂ powder after 8 hours of ball milling shown with a color distribution to highlight the two phases (blue =alumina, yellow=zirconia, black=background).....	98
Figure 55: Cumulative mass percentage vs. diameter size for Al ₂ O ₃ particles	100
Figure 56: Cumulative mass percentage vs. diameter size for ZrO ₂ particles	101
Figure 57: Agglomerated whiskers produced using the molten salt method	104
Figure 58: Mullite whisker with several secondary whiskers branching out.....	104
Figure 59: A second SEM image of whiskers produced using molten salt method with evidence of residual amorphous silica (as pointed by arrows)	105
Figure 60: SEM image of mullite whiskers after 150 mins of ball milling at 200 rpm	106
Figure 61: Whisker clusters deagglomerated through ultrasonic bath technique	106
Figure 62: SEM image of the surface of ZTA _w after sintering profile 1	108
Figure 63: SEM image of the surface of ZTA _w after sintering profile 2.....	109
Figure 64: ZTA _w after second sintering profile with no visible evidence of residual carbon.....	109

Figure 65: Polished and etched ZTA _n sample at 1 kx magnification	110
Figure 66: Polished and etched ZTA _w sample at 1 kx magnification.....	110
Figure 67: SEM image of ZTA showing ZrO ₂ located at triple points of Al ₂ O ₃ , 1000 times magnification	112
Figure 68: Clustered whiskers preventing ZTA _w densification.....	113
Figure 69: Clustered whiskers allowing ZTA _w densification.....	113
Figure 70: A microstructural defect characterised by increased porosity.....	114
Figure 71: XRD spectrum of ZTA _n powder.....	115
Figure 72: XRD spectrum of ZTA _n sample post-sintering	116
Figure 73: XRD spectrum of ZTA _n powder with sintered ZTA _n overlaid to show phase changes during sintering	117
Figure 74: XRD spectrum of ZTA _w powder prior to sintering.....	118
Figure 75: XRD spectrum of ZTA _w post HIP process	119
Figure 76: XRD spectrum of ZTA _n powder with sintered ZTA _n overlaid to show phase changes during sintering	120
Figure 77: Phase diagram zirconia rich region of the zirconia-yttria system, ● represents compositions and temperatures which will result in monoclinic-cubic mixtures of ZrO ₂ at room temperature, whereas ▪ represents tetragonal + monoclinic, and ○ represents cubic. The red star represents the samples YSZ at sintering temperature [162]	121
Figure 78: Phase diagram of 85%Al ₂ O ₃ -15%ZrO ₂ -Y ₂ O ₃ system [161].....	122
Figure 79: ZTA _n area scanned for EDS analysis.....	123
Figure 80: EDS analysis of ZTA _n	123
Figure 81: Area scanned for ZTA _w analysis.....	124
Figure 82: EDS analysis of ZTA _w	124
Figure 83: Load-Displacement Curve of ZTA _w Sample 3	127

Figure 84: Micro indented ZTA_w with microcracks originating at the edges of the indentation (the arrow indicates the crack propagation from the tips of the diamond impressions) 130

Figure 85: SEM image of ZTA_w fracture surface with evidence of whisker pull-out circled 131

Figure 86: Normalised mass change of ZTA_w vs. number of cycles from room temperature to 1200°C.. 134

Figure 87: SEM image of ZTA_w after HIP process at 200 times magnification 135

Figure 88: SEM image of ZTA_w after 10 cycles 136

Figure 89: SEM image of ZTA_w after 50 cycles. Red circles point to whiskers. 136

Figure 90: SEM image of ZTA_w after 100 cycles 137

Figure 91: SEM image of ZTA_w after 200 cycles with whiskers in square boxes and examples of elongated zirconia grains in circles 137

Figure 92: SEM image of ZTA_w before thermal cycling. Red circles highlight zirconia grains and yellow circles highlight alumina grains. There is no apparent whisker content in this sample. 138

Figure 93: SEM image of ZTA_w after 10 cycles showing densification. Alumina grains circled by yellow and zirconia grains circled by red. There is no apparent whisker content in this sample 138

Figure 94: SEM image of ZTA_w after 50 thermal cycles. Purple circles highlight whiskers. Red circles highlight zirconia grains and yellow circle indicates an alumina grain 139

Figure 95: SEM image of ZTA_w after 100 thermal cycles. Purple circle highlights area of low density due to whiskers. Yellow circles highlight alumina grains and red circles highlight zirconia grains. The light blue circle shows a continuous zirconia grain which has formed between alumina grains. Light green circle shows whisker on the surface 139

Figure 96: Progression of XRD scans for ZTA_w from powder to 450 thermal cycles..... 141

Figure 97: Progression of XRD scans for ZTA_w from powder to 450 thermal cycles with magnification of 25-29 region of 2θ..... 142

Figure 98: Progression of XRD scans for ZTA _w from powder to 450 thermal cycles with magnification of 30-40 region of 2θ.....	143
Figure 99: Progression of XRD scans for ZTA _w from powder to 450 thermal cycles with magnification of 69-74 region of 2θ.....	144
Figure 100: SEM image of ZTA _w after 50 cycles highlighting a large diameter exposed mullite whisker at 800 x magnification.....	145
Figure 101: SEM image of ZTA _w after 50 cycles highlighting a large diameter exposed mullite whisker at 10 kx magnification.....	145
Figure 102: SEM image of ZTA _w after 200 cycles highlighting several small diameter exposed mullite whiskers at 10 kx magnification.....	146
Figure 103: EDS scan of mullite whiskers prior to inclusion in ZTA composite	146
Figure 104: Image of CAD designed impellor and 3-D printed impellor negative	151

List of Tables

Table 1: Economic considerations for various power plants [5].....	6
Table 2: Strength Comparison of Advanced Ceramics and CMCs.....	12
Table 3: Comparison of Fracture Toughness of Various Advanced Ceramics Systems	16
Table 4: Hillig’s Criteria for Ranking Oxides [104].....	49
Table 5: Selected Property Values for Sintered Fully Dense α–alumina [105]	50
Table 6: Whiskers available for reinforcement of oxides [36] [100] [114] [115] [116] [117] [118] [119] ..	54
Table 7: Fracture toughness (K_{ic}), fracture strength (σ_f), flexural strength and microhardness of 3:2 mullite at different temperatures [120]	57
Table 8: Different Colloidal Processing Routes [124].....	58
Table 9: Sample Compositions.....	79

Table 10: Average particle sizes after 8 h of dry ball milling	99
Table 11: D ₅₀ Sizes of alumina and zirconia after various ball mill times	102
Table 12: Porosity of Samples after two different sintering profiles.....	107
Table 13: Average grain size of ZTA _n and ZTA _w after sintering	111
Table 14: Change in size between particles and grains after sintering of ZTA _n and ZTA _w	112
Table 15: Flexural Strengths of Samples Sintered Using Sintering Profile 1.....	125
Table 16: Flexural Strengths of Samples Sintered Using Sintering Profile 2.....	126
Table 17: Flexural strength values of ZTA _n and ZTA _w after 2 different sintering profiles	127
Table 18: Fracture Toughness measurements of ZTA _n and ZTA _w	129
Table 19: Fracture toughness and hardness of ZTA _n and ZTA _w	130
Table 20: Measure Flexural Strength Values of ZTA _n and ZTA _w at 1200 °C	133
Table 21: High Temperature and Room Temperature Flexural Strength of ZTA _n and ZTA _w	133

List of Symbols

E	Elastic Modulus	P_f	Probability of Failure
γ	Surface Energy	m	Weibull Modulus
U	Elastic Energy	ρ	Density
c	Crack Size	AP	Open and Interconnected Pore Content
σ	Stress	C	Mass of the Specimen Saturated with Water
ν	Poisson's Ratio	A	Mass of Dry Specimen
K	Stress Intensity	B	Density of Water
w	width	F	Mass of Specimen in Water
Y	Stress Crack Intensity Constant	P	Load
G°	Gibbs Energy	L	Outer Span
R	Universal Gas Constant		

α_i	Chemical Activity	z	Thickness of 3-Point Bend Specimen
p	Partial Pressure	s	Stress-Strain Slope
Q	Activation Energy	G	Shear Modulus
k	Boltzmann's Constant	k	microcracking constant
T	Temperature	e^T	Dilation Strain
ε	Strain	ψ	Degree of Stabilization
$\dot{\varepsilon}$	Strain Rate	θ	Zirconia Inclusion Constant
S	Creep Constant	X	Toroidal Crack Length
b	Magnitude of Burgers Vector	R	Size of Zirconia Inclusion
d	Grain Size	P	Pressure
V	Volume Fraction of Reinforcing Phases	Π	Reciprocal Modulus of the Composite
η	Viscosity	M	Molar Mass
T	Traction	x	Distance Between Particle Centres
δ	Crack Displacement	t	Time
κ	Damage Factor	ζ	Surface Thickness
α^*	Cohesive Zone Damage Evolution Parameter	L	Sample Length
β	Cohesive Zone Damage Evolution Parameter	Ω	Atomic Volume
λ	Cohesive Zone Damage Free Variable	D	Diffusion Coefficient
B_i	Biot Modulus	Γ	Scaling Parameter
α	Coefficient of Thermal Expansion	ψ	Porosity
Λ	Probability of Failure Constant	V	Molar Volume
J	Sintering Constant	H	Hardness

Subscripts and Superscripts

th	theoretical
o	original
p	plastic
$*$	with microcracking
c	critical
f	fibre
m	matrix
w	whisker
b	composite
DB	debond
s	surface
v	volume
bo	grain boundary

List of Abbreviations

CMC	Ceramic Matrix Composite
GE	General Electric
AMZ	Alumina-Mullite-Zirconia Composite
CERMET	Metal Ceramic Matrix Composite
ZTA	Zirconia Toughened Alumina
CFCC	Continuous Fibre Reinforced Ceramic Composite
CVI	Chemical Vapor Infiltration
WHIPOX	Wound Highly Porous Oxide
DLR	German Aerospace Institute (Deutsches Zentrum Für Luft und Raumfahrt)
PyC	Pyro-Carbon
FGC	Functionally Graded Ceramic
PSZ	Partially Stabilized Zirconia
MSM	Molten Salt Method
DTA	Differential Thermal Analysis
TG	Thermo-gravimetric Analysis
EFS	Electric Field Assisted Sintering
MSC	Master Sintering Curve
EDS	Energy Disruptive X-Ray Spectrometer
SA	Surface Area
TBC	Thermal Barrier Coating
EBC	Environmental Barrier Coating

1.0 Introduction

The world's projected total energy demand is expected to increase by 74% between 2015 and 2035 [1]. This increased demand is coupled with a greater awareness of the threat of global warming and the role of greenhouse gas emissions within that threat [2]. Furthermore, forecasts of the prices of hydrocarbons predict likely price increases as accessible reserves are exhausted and more complicated extraction techniques are required [3]. In the USA alone, gas turbines are expected to account for up to 40% of the energy produced, while the developing world is expected to exceed this figure [4]. It is therefore important to research methods to increase the efficiency and reduce emissions of industrial gas turbines. One clear method of achieving this goal is to increase the inlet operating temperature of the gas turbine hot path. As shown in Figure 1, the simple cycle efficiency of the turbine increases with increasing inlet temperature [5].

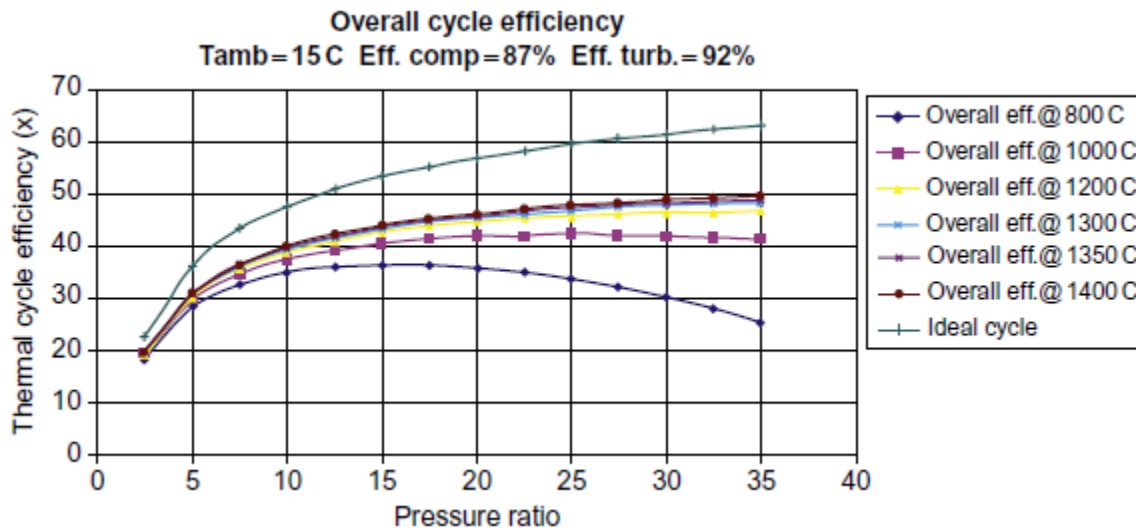


Figure 1: Overall cycle efficiency for simple cycle gas turbine [5]

The operating temperature of industrial gas turbines has steadily increased over the last 7 decades, lagging slightly behind those of aero-gas turbines [6]. These gains in temperature have been achieved through improvements in the superalloys being employed; the thermal and environmental barrier

coatings applied, as well as advanced cooling systems. Figure 2 shows the improvements in operating temperature achieved through the application of these systems.

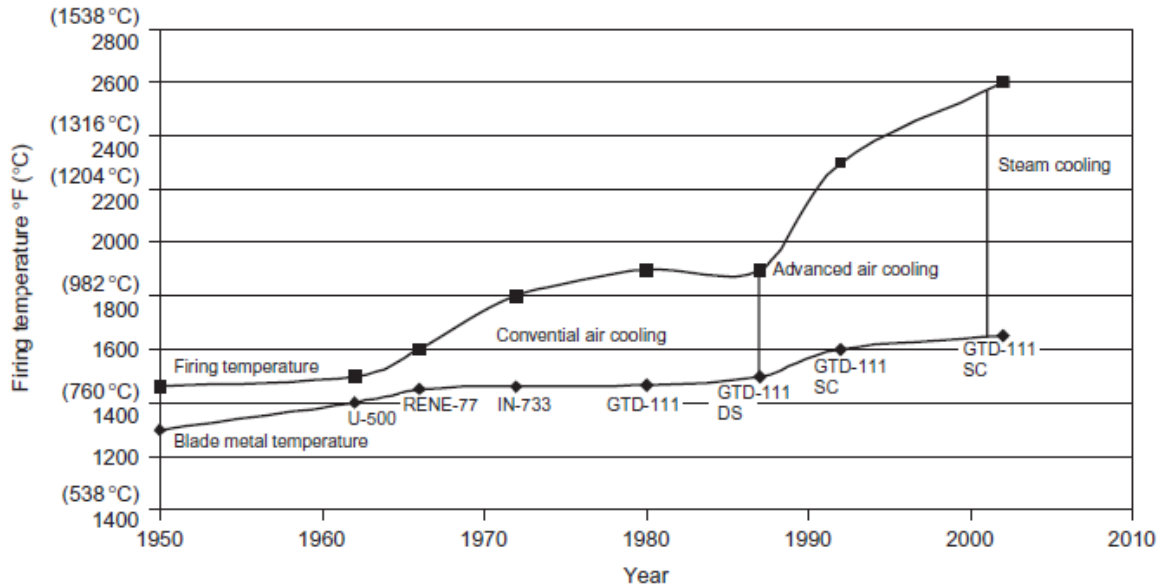


Figure 2: Improvements to firing temperature of gas turbines through materials and cooling system engineering [5]

There is now a major effort being made to incorporate ceramic matrix composites (CMC) into gas turbines. Ceramics have excellent stability, creep resistance, oxidation resistance, low density and high strength at high temperatures, but have been largely ignored due to their brittle nature. CMCs incorporate further phases to improve upon the toughness of bulk ceramics without greatly sacrificing their desirable properties. Throughout the 1970s the Defense Advanced Research Projects Agency commissioned a study to examine whether it would be possible to incorporate CMCs into gas turbines. The report mostly examined bulk SiC/SiC, SiC/Si₃N₄ and Si₃N₄/Si₃N₄ composites and concluded that the composites showed favorable high temperature mechanical properties, but were still too brittle to be largely incorporated. The work further concluded that the stochastic nature of ceramics requires a rigorous statistical analysis of properties. The strength of ceramics often conforms to a weibull distribution and as such, a weibull analysis of the results provides a more complete profile of the strength that can be expected [7]. Recent work by General Electric (GE) has developed a SiC/SiC fibre

based composite which uses a liquid silicon melt infiltration process to produce the matrix. Combined with an environmental barrier coating (EBC) this CMC has been proven to meet the material requirements of the next generation of GE's gas turbines and is now undergoing testing in their F-series engines [8] [9] [10] [11]. Originally incorporated into the shroud and combustors HiPerComp™, which is the commercial name of the material, has been projected to save ~\$960 million in natural gas costs and ~4.3 million metric tons of CO₂ emissions and 51 000 metric tons of NO_x emissions. While HiPerComp™ displays mechanical and thermal properties which have been proven to withstand gas turbine environments and lifetimes there are two major draw backs to the CMC. SiC is vulnerable to aggressive oxidation and failure at 1200°C in water containing atmospheres and must be protected with an environmental barrier coating. Secondly, the cost of materials and processing of HiPerComp™ CMC is greater than the cost of current generation single crystal superalloys. As such it is proposed that an oxide-oxide based CMC be examined to address both of these concerns. With the view of an easily processed, high toughness, high stability oxide-oxide CMC, mullite whisker reinforced zirconia toughened alumina has been investigated.

2.0 Review of Literature

2.1 Gas Turbines

Gas turbines extract rotational mechanical energy from a Brayton cycle. In this cycle the working fluid is drawn in and pressurized in a compressor, then mixed and combusted with fuel, increasing the enthalpy. Work is then extracted by a turbine and the mixture of working fluid and combusted fuel are ejected. Thermodynamic plots of an ideal Brayton cycle are shown in Figure 3.

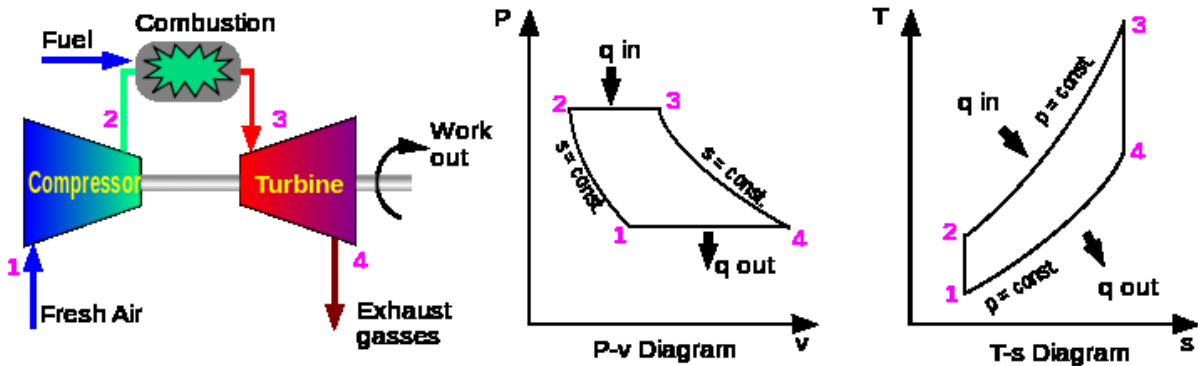


Figure 3: Ideal Brayton Cycle [12]

Gas turbines have primarily been used in either as power plants for aerospace applications or in an industrial capacity to generate electricity or power compressors or pumps. Aerospace turbines focus on performance and output and industrial turbines focus on durability and efficiency. The temperature at which gas turbines operate has generally been higher for aerospace turbines than industrial ones as shown in Figure 4 [5].

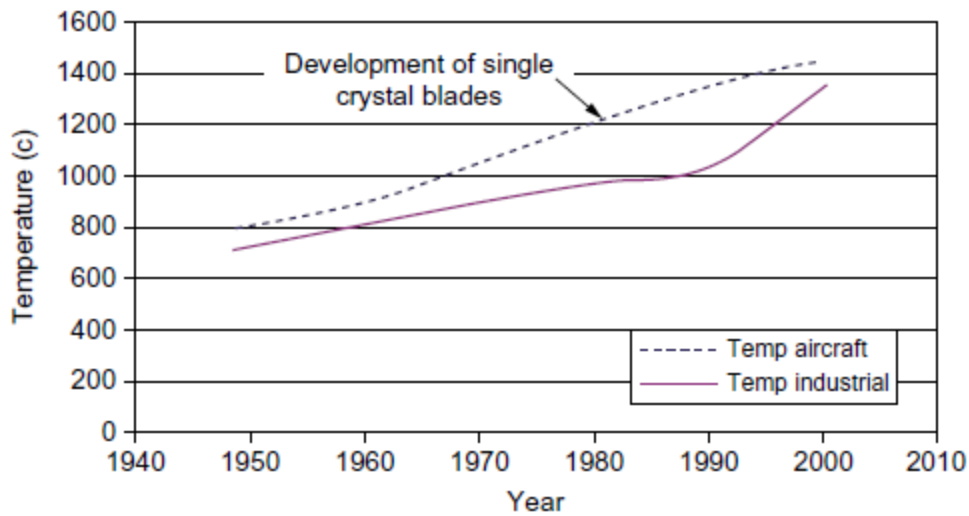


Figure 4: Improvements in firing temperatures of gas turbines [5]

Modern industrial gas turbines vary according to size and scale and can range from microturbines which produce ~30 kW of power to large industrial turbines which produce over 150 MW. Conditions within the respective turbines will vary, larger turbines are expected to operate for lifetimes of 50 000 h, with inlet temperatures of 1427°C and pressure ratios greater than 40:1 [5] [6].

Table 1 shows a comparison of the economic considerations when planning a power plant [5]. It can be seen that a combination of net efficiency, time to completion, and initial capital cost favour advanced gas turbine combined cycle power plants. In addition, the variety of sizes of gas turbines allow for great flexibility when determining the scope and location of power generation. These factors will likely lead to an increased dependence upon gas turbines for power generation, and consequently, demand for advanced materials to improve the efficiency of gas turbine power plants.

Table 1: Economic considerations for various power plants [5]

Type of Plant	Capital Cost (\$/kW)	Heat Rate BTU/kWh (kJ/kWh)	Net Efficiency	Variable Operation and Maintenance (\$/MWh)	Fixed Operation and Maintenance (\$/MWh)	Availability (%)	Reliability (%)	Time from Planning to Completion (Months)
SCGT (2500 °F/1371 °C) Natural gas fired	300–350	7582–8000	45	5.8	0.23	88–95	97–99	10–12
SCGT oil fired	400–500	8322–8229	41	6.2	0.25	90–96	95–98	12–16
SCGT crude fired	500–600	10,662–11,250	32	13.5	0.25	75–80	90–95	12–16
Regenerative gas turbine natural gas fired	375–575	6824–7200	50	6	0.25	86–93	96–98	12–16
Combined-cycle gas turbine	600–900	6203–6545	55	4	0.35	86–93	95–98	22–24
Advanced gas turbine CCPP	800–1,000	5249–5538	65	4.5	0.4	84–90	94–96	28–30
Combined-cycle coal gasification	1,200–1,400	6950–7332	49	7	1.45	75–85	90–95	30–36
Combined-cycle fluidized bed	1,200–1,400	7300–7701	47	7	1.45	75–85	90–95	30–36
Nuclear power	1,800–200	10,000–10,550	34	8	2.28	80–89	92–98	48–60
Steam plant coal fired	800–1,000	9749–10285	35	3	1.43	82–89	94–97	36–42
Diesel generator-diesel fired	400–500	7582–8000	45	6.2	4.7	90–95	96–98	12–16
Diesel generator-power plant oil fired	600–700	8124–8570	42	7.2	4.7	85–90	92–95	16–18
Gas engine generator power plant	650–750	7300–7701	47	5.2	4.7	92–96	96–98	12–16

2.1.1 Evolution of High Temperature Section Materials

The hot section materials within early gas turbines were not highly engineered and depended upon heuristics and manufacturing techniques of the time. Embryonic gas turbines of the late 19th century used bronze alloys for their blade sections. Steel became standard after the invention of the Bessemer process which improved both quality and availability of steel [13]. The first engineered high temperature steel alloys focused upon the inclusion of Molybdenum and Chromium to improve creep resistance and oxidation resistance respectively. As inlet temperatures increased, nickel based superalloys replaced stainless steels in turbine hot section components. Nickel based superalloys are primarily composed of 40%-60% nickel and 10%-25% chromium, with secondary alloying elements of either iron or cobalt depending upon the application. Tertiary alloying elements include Al, B, C, Si, Mo, Nb, Mn, Ti, W, and Zr. Figure 5 compares the material adoption of aerospace gas turbines and industrial gas turbines. The evolution of superalloys and manufacturing techniques is apparent. The increase in stress to creep rupture from IN792 to DS-GTD111 is notable because the alloying components of DS-

GTD111 were predicted using phase stability techniques [5]. It can be seen that manufacturing techniques have also improved the high temperature performance of superalloys. Directionally solidified alloys, where crystals are anisotropically grown along the primary tensile axis, show an improvement in high temperature properties over precision casting. Single crystal alloys have shown an improvement over directionally solidified alloys and are currently the state of the art manufacturing technique for hot section components [6] [14].

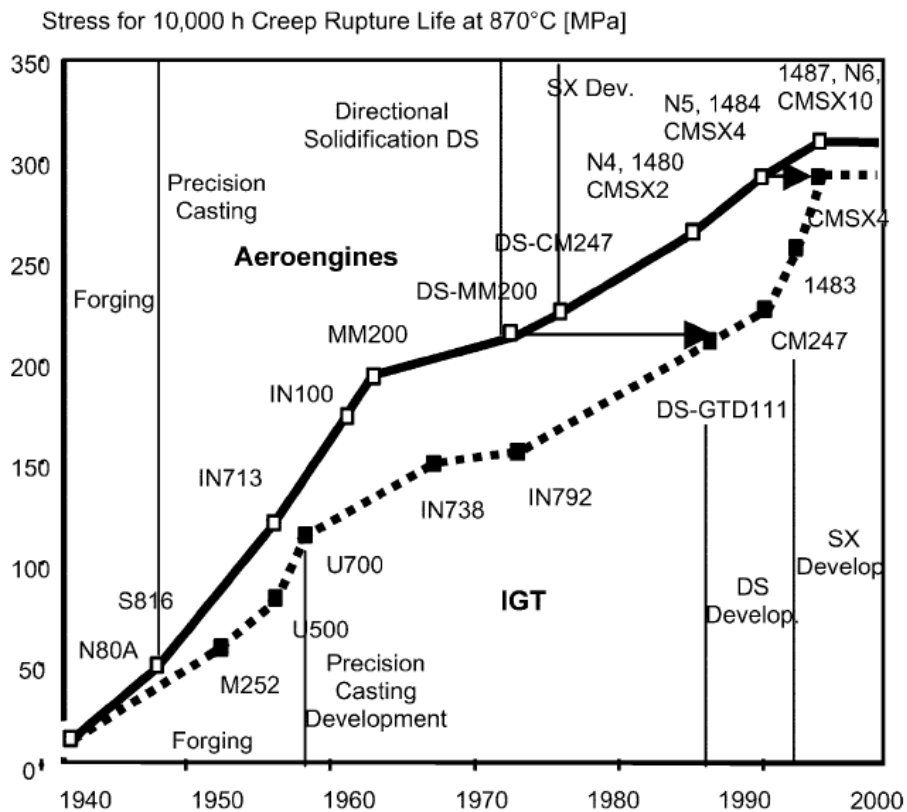


Figure 5: Comparison of the development of aerospace and industrial gas turbine alloys [6]

Further improvements in firing temperatures have been delivered by thermal barrier coatings and cooling systems mentioned in section 1.0 and shown in Figure 5 [5] [15] [16].

2.2 Desired Properties

For a material to be considered for use within a gas turbine there are a variety of properties which it must fulfill. Each potential new material must be proven in a series of escalating tests before a company will risk adopting it for use in commercial turbines. These tests generally conform to the structure of: 1. Lab development 2. Mechanical and chemical property characterization 3. Rig testing 4. Small scale turbine test 5. Large scale turbine tests and production ramp up 6. General adoption [17].

The economics of adopting a new material must also be considered. For the new material to have commercial applications the reductions in fuel and maintenance costs must be greater than the cost of development and processing. The perceived payoff of any material in the early stages of readiness will be extremely theoretical as it is hard to predict the exact efficiency gains, as well as the overall design and production costs; however, when developing SiC/SiC CCFCs GE predicted that for the new design to be economically viable it must cost no more than 3 times than the metal it is replacing, their cost prediction model placed the new SiC/SiC CMC at 2.5 times the metal it was replacing making it viable [9]. Considering the raw materials and processing of the oxide-oxide are less expensive than the SiC/SiC it can be predicted that if this material matches the mechanical, thermal and reliability properties needed, could also be an economically viable replacement. Another potential application for the proposed composite is within next generation micro-turbines where near net shape forming, high temperature stability, and improved reliability are critical [18].

2.2.1 Strength

In material terms the strength of a material is the amount of stress it can withstand before failure, either through yielding (necking), tensile failure or fracture. The theoretical upper limit of strength is the energy it would take to simultaneously break every atomic bond along the fracture plane. By assuming

a linear relationship between the work required, the size of the displacement and scaling to the lattice spacing we can estimate the theoretical strength σ_{th} through equation (1) [19].

$$\sigma_{th} = \left[\frac{E\gamma}{c_0} \right]^{1/2} \quad (1)$$

Where E is the elastic modulus, γ is the energy required to create new surfaces, c_0 is the length of the new surface and σ_{th} is the theoretical strength. The measured strength of brittle materials will be much lower than the theoretical strength because the assumption that the majority of the bonds along the fracture plane simultaneously break is not reflected in reality. Griffiths proposed that a crack will propagate when the decrease in the elastic energy (U) stored within the immediate zone surrounding the crack tip exceeds the increase in surface energy created, expressed in equation (2).

$$U = -\frac{\pi c^2 \sigma^2}{E} + 4\gamma c \quad (2)$$

Where c is the crack size, σ is the stress, E is the elastic modulus and γ is the surface energy created by a new surface. It can be seen that surface energy varies with c , while the crack extension energy varies with c^2 , therefore at a certain critical crack size c , crack extension will be energetically favourable and the crack will propagate unimpeded causing catastrophic failure. The critical crack size (c) is expressed by equation (3)

$$c \geq \frac{2\gamma E}{\sigma^2 \pi} \quad (3)$$

Orowan incorporated tolerance for some plasticity into the Griffiths criterion by including an effective plastic surface energy term (γ_p). Equation (4) shows the estimate for critical stress which will result in catastrophic failure in brittle materials.

$$\sigma_c \approx \left(\frac{E(\gamma + \gamma_p)}{c} \right)^{1/2} \quad (4)$$

The Griffith-Orowan criterion places an upper limit on stress magnitude before catastrophic failure [19]. A second approach incorporates maximum distortion energy criterion combined with the stress tensor, this approach takes into account the 3-D tensor nature of more complex stress profiles. The maximum distortion energy criterion is summarized in equations (5) and (6) where equation (5) represents the total strain energy while equation (6) represents the maximum strain energy for yielding and failure.

$$U_T = \frac{1}{2E} [\sigma_1^2 + \sigma_2^2 + \sigma_3^2 - 2\nu(\sigma_1\sigma_2 + \sigma_2\sigma_3 + \sigma_3\sigma_1)] \quad (5)$$

$$U_d = \frac{1+\nu}{6E} [(\sigma_1 - \sigma_2)^2 + (\sigma_2 - \sigma_3)^2 + (\sigma_3 - \sigma_1)^2] \quad (6)$$

Where E is the elastic modulus, the σ_i terms represent stress components of a Cauchy Stress Tensor, and ν is the Poisson's ratio. Flaws will act as stress concentrators and lower the strength of the material. Some of the more common microstructural defects include incongruences, vacancies, inclusions, solutes, grain boundaries, inherent stress gradients, and micro-cracks.

The material's strength can be expressed in several forms such as the ultimate tensile strength, compressive strength or shear strength depending upon how the material is loaded. Most structural materials fail in tension before compression; however, tensile testing of ceramics is exceedingly challenging due to machining requirements and very low strains to failure. The most common strength

property reported for bulk ceramics is the flexural strength. Although flexural strength provides a measure with which to compare materials it is not the most accurate representation of a brittle material's strength. Due to the brittle nature of ceramics, failure is very stochastic in nature and a statistical expression of strength is more representative of the true constraints of the material. Therefore the strength of brittle materials is often reported with both the characteristic strength and a weibull modulus, which will be covered further in section 2.2.7. The flexural strength values of various ceramics and CMCs are compared in Table 2.

For the new material to be comparable to existing CMC's it should possess a flexural strength of around 425 MPa at room temperature and 330 MPa at 1200 °C, in addition to other attributes [7] [20]. This can be compared to flexural strength values for other CMCs including earlier forms of ZTA, SiC/SiC composites and Si₃N₄ based composites.

Table 2: Strength Comparison of Advanced Ceramics and CMCs

Material	Process	Flexural Strength (MPa)		Notes	Source	
		Room Temp	1200°C			
Alumina	Commercial alumina Nano Crystalline alumina	Hot Pressed at 1850°C	210			[21]
			475		3.5µm grain size	[22]
			683		1.2 µm grain size	[23]
			536		.89 µm grain size	[24]
			707		.63 µm Al ₂ O ₃ 200 nm Cu grain size	[24]
Al ₂ O ₃ /10%SiC		560		2.9 µm Al ₂ O ₃ 200 nm SiC	[25]	
Al ₂ O ₃ /20%SiC _w		805	520		[26]	
Zirconia	Polycrystalline 75% mullite/25% zirconia	Cold Pressing reaction sintered	900-1200		grain size of .5 µm	[27]
			270		ΔT 360	[28]
Mullite		HIP	270		ΔT 300	[29]
Zirconia Toughened Alumina	56% mullite/26% alumina/18% zirconia	reaction sintered	315		ΔT 325	[28]
	72% alumina/11% mullite/17% zirconia	reaction sintered	330		ΔT 285	[28]

Material	Process	Flexural Strength (MPa)		Notes	Source
		Room Temp	1200°C		
Silicon Nitride	SN-81	690	590		[30], [31]
	SN-88	790	770		[30], [31]
	Si ₃ N ₄ +Y ₂ O ₃ /SiO ₂	Pressureless sinter Sintered at 1800 °C in Nitrogen under pressure 1.8 Mpa	469	219	
Fibre Based Oxide-Oxide CMC	Nextel 720 Alumino silicate system	179	170 (at 1000°C)		[33]
	Nextel 440-modified LAS	100	70(900°C)		[34]
	Sumica-3Al ₂ O ₃ -2SiO ₂ -1B ₂ O ₃	100	70(900°C)		[34]
Fibre Based Silicon Carbide CMC	HiPerComp™	298			[11]

2.2.2 Toughness

Brittle materials fail according to the weak link theory, where the largest flaw will govern the overall strength of the material. Two materials with the same microstructure but different flaws will have different strengths. The shape and type of flaw will also play a role due to varying stress concentrating effects of different crack tip geometries. Stress intensity, K , given by equation (7) has been introduced to scale the stress amplification of different crack geometries.

$$K = \sigma\sqrt{\pi c} \cdot f\left(\frac{c}{w}\right) \quad (7)$$

Where $f(c/w)$ is a function based upon the shape and length of the crack, the loading mode (there are 3 loading modes: case 1, where tensile stress is normal to the plane of the crack; case 2, where shear stress is parallel to the plane of the crack and parallel to the direction of crack propagation; and case 3, where shear stress is parallel to the plane of the crack and normal to the direction of crack propagation) and the width of the sample. The combination of stress and crack geometry which results in unbounded crack growth corresponds to a critical stress intensity which is material (and loading mode) dependant. This critical stress intensity is usually given the nomenclature K_{Ic} and is expressed as the material's toughness or fracture toughness under mode I [35]. The critical stress intensity will also sometimes be seen in the form of equation (8) where Y is a constant which accounts for the crack geometry function. For sharp edged cracks in mode 1 loading Y , takes a value of 1.12, and circular cracks will have a Y value of $2/\pi$ provided the width of the sample is much larger than the crack length

$$K = \sigma Y \sqrt{\pi c} \quad (8)$$

As a crack propagates, the stress concentration around the crack tip will create a process zone ahead of the crack. Interactions between the process zone and the material can serve to increase the material's

R value both ahead of and behind the crack. The **R** value is determined by rearranging equation (3) from section 2.2.1, into equation (9) where the 2γ is the crack resistance, **R**.

$$\frac{\pi\sigma^2c}{E} \geq 2\gamma \quad (9)$$

Advanced ceramics use various techniques to take advantage of this effect improving the overall fracture toughness of the material; these will be further covered in section 2.3. Reported fracture toughness values of various ceramic materials are summarized in Table 3 where toughening effects via various mechanisms can clearly be seen [19].

Table 3: Comparison of Fracture Toughness of Various Advanced Ceramics Systems

Material		Process	Fracture Toughness (MPa·m ^{1/2})	Notes	Source
Alumina	Commercial alumina	Hot Pressed at 1850°C	1.75	Hardness of 1600 kg/mm ²	[21]
	Nano Crystalline alumina		3.6	3.5 μm grain size	[22]
			3.5	1.2 um grain size	[23]
			3.57	.89 um grain size	[24]
	Al ₂ O ₃ /5%Cu		4.28	.63 um Al ₂ O ₃ 200 nm Cu grain size	[24]
	Al ₂ O ₃ /10%SiC		5.2	2.9 um Al ₂ O ₃ 200 nm SiC	[25]
	Al ₂ O ₃ /20%SiC _w *		8.7		[26]
SWCN** reinforced nano-alumina	Powder Route, sintered by SPS at 1150°C	9.4	Hardness of 1642 kg/mm ²	[36]	
Zirconia	Polycrystalline	Cold Pressing	9.0	grain size of .5 um	[27]
	75% mullite/25% zirconia	reaction sintered	4.6		[28]
Mullite		HIP	1.8		[29]

Material	Process	Fracture Toughness (MPa·m ^{1/2})	Notes	Source
Zirconia Toughened Alumina	56% mullite/26%alumina/18%zirconia	reaction sintered	4.75	[28]
	72%alumina/11%mullite/17%zirconia	reaction sintered	5.25	[28]
Silicon Nitride CMC	Si ₃ N ₄ /3%MgO/1.5Al ₂ O ₃ /5%SiO ₂	1780°C 3h in nitrogen pressure	6.3	[37]
	Si ₃ N ₄ /10%SiO ₂ /5%Yb ₂ O ₃	Pressureless sinter at 1750°C under nitrogen (0.1MPa)	9.1	[38]
	Si ₃ N ₄ -TiN/6%Y ₂ O ₃ /2%Al ₂ O ₃	Hot Pressed at 1800°C in N ₂ atmosphere	6.5	[39]
	Si ₃ N ₄ (95%α-5%β)/8%Y ₂ O ₃ /1.5%Al ₂ O ₃	Attrition milled powders and horizontal rolling milled	9.5	[39]

*SiC_w – Silicon carbide whiskers

**SWCN – Single walled carbon nanotube

2.2.3 Corrosion and Oxidation Resistance

Corrosion of a material occurs when it chemically reacts with its environment either by losing mass through volatilization or gaining mass through the formation of scale. The high temperatures and reactive environments found within the hot path of gas turbines lead to high environmental degradation rates. The corrosion of structural components leads to a degradation of important properties and can cause failure. Thermodynamic equilibriums determine the oxidation behavior of the material. Surface oxidation occurs when the oxygen potential is greater than the oxygen partial pressure in equilibrium with the oxide. The chemical equation of the reaction is shown by equation (10) while the equilibrium balance is given by equation (11)



$$\Delta G^o = -RT \ln \left(\frac{a_{MO_2}}{a_M \cdot p_{O_2}} \right) \quad (11)$$

Where ΔG^o is the change in Gibbs energy for the reaction shown in equation (9), R is the universal gas constant, T is the absolute temperature, and the a represents chemical activity of the various components in equation (10). When the activities of the solid metal and oxide are equal then the oxygen potential becomes

$$p_{O_2} = e^{\Delta G^o/RT} \quad (12)$$

The oxygen potential can then be calculated to determine whether an oxide scale will form on the surface [40] [41]. For ceramics composed of stable oxide(s) surface oxidation is less of a concern. The primary concern in this case is the diffusion of oxygen through the matrix which may encourage reactions between reinforcing phase(s). These reactions may introduce weaker constituents or create voids of pressurized gas; both outcomes will negatively affect the structural properties of the oxide composite. An example of an adversely affected CMC is SiC whisker reinforced alumina. In Al_2O_3 -SiC_w,

SiC whiskers oxidize upon exposure to oxygen at high temperatures, forming mullite, and aluminosilicate glass phases around the whiskers as well as pockets of CO gas [42]. Internal oxidation is also determined by thermodynamic equilibriums; however, the oxygen content may be limited by diffusion mechanics.

A further concern is the interaction of corrosion/oxidation mechanics and fracture mechanics leading to stress corrosion cracking. It is therefore important to either design CMC materials that will not react with species in the environment, or apply a compatible environmental protection barrier [21].

2.2.4 Creep Resistance

Creep is the plastic deformation of a material due to a stress which is below the yield stress over a period of time. In most materials this effect is present at temperatures about 40% of the absolute melting temperature and becomes more prevalent at greater temperatures, it is therefore often considered a thermal process. Extensive empirical studies have divided creep behavior into three separate regimes based upon the strain profile. Different creep regimes will activate depending upon various factors such as microstructure and ductility, temperature, and stress intensity; however, the most common pattern is, for a material, to begin with primary creep then move into secondary and finally tertiary regimes. The three regimes are qualitatively represented in Figure 6.

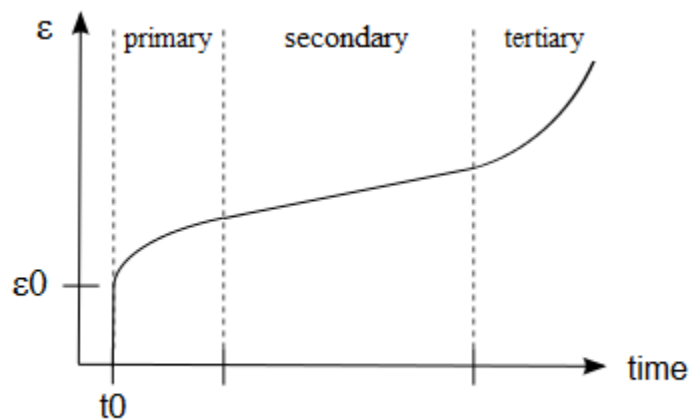


Figure 6: Strain vs. time showcasing the three regions of creep [12]

Primary creep consists of a decelerating strain rate; in this region the material may be prone to hardening caused by microstructural changes such as dislocation entanglement or solute hardening in metals. The secondary region consists of steady state strain. An important set of secondary creep mechanisms are diffusional; such as grain boundary sliding, vacancy motion in grains and on the grain boundaries [43] [44]. Tertiary Creep consists of an accelerating strain rate and causes material damage and rupture. In this state the material may exhibit the propagation of microcracks and voids along grain boundaries or other incoherencies such as, grain boundary sliding through diffusion, plastic deformation or the conversion of grains to a glassy phase. In engineering applications creep is ideally limited to the primary and secondary regions during which the materials spend their lifetime.

The mechanisms of creep activated plastic deformation centre around either the grain boundaries of polycrystalline materials or the crystal lattice of the material. The four categories of grain boundary deformation are cavitation creep and microcracking, interface reaction controlled diffusion creep, grain boundary sliding and grain rearrangement, and diffusion creep. Grain boundary related creep is accommodated either through the diffusion of vacancies from areas under tensile stress to areas under compressive stress, the sliding and elongation of grains relative to one another, grain boundary sliding accommodated by dislocations along grain boundaries, or the formation of cavities and microcracks. The two categories of lattice deformation are dislocation climb and dislocation glide controlled by climb. The activation of lattice creep is controlled by the number and orientation of independent slip systems or through dislocations activated from Bardeen-Herring sources [45].

The secondary creep region is commonly modeled by an empirical equation (13) [40]. Strain rate ($\dot{\epsilon}$) can be expressed as

$$\dot{\epsilon} = S \left(\frac{\sigma}{G} \right)^n \exp\left(-\frac{\Delta Q}{kT}\right) \quad (13)$$

Where S is a constant, σ is the applied stress, G is the shear modulus, ΔQ is the activation energy, k is the Boltzmann's constant and T is the absolute temperature. The exponent n varies depending upon the mechanism of creep and will be between 1 and 2 for creep regimes primarily defined by diffusional mechanisms and between 3 and 7 for creep regimes primarily defined by dislocation climb. Polygrained ceramics will have n values between 2 to 4, due to most creep occurring as grain boundary sliding and void nucleation. Whisker reinforced CMCs will reduce the n value due to whiskers interfering with grain boundary sliding; however, too high of a volume fracture for whiskers will lead to more areas for void nucleation and greatly reduce creep resistance [44].

A second strain rate expression, equation (14), relates the creep to microstructural properties: D , the appropriate diffusion coefficient, G , the shear modulus, b , the magnitude of burgers vector, and d , the grain size.

$$\dot{\epsilon} = A \frac{DGb}{kT} \left(\frac{b}{d}\right)^p \left(\frac{\sigma}{G}\right)^n \quad (14)$$

This equation only applies to single phase polycrystalline materials, where p is the grain size exponent and n is still the stress exponent [45]. The microstructural approach to creep can be extended to a multiphase system and equation for the rate of plastic deformation will take on different forms depending upon the modes of creep expected from the phases. In a composite with rigid additions and the primary creep mode of the matrix being grain boundary sliding the creep can be modeled by equation (15)

$$\dot{\epsilon} = S \frac{\sigma^n}{d^p r^q V} \exp\left(-\frac{Q}{RT}\right) \quad (15)$$

Where V is the volume fraction of the reinforcing phases, q and n are phenomenological exponents and S is a constant. Wakashima and Liu have developed a continuum model for a two phase composite in which each phase undergoes diffusional creep [46].

$$\varepsilon = \left[\frac{\Delta E}{E_u} \left\{ 1 - \exp\left(-\frac{t}{\tau}\right) \right\} + \frac{1}{\bar{\eta}} \right] \quad (16)$$

$$\frac{\Delta E}{E_u} = \frac{V_1}{p_1} \left(q_1 - \frac{\eta_1}{\bar{\eta}} \right)^2 = \frac{V_2}{p_2} \left(q_2 - \frac{\eta_2}{\bar{\eta}} \right)^2 \quad (17)$$

$$\tau \equiv \frac{1}{p_1 - p_2} = \frac{\eta_1}{p_1} \left(1 - V_1 \frac{\eta_1}{\bar{\eta}} \right) = -\frac{\eta_2}{p_2} \left(1 - V_2 \frac{\eta_2}{\bar{\eta}} \right) \quad (18)$$

Where V_i is the volume fraction of phase i , η_i is the viscosity of phase i undergoing Newtonian viscous flow, $\bar{\eta} \equiv V_1\eta_1 + V_2\eta_2$; q_i is the phase stress concentration factor where $V_1q_1+V_2q_2=1$ and p_i is the internal stress caused by the mismatch in creep strains between the phases where $V_1p_1+V_2p_2=0$ [45].

2.2.5 Fatigue Resistance

The exposure to cyclic loading conditions will alter a material's properties; this phenomenon is known as fatigue. The alteration of material properties is achieved by minute plastic deformations which may lead to micro-crack initiation followed by micro-crack propagation. Fatigue is a concern in any material which undergoes cyclic loading as damage may occur at stress levels well below the yield stress. In contemporary engineering two different methods dominate the treatment of fatigue. The more traditional approach is to use empirically derived equations, either Paris-Erdogan shown by equation (19) for slow crack growth with a process zone much smaller than the crack size (c) or the Coffin-Manson relation shown by equation (20) for low cycle fatigue.

$$\frac{dc}{dN} = C(\Delta K)^m \quad (19)$$

$$\frac{\Delta \epsilon_p}{2} = \epsilon'_f (2N)^c \quad (20)$$

Where N is the number of cycles, C and m are constants depending upon material properties and ΔK is the variation of the stress intensity factor [47]. The rain-flow counting algorithm, which normalizes the damage caused by changes in stress, is combined with the above empirical equations to predict failure.

The second method uses a cohesive zone damage model to predict crack initiation and growth. This model uses a damage factor function which scales the traction to the crack tip displacement as can be seen in equations (21), (22) and (23).

$$T = f(\kappa)\delta \quad (21)$$

$$f(\kappa) = \frac{\sigma_c(1 - \kappa)}{\kappa(\delta_u - \delta_c) + \delta_c} \quad (22)$$

$$C(\kappa) = \sigma_c(1 - \kappa) \text{ and } T \leq C(\kappa) \quad (23)$$

Where T is traction, κ is the damage factor which scales from 0 to 1 where 0 presents no damage and 1 is for failure, σ_c is the critical stress, δ is displacement with subscript u denoting crack tip displacement at failure and subscript c denoting crack tip displacement at which damage starts to accumulate. The damage factor is adjusted according to the following inequalities.

$$\begin{aligned} \dot{\kappa} &= \alpha^* \kappa (T - \beta C)(\dot{\delta}) \quad \text{If } (T - \beta C)(\dot{\delta}) > 0 \\ \dot{\kappa} &= 0 \quad \text{If } (T - \beta C)(\dot{\delta}) < 0 \\ \dot{\kappa} &= \dot{\lambda} \quad \text{If } T=C \text{ and } \dot{\delta} > 0 \end{aligned} \quad (24)$$

Where $\dot{\lambda}$ is a free variable. α^* and β are damage evolution parameters dependent upon the material. The advantage of this interpretation of the cohesive zone model is its incorporation of a bounded

linearized damage factor which accommodates for changing material properties around the crack tip zone. This allows one to adapt the model to FEA efforts as well as predict fatigue performance in extreme cases such as overloading and crack healing [48].

The anisotropic nature of CMCs leads to a more complex fatigue analysis and profile than that of bulk ceramics. The interactions between the multiple damage mechanisms and fatigue resistant elements within the composite will decide the fatigue profile [44].

2.2.6 Thermal Shock and Thermal Fatigue Resistance

Thermal shock is a concern for materials which may experience a sudden temperature change, an example being a gas turbine in emergency shutdown where the temperature may suddenly drop up to several hundred degrees centigrade over the course of several minutes. When a monolithic material is heated or cooled quickly a thermal gradient will arise and thermal expansion will cause strains, generating a stress field. The maximum stress will occur either at the surface (tension during cooling) or core, equation (25) predicts the maximum stress in a plate.

$$\sigma_{max} = \frac{E\alpha\Delta T}{1-\nu} \left(1.5 + \frac{3.25}{Bi} - 0.5e^{-16/Bi} \right)^{-1} \quad (25)$$

Where Bi is the Biot modulus which relates heat transfer to dimensions and is given by equation (26).

$$Bi = l \frac{h}{k} \quad (26)$$

In equation (25), l is the characteristic dimension, h is the heat transfer coefficient between the body (material) and medium and k is the thermal conductivity of the solid material. In composites where different phases have different thermal expansion coefficients, more complex stress fields will form. It can be seen that stress varies directly with temperature change. At a large enough temperature change, the generated stresses will lead to microstructural damage (cracking, phase transformation) and reduce

the strength of the composite. In cooling the greatest tensile stresses are developed at the surface, when this effect is combined with surface defects catastrophic failure may occur [49]. Figure 7 shows a typical strength vs. temperature change profile of an alumina-mullite-zirconia (AMZ) composite with various amounts of SiC added. It can be seen that after a temperature change of 300°C, the strength of the composite with 0 wt% SiC is severely reduced, whereas that strength reduction isn't visible until a change of 1200°C in the 10 wt% and 20 wt% SiC additions in AMZ composite [50].

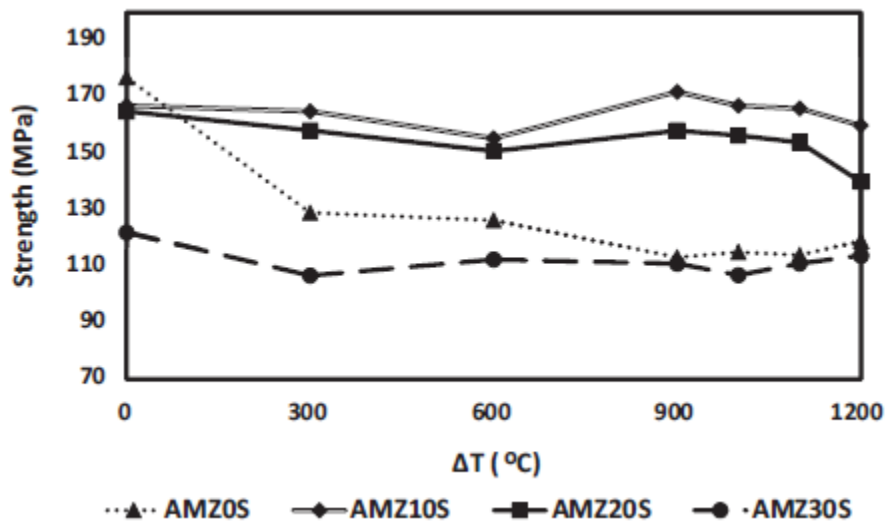


Figure 7: Strength of alumina-mullite-zirconia composites with various wt% SiC additions after 1 cycle thermal shock test

The thermal shock resistance of a material is expressed in °C and is the experimentally determined temperature change the material can undergo before a loss in properties.

Thermal fatigue is a form of fatigue where the stress amplitude of the cyclic loading is caused by coefficient of thermal expansion mismatch. For materials which will be undergoing heating and cooling cycles it is important to account for the internal stresses which will be generated and ensure that material failure will not occur through thermal fatigue.

2.2.7 Statistical Analysis of properties

As mentioned in the above sections, ceramics exhibit brittle stress-strain behavior and failure is often highly stochastic. This is due to the inability of ceramics to relieve local stress concentrations caused by flaws through plastic flow. The random distribution of flaws leads to differences of exhibited strengths within ceramics which have been processed in the same way as well as within the ceramic itself. To adjust for this behaviour is an approach which predicts the probability of failure of individual elements within the ceramic. The probability of failure of each element is then integrated over the entire structure to calculate the probability of failure of that component. Work by Vardar and Finnie has shown an integral formulation of the weibull approach given by equation (27) [51]

$$P_f = 1 - e^{-\int V(\Lambda \int A \sigma_n^m dA) dV} \quad (27)$$

Where Λ is a constant determined by the weibull modulus. This formula can be simplified by the assumption of uniform uniaxial stress to equation (28)

$$P_f = 1 - e^{-\int \left(\frac{\sigma}{\sigma_0}\right)^m dV} \quad (28)$$

Where P_f is the probability of failure, σ is the applied stress, σ_0 is the stress at which probability of failure is 100%, m is the weibull modulus and V is the volume. The weibull modulus is the measure of how closely the material adheres to a weibull distribution, a higher modulus will mean that there is little variation in the strengths measured [7].

Ideally the material should have a weibull modulus of 20 to 25; however, most ceramics will have a modulus between 5 and 10 [19].

2.3 Composites

Bulk ceramics are rarely used in mechanical applications despite their enhanced hardness, strength, thermal resistance, and corrosion resistance. This is due to their brittle nature preventing their reliable adoption. Engineers have developed a composite system for reducing the brittleness of ceramics, where a second phase alters the property of the material. Ceramic based composites can take many forms including: ceramic metal composites (CERMETS) [52] [53]; mechanical mixtures of more than one ceramic phase such as Zirconia Toughened Alumina (ZTA) [54] or rod-like β - Si_3N_4 phase within an α - Si_3N_4 matrix [39] [55]; or fibre based composites [9] [56] [57]. The focus of this work is high temperature CMCs designed to operate around or above 1200°C so CERMETS will not be examined in any detail.

Ceramic matrix composites can be divided into two main branches based on the reinforcement phase. Continuous fibre reinforced ceramic composites (CFCCs) are enhanced by long, continuous fibres which provide the stiffness and strength of the composite while the matrix protects the fibres and transfers the load. Discontinuously reinforced CMCs use a secondary phase to enhance the properties; this phase often takes the form of randomly aligned particulates or whiskers, although CMCs which rely on transformation toughening or layered eutectic structures are also loosely grouped into this class.

2.3.1 CFCCs

CFCCs have received much attention due to their graceful failure [58]. This has made them a highly attractive material to replace high temperature alloys in the near future because current reliability models for superalloys can more easily be adapted to their use [11] [17] [59]. The greatest challenges preventing the widespread adoption of CFCCs to high temperature applications are the costs associated with the production and the development of a material properties database for existing CMCs [9] [11]. A successful CFCC must consist of a fibre phase, a fibre-matrix interface, and a matrix; an environmental protection barrier may also be necessary depending upon the chemical composition of the phases and

the environment where the CFCC will be utilized. High tensile strength is the primary structural property for the fibre phase; this will depend upon the microstructure and chemical composition of the fibre. The fibre-matrix interface is responsible for the enhanced toughness of the CFCC; the interface must be able to both transfer loads from the matrix to the fibres as well as deflect any cracking along the surface of the fibres by debonding. The conflicting requirements of the crack deflection and load transfer as well as the necessity of the interface to be chemically compatible with both the fibre phase and the matrix mean that the interface often provides the greatest design challenge. Finally, the matrix phase is responsible for transferring loads between fibres as well as protecting the fibres from the environment. In cases where the CFCC's intended application is an environment where the matrix will degrade, an environmental protection coating may be added to provide an extra layer of protection.

CFCCs can be divided into three sub-categories based upon the fibre phase and the matrix phase. These sub-categories are oxide/oxide, non-oxide/non-oxide, and non-oxide/oxide.

2.3.1.1 Oxide/Oxide Systems

Oxide/oxide systems are of interest due to the inherent oxidation resistance of the phases as well as the economy of the materials. Oxide fibres were originally developed from fibre glass production and are primarily based upon alumina, silica and zirconia [60]. The Nextel series of fibres by 3M have been some of the most successful oxide fibres produced to date. Nextel fibres are produced through a sol-gel method where a sol-gel containing oxide precursor is spun through a spinnerette, followed by pyrolyzation to remove organics and sintering [60] [61]. Nextel series of fibres have shown varying levels strength and creep resistance, with Nextel 720 showing the greatest creep resistance but susceptibility to alkaline poisoning [62] [63]. In oxide fibres grain boundary sliding has been shown to be the route of failure for high temperature exposure [64] [65]. Single Crystal oxide fibres have therefore attracted interest due to the inherent creep resistance expected from an oxide fibre with no grain

boundaries. Current work with producing single crystal fibres relies on a laser melt zone method in which a small section of a composite is melted; a seed crystal is used to draw the fibre from the melt zone [66]. This production method is slow, expensive and produces large diameter fibres which are difficult to handle and lay-up and is therefore not considered commercially viable, although Saphikon produces sapphire fibers which have been useful for academic studies [67] [68] [69]. In general, oxide fibre reinforcements will be weaker and more prone to creep failure than covalently bonded fibres, for applications below 1200 °C the cost savings and chemical stability may justify their use in CFCCs.

Oxide-oxide CFCCs can either incorporate a weak interface or use a porous matrix to ensure that failure remains pseudo-ductile. The most common weak interfaces used in CFCCs are pyro-carbon and boron nitride; however, both these interfaces are more susceptible to oxidation than the oxide fibre or matrix defeating the purpose of using oxide constituents. Monazite and scheelite have been explored as potential interfaces for oxide systems, with both interfaces demonstrating fibre pull-out during failure; however, these coatings still rely on time intensive and expensive methods of application [70] [71]. Porous matrices or porous fibre-matrix interfaces are designed to fail before the fibre reinforcement will fail. In porous matrix systems the design principle is for cracks to travel from pore to pore without damaging the fibres. Porous fibre-matrix interfaces are designed to fail at the onset of cracking, directing any crack parallel to the fibre [69]. Porous matrices will provide less stiffness than a highly dense matrix and will also conduct oxidation; furthermore, porous matrix ceramics cannot be depended upon in applications where a hermetic seal is required [69].

Weak oxide interphases are based on highly polarized oxide bonds caused by high valence cations. The generic formula MXO_4 covers most forms where M is a rare earth and X is a pentavalent cation. Work by Lewis et al. has been conducted to study which combinations of elements will produce stable weak interfaces with common oxide constituents with lanthanum vanadate, yttrium vanadate and

neodymium phosphate as promising candidates [72]. Weak oxide interfaces are applied to the fibre before the matrix is applied using a chemical deposition method, most commonly chemical vapor infiltration (CVI). CVI poses challenges for industrial manufacturing due to high costs and lengthy timescales so other methods for interface application have been investigated. Lewis et al. have demonstrated a physical vapor deposition method which uses RF magnetron sputtering argon to apply the chemical coat [72].

The method of production for the oxide matrix will vary depending upon whether the matrix is intended to be porous or not. Solid oxide matrices can be manufactured by CVI or slurry infiltration. Porous oxide matrices are most often produced through slurry infiltration. The slurry can be composed of a bimodal distribution of particle sizes, the combination of large particles and small particles leads to an adequate and even distribution of pores to ensure notch insensitive behavior, this is illustrated in Figure 8.

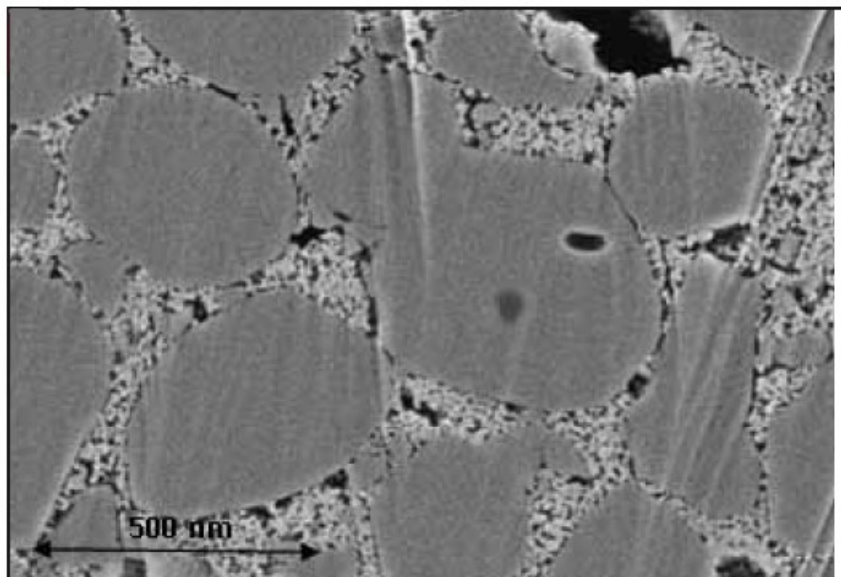


Figure 8: Bimodal particle distribution within an oxide/oxide CMC to ensure porosity [73]

A novel method of ensuring slurry infiltration, known as electrophoretic deposition, has been developed by Westby et al. [74]. In this method an electric field is placed across the Nextel 720 fibre weave which has been placed within a slurry bath. Surfactants are then used to give the oxide particles a charge and these particles are driven by the electric field infiltrating the weave. This process has proven to be faster than traditional slurry infiltration methods.

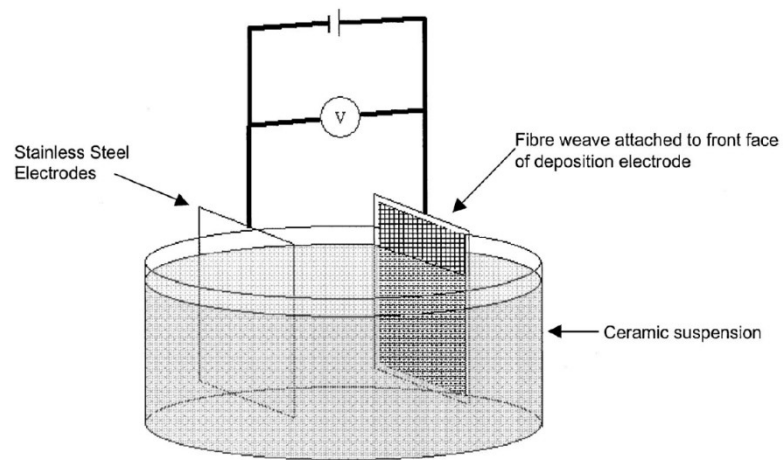


Figure 9: Basic electrophoretic deposition set up [74]

Two oxide CMC systems of note are the (**W**ound **H**ighly **P**orous **O**xide) WHIPOX system developed by the German Aerospace Institute (DLR) and the Nextel 610 oxide system developed by COI ceramics. The WHIPOX system uses a slurry infiltrated computer controlled winding system shown in Figure 11, followed by wet layup and pressureless sintering to produce a variety of near net shape structures.

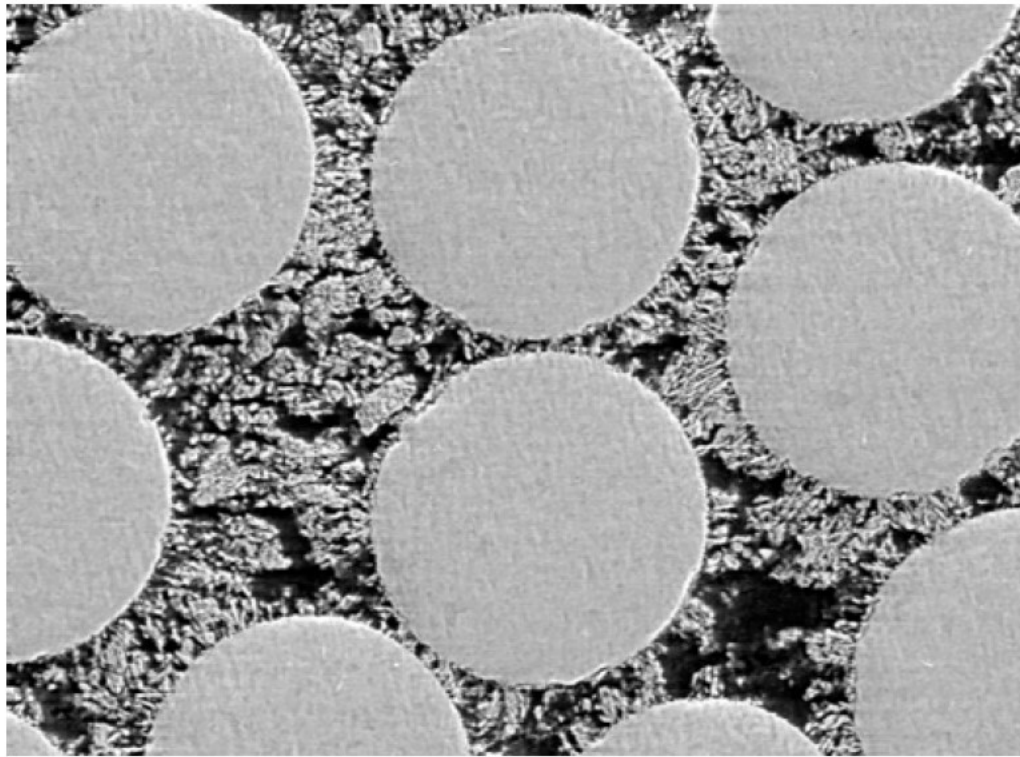


Figure 10: Cross section of WHIPOX oxide ceramic illustrating fibres, bimodal distribution of particles and porosity [76]

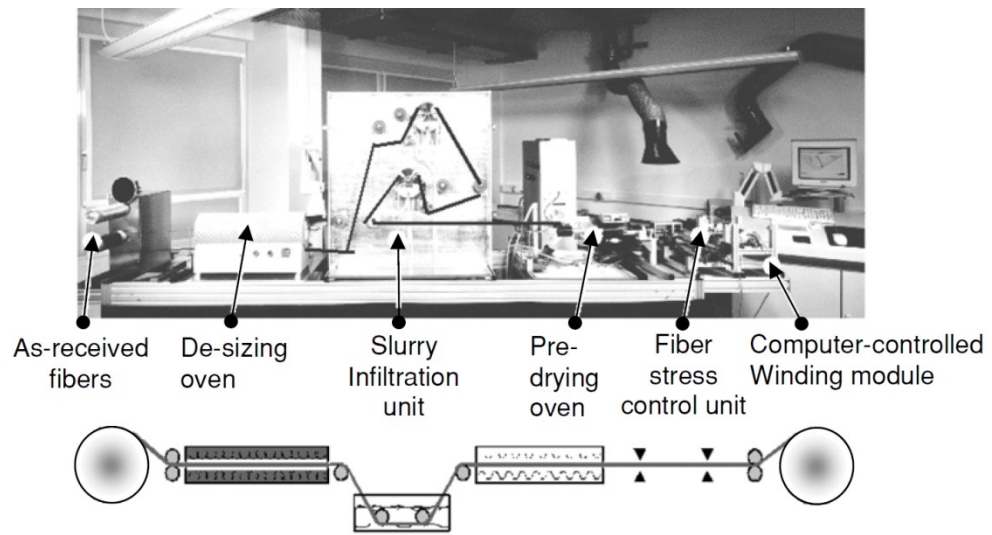


Figure 11: WHIPOX winding steps, equipment above simplified representation below [75]

This process has the advantage of being both consistent as well as adaptable. The COI ceramic system was developed in concert with NASA, Boeing and Rolls Royce and its target application is the exhaust nozzle of Rolls Royce's Trent 1000 engine. The CMC should be able to withstand higher exhaust temperatures than the current titanium alloys in use while providing weight savings over high temperature superalloys which would also be able to operate at that range [75] [76] .

Oxide CMCs are currently only capable of operating at temperatures up to 1100 °C with short jumps to 1200 °C. This is due to limitations from both the fibres and the matrix. The silicon content and grain boundaries of oxide fibres are both prone to degradation at higher temperatures especially if steam content is present. Steam will volatilize SiO_2 into silicon hydroxide which will eat away at the fibres leading to early failure [65]. Higher temperatures will also lead to grain boundary mobility which greatly reduces the creep resistance of oxide based fibres [77]. Sintering of the porous matrix is also a concern at high temperatures, the graceful failure of porous oxide CMCs depends on a weak matrix, significant sintering will provide a stiffer matrix which leads to brittle failure, Figure 12 shows the ductile to brittle transition line for CMCs.

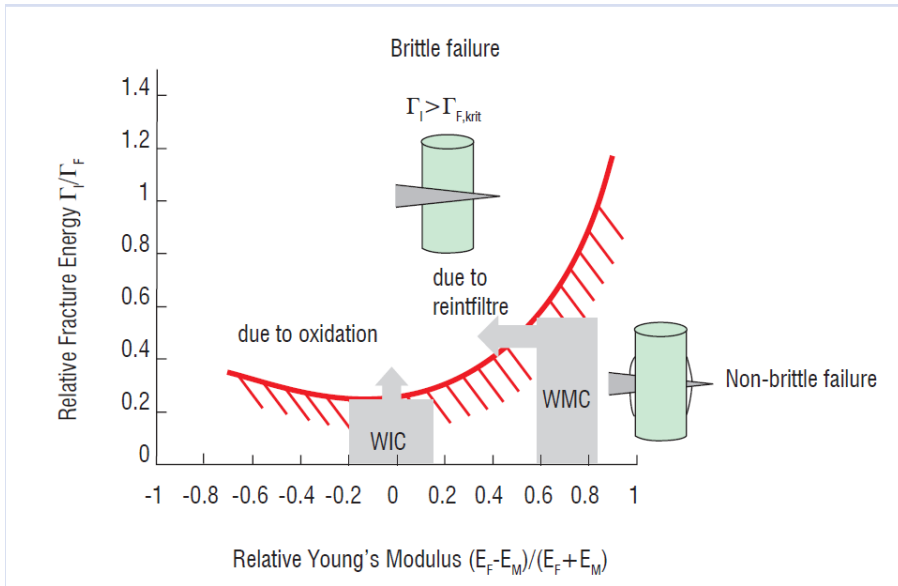


Figure 12: Relative fracture energies of interface to fibres vs. relative young's modulus of fibre to matrix and ductile brittle transition line [78]

To improve the high temperature capabilities of oxide fibres single crystal fibres are being investigated to remove the issue of grain boundary mobility. Beyond sapphire, yttrium aluminum garnet has been suggested as a potential material to base single crystal fibres off of due to its high inherent creep resistance [72]. If oxide systems were to switch to a dense matrix with a fibre coating then the issue of sintering matrices would also be addressed. A third approach to improve the high temperature properties of oxide CMCs is a thermal barrier coating. This approach follows the same principles as that of high temperature metals which require TBCs; however, the oxide resistant ceramic base relieves some of the issues of thermal expansion mismatch and the necessity of an undercoating to provide oxidation protection.

2.3.1.2 Non-oxide/non-oxide Systems

Non-oxide systems depend upon covalent bonding and display higher strengths and greater temperature resistance. The three most utilized non-oxide/non-oxide CMC systems are C/C, C/SiC, and SiC/SiC. For high temperature applications the SiC/SiC system has been the most heavily researched system and has yielded some commercial composites which are being adopted within high temperature machinery. SiC fibres are produced through a polymer precursor which is pyrolysed and sintered or chemical vapor deposition upon a carbon or tungsten monofilament [79]. As with oxide fibres, smaller grain structure will lead to greater strength but lower creep resistance and smaller diameter leads to greater flexibility and ease of forming. Precursor based SiC fibres will tend to have smaller diameters. Nippon Carbon in Japan has a line of precursor based SiC fibres with the trade name Hi-Nicalon™; when treated with electron radiation Hi-Nicalon™ fibres will attain a near stoichiometric mix of Si and C, these fibres are branded Hi-Nicalon™ type-S. Ube Industries and COI ceramics have developed Tyranno SA™ and Sylramic™ SiC fibres respectively. These fibres utilize sintering aids to reduce the residual oxygen content and improve the fibres' properties. An example of a SiC fibre produced through CVD is Specialty Materials' Ultra SCS fibre, which deposits SiC on a carbon monofilament [79].

The most common fibre-matrix interface utilized in SiC/SiC composites is layered pyro-carbon (PyC) and boron nitride (BN). PyC is a carbon structure similar to layers of graphite except PyC still contains some carbon bonds between layers. PyC easily oxidizes at temperatures above 500 °C, so a layer of BN is often applied to protect the interface.

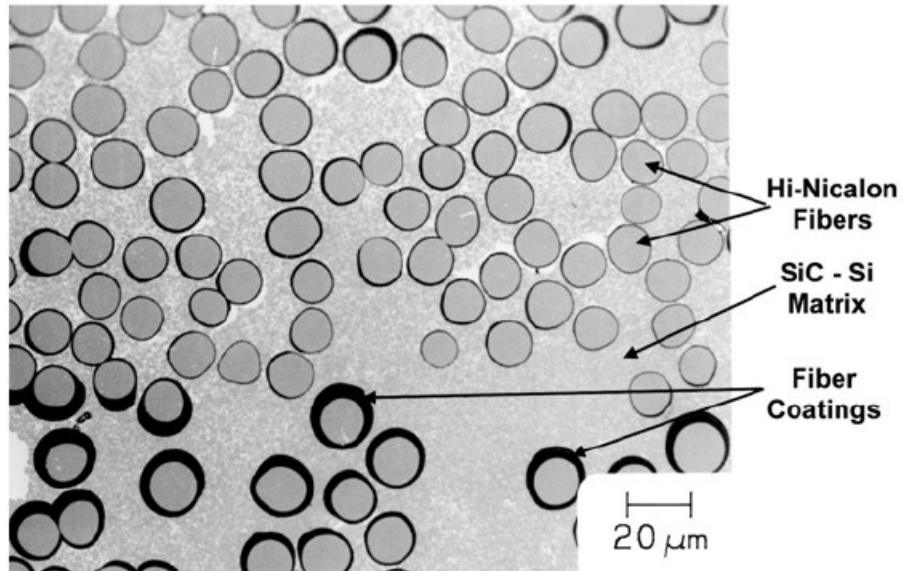


Figure 13: SEM image of melt infiltrated SiC/SiC CMC illustrating fibre coating [9]

The loss of CMC properties to the oxidation of fibres and interfaces is known within the industry as pesting and is a major concern for non-oxide CMCs passing through the temperature range of 500 °C – 900 °C [80]. Under the Ultra Efficient Engine Technologies program undertaken by NASA further work was done to explore non-oxide/non-oxide interface systems. During this work it was discovered that the coatings used to enable fibre forming could leave degrading residue and should be optimized to processing conditions. Further work was undertaken to develop a proprietary BN interface which debonds from the matrix during processing to guarantee a weak interface. To push the intended use temperature range to 1400 °C a polymer infiltration method was used in addition to CVI to produce a matrix with very little free Si content. This prevents the Si from reacting with the BN phase of the fibre interface and forming a strong bond which prevents toughening behavior [81].

Non-oxide matrices are formed using a variety of techniques, the most common involving at least one step of CVI.

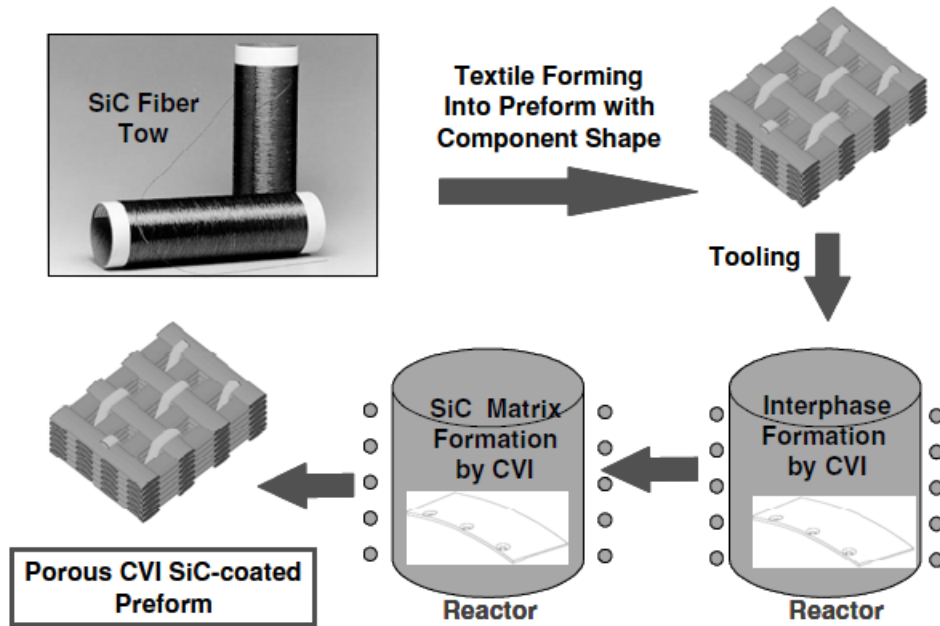


Figure 14: SiC/SiC baseline production method adapted by NASA for their high temperature CMC program [81]

Originally SiC/SiC composites depended almost entirely upon CVI processing; however, as mentioned above, CVI is a slow and expensive process. Other production methods involve infiltration by either slurry, liquid silicon or a polymer precursor, followed by either a drying stage or reaction stage and finally sintering. Liquid silicon and polymer infiltration depend upon chemical reactions during processing to transform the infiltrate into the ceramic matrix [8] [9] [10]. General Electric has developed a process for producing trademarked HiPerComp™ SiC/SiC CMC known as the pre-peg method. In this method the SiC Fibre is coated through CVD and then wound through a wet drum which applies the matrix precursor. The fibre is then laid up in the intended shape and the precursor is pyrolysed, followed by a liquid silicon infiltration. This method produces more reliable CMCs than earlier slurry cast and CVI methods as well as reducing processing times [79].

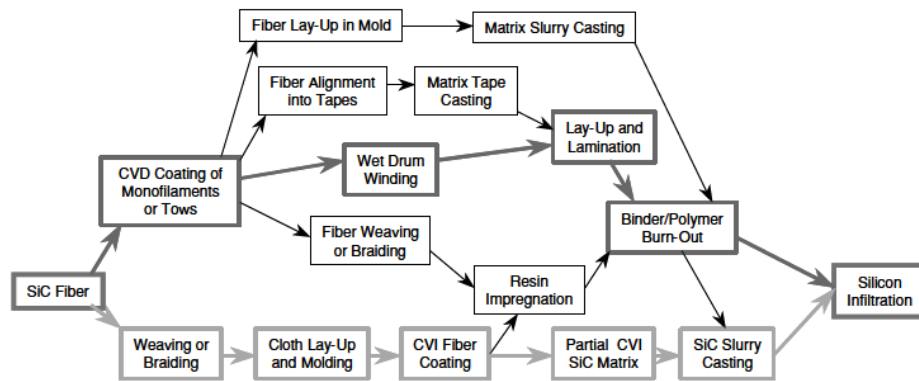


Figure 15: Production routes of GE's HiPerComp™ MI CMC, dark grey path is prepeg process and light grey is slurry cast [9]

Concern over oxygen ingress and embrittlement of non-oxide CMCs has led to the design philosophy of self-healing materials.

2.3.1.3 Self-Healing Materials

In traditional materials damage accumulates until it reaches a critical saturation at which point the component fails as covered in section 2.2.5. To account for damage accumulation traditional materials are either over-designed to reduce the rate at which damage occurs or examined at set periods and replaced when a designated level of damage is reached. Self-healing design philosophy seeks to counter damage accumulation and in some cases reverse it leading to more robust materials. Self-healing is accomplished by designing a constituent within the material to become activated through damage leading to reactions which will repair the damaged area. This can either be an active or passive system. In the active system, the material has a method to detect damage and direct the healing component to that area. In the passive system the healing component is present throughout the system and automatically reacts in damage conditions [82].

High temperature self-healing materials are almost exclusively passive due to the extensive engineering demands already placed upon designing high temperature materials. High temperature self-healing CMCs depend upon oxygen invasion into microcracks which form during use. The ingressing oxygen

reacts with newly exposed reactive layer of the matrix and forms a glass which flows into the microcracks and seals them, creating both a physical and diffusional barrier to further oxygen progression within the matrix shown in Figure 16.

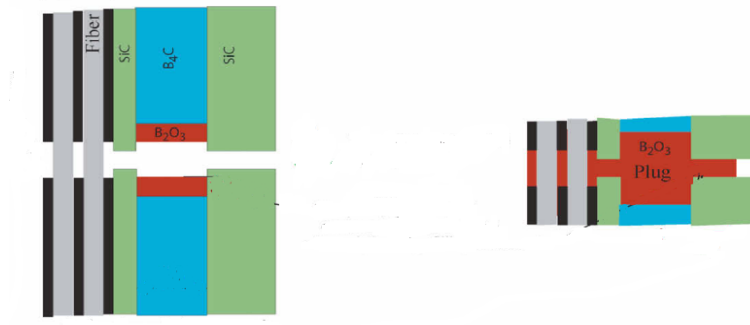


Figure 16: Oxidation of B_4C phase forming a B_2O_3 oxide plug [83]

This design is used to protect fibres and the fibre-matrix interface from oxygen exposure and increases the life expectancy of the CMC. It also prevents a strong bond forming between the matrix and fibre due to the oxidation of the interface, this strong bond leads to brittle failure. The compounds most commonly used to react with the oxygen are B_4C and SiC, which form B_2O_3 or SiO_2 respectively. These compounds are either already present within the matrix or layered into the matrix using alternating CVI pulses, a layered microstructure is shown in Figure 17.

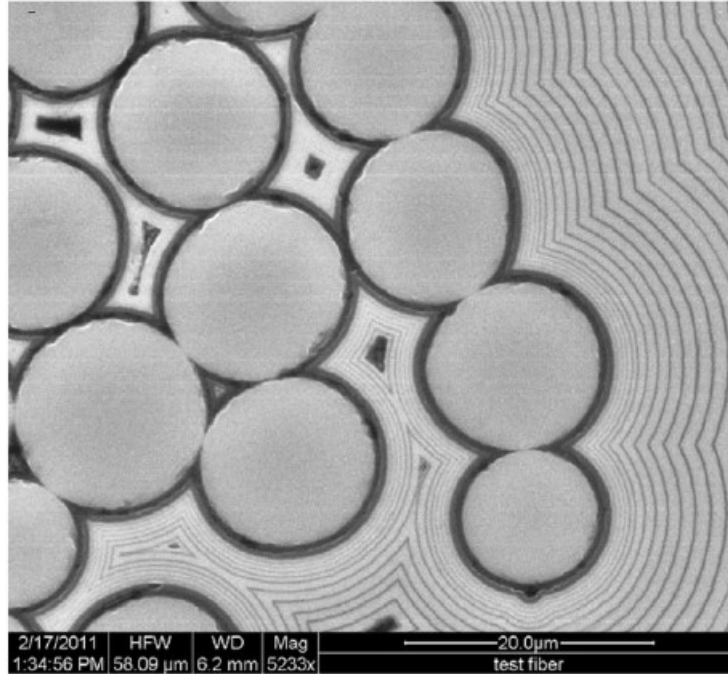


Figure 17: Alternating layers of SiC and B₄C self-healing matrix deposited through CVI [84]

The reactive constituent must be able to react with the ingressing oxygen and form a plug which will prevent further oxidation. To optimize this behavior one must know possible reactants and products, reaction kinetics, oxygen diffusivity in the most likely products, viscosity of the glass which forms, compatibility of the glass with any composite phase it may come in contact with, and thermal and mechanical fatigue behavior of the composite glass system. Phase diagrams are invaluable tools in predicting what products may occur when oxygen encounters the reactive layer at a high temperature; however, intermediary reactions, catalysts and the effect of pollutants within the fuel stream may also play a role in determining the products. Reaction kinetics are crucial in determining both the rate of formation of the target glass as well as how quickly the target glass may volatilize in the conditions or the rate of reaction of the glass with other constituents within the matrix. At high enough temperatures there is competition between the rate of new liquid glass formation from the reactants and the volatilization of the current liquid glass acting as a plug, if the volatilization reaction starts to outpace the formation of new plug then the matrix will cease to be self-healing and degradation of the fibres and

interphases will proceed more rapidly. Volatization is a major concern for composites incorporating a SiO_2 phase operating in steam environments because silica is prone to forming silica hydroxide. Furthermore, the oxide plug should be designed to avoid degrading fibres and interfaces itself as shown by Quemard et al [85].

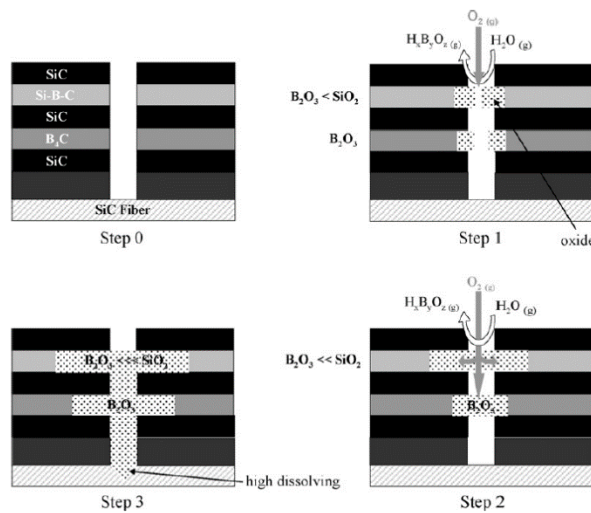


Figure 18: Self-healing mechanism of Si-B-C, B_4C , SiC CMC Step 0) microcracks develop in the matrix Step 1) Oxygen and moisture ingress leads to the formation of oxides Step 2) oxide plug grows and fills the crack Step 3) crack is sealed by the oxide, there is high dissolving of the SiC fibre [85]

The diffusivity of oxygen within the glass that forms is another obvious concern since the goal of a self-healing matrix is to prevent further oxidation of important constituents. Viscosity of the product is directly related to the glass's ability to infiltrate microcracks through capillary effects. Finally the healing effect should be stable throughout the loading and temperature profiles the CMC can be expected to cycle through within its lifetime. The coefficient of thermal expansion, the solidification and bonding of the glass to the matrix upon cooling will all affect the CMC's lifetime.

2.3.1.4 Environmental Barrier Coatings

Environmental Barrier Coatings (EBC) are crucial for high temperature non-oxide CMCs. SiC based CMCs can depend upon passive SiO_2 scale forming in oxidative atmospheres; however, moisture content in the combustion atmosphere at temperatures above $1100\text{ }^\circ\text{C}$ will lead to material loss through the

volatization of silicon hydroxide as the SiO_2 reacts with H_2O . Carbon based CMCs will oxidize above 1000 °C with any oxygen content present offering an even greater challenge. To prevent material loss and failure due to oxidation highly stable environmental barrier coatings are employed. The most common EBC currently in development is based off a Si/mullite/BSAS architecture, where BSAS is $((1-x)\text{BaO} \cdot x\text{SrO} \cdot \text{Al}_2\text{O}_3 \cdot 2\text{SiO}_2, 0 \leq x \leq 1)$ [86]. BSAS coatings were chosen for low silica activity within BSAS to prevent volatization, and closely matching coefficients of thermal expansion to prevent cracking and spallation. Currently the Si/mullite/BSAS EBC is applied using atmospheric pressure plasma spraying which has drawbacks of requiring surface roughness for a good bond to form and being a line-of-sight application process. Surface roughness is provided by mechanical abrasion or chemical etching, both techniques reduce the flexural strength of monolithic ceramic specimen. Line-of-sight application techniques are difficult to adapt to complex part geometries. Research is being conducted into slurry and sol-gel based methods of applying EBCs as well as different EBC architectures [87] [88] [89]. The primary concern with slurry based and sol-gel application methods is adequate coating thickness, uniform distribution, and sintering mechanics. The viscosity of the slurry will affect the thickness and uniformity. Particle size and chemical composition will affect the sinter mechanics [87].

2.3.1.5 Fibre Layup

The alignment of the fibres will also affect the properties of the composite. Many different patterns of alignment have been explored in composites based off of polymers. When adapting these alignments for ceramics it is important to adjust for the lower strain to failure seen in most ceramic materials. A consequence of this ceramic property is patterns which require sharper bends in the fibre such as the woven knot pattern have the potential to lead to fibre failure at lower than predicted stresses. A second issue with more complex layup patterns is the degradation of the interface, and the difficulty of matrix

infiltration. As such, the most common layup pattern in modern CMCs is the $0^\circ/90^\circ$ alternating layers which provides strong biaxial properties.

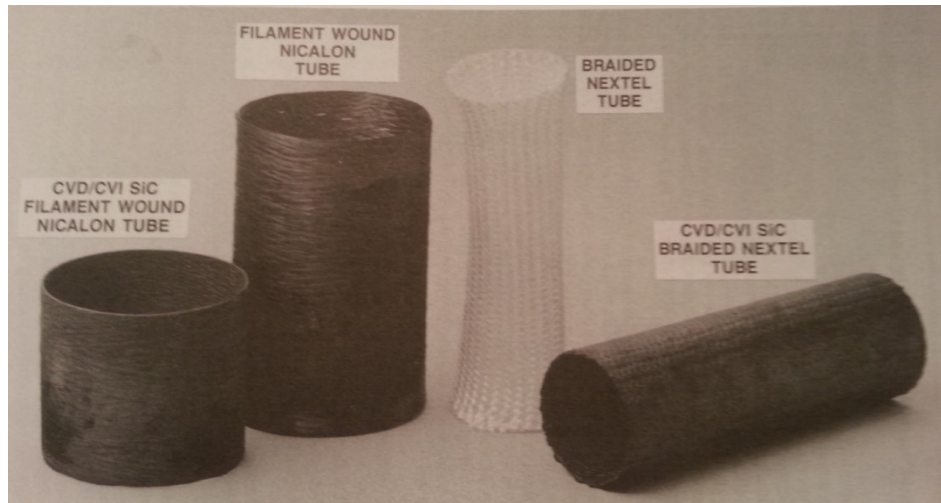


Figure 19: Different weaves of CMC fibre: tubes on the left exhibit 1D wound fibre, the tubes on the right exhibit a 2D braided weave structure [90]

2.3.2 Discontinuous CMCs

Discontinuous CMCs are ceramic systems which do not use continuous fibres for reinforcement. The goal of discontinuous systems is often to increase the toughness of the ceramic system; however, the improvement of functional properties such as optics or piezoelectric effect may also be the goal. The earliest breakthrough in improving toughness for discontinuous CMCs was the discovery of transformation toughening within the partially stabilized zirconia regime, which could be included as a secondary phase in other ceramics. Further advances have been obtained through the incorporation of whiskers, which are high aspect ratio single crystal constituents, layering different phases of ceramics (either laminated or functionally graded ceramics) and alloying intermetallic compounds with reinforcing covalent phases. The improvements given by transformation toughening will be evaluated in more detail in sections 2.3.3.

There are two principles which work to improve the toughness of laminate layered ceramics, the first is to provide incoherent boundaries between the layers which provide preferential crack progression paths. This both provides an increase in crack length and consequently required crack propagation energy as well as creating a pseudo-fibre pull-out effect between layers.

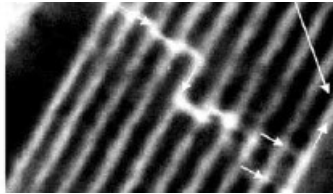


Figure 20: Crack deflection along a multi layered interface [91]

The second principle in operation is a slight thermal expansion mismatch between layers which creates tensile and compressive stress fields within the ceramic. Tensile stress fields provide a preferential crack progression path, and compressive stress fields slow crack propagation by exerting a crack closing force. Functionally graded ceramics (FGCs) operate with coherent and semi coherent interfaces between each layer. The intent of FGCs is to provide a composite which pairs the strength and hardness of one constituent, usually at the exposed end, with the toughness of the second constituent; mimicking natural structures such as tree bark or bones [92] [93].

There are several processing routes through which layered and FGC CMCs can be manufactured. Both layered ceramics are produced by layering during the green forming stage, laminates are produced with as little interaction between layers as possible while FGCs are engineered to ensure smooth transitions between phases. The most common processing methods for producing layered ceramics are tape casting, centrifugal casting, slip casting, and electrophoretic deposition [94]. For each of the processing techniques, individual layers are produced in slurry form and then applied to the existing layer; the composite is then compressed and sintered. Compressing can either be cold or hot, with hot pressing incorporating the sintering process. Attention needs to be paid to the thermal expansion mismatch of

coinciding layers to prevent early and unwanted cracking. Further concerns include defects within the ceramic which may come about as part of the processing, the relative sintering curves of each layer to ensure the ceramic is sintered as fully dense as possible without excess coarsening [95] [96].

Intermetallic compounds have also been investigated for use as high temperature structural materials. MoSi_2 has been identified as one of the most promising of these compounds due to its oxidation resistance, creep resistance and high melting point [97]. The Melting point of MoSi_2 is 2020°C when it is in its hexagonal phase, its tetragonal phase is stable from room temperature to 1900°C [98]. One significant issue with using MoSi_2 in oxidative environments is the intermetallic break down at temperatures below 1100°C due to pest oxidation. In this process MoSi_2 transforms into MoO_3 which expands and cracks the MoSi_2 matrix [99]. Above 1100°C oxidation becomes less of a concern as a protective SiO_2 scale is able to form. One strategy adopted to prevent pest oxidation is to alloy MoSi_2 with Si_3N_4 which allows a protective SiON_2 scale to form before pest oxidation. Alloying Si_3N_4 can further improve the toughness and reduce the CTE of MoSi_2 which is desirable for high temperature applications. Further, $\text{MoSi}_2/\text{Si}_3\text{N}_4$ compounds can be used as the matrix phase with SiC fibres due to the reduced thermal expansion mismatch caused by the addition of the Si_3N_4 phase. The fibre reinforced $\text{MoSi}_2/\text{Si}_3\text{N}_4$ composite has many of the same advantages and disadvantages as SiC/SiC composites covered in section 2.3.1.2. Another advantage offered by MoSi_2 based composites is the electrical conductivity of the MoSi_2 phase, this allows the use of electrical discharge machining for shaping as well as some functional applications such as diesel engine glow plug [97].

Much work has been done to develop and characterize ceramic composites with discrete additions. Some of the more common systems encountered include an alumina or mullite matrix with SiC additions either in the form of particulates or whiskers. The mechanisms of whisker toughening have been thoroughly explored and reported upon in the literature. Whiskers enhance the toughness of ceramics

by absorbing energy involved in crack propagation. This energy is absorbed primarily through five mechanisms which are crack deflection, crack bowing, microcracking, whisker pullout and crack bridging. The contribution of microcracking, which occurs when stresses caused by coefficient of thermal expansion mismatch, has been modeled by equation (29) [100].

$$\frac{dK_c}{K_c} = \left\{ \left[k_1 - \left(\frac{5}{8} \right) \right] \left[\left(\frac{G}{G^*} \right) - 1 \right] + \left[k_2 + \left(\frac{3}{4} \right) \right] \left[\left(\frac{\nu^* G}{G^*} \right) - \nu \right] \right\} / (1 - \nu) \quad (29)$$

Where K_c is the toughness prior to microcracking, k_1 and k_2 are constants depending upon the shape of the microcracking zone and G and G^* are shear moduli prior to and post microcracking, ν and ν^* are the Poisson's ratios prior to and post microcracking. Microcracking contributes to toughening only if a propagating crack is deflected by micro-cracks. Furthermore the micro-cracks must be small enough that they do not initiate crack propagation themselves. Crack deflection is a mechanism which increases toughening by increasing the length the crack must travel by altering its path. Crack deflection is most commonly caused by internal stress fields within the composite which are created by thermal expansion mismatches encountered during cooling. Crack bowing is the theoretical extension of the crack length as it encounters a stiffer second phase as shown in Figure 21.

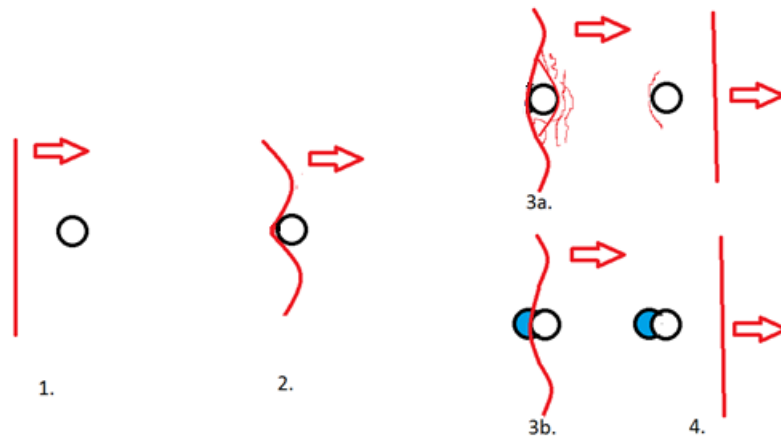


Figure 21: Crack bowing: 1. crack approaches stiff inclusion. 2. extra crack energy is absorbed as the crack length increases while bowing around stiff inclusion. 3a. crack continues past inclusion by propagating cracks ahead of the inclusion and joining them. 3b. crack continues past inclusion by shearing it. 4. crack continues

The greatest contributions occur due to whisker pullout and crack bridging. Both these mechanics absorb energy through friction between the whisker and matrix interface as the crack propagates perpendicular to the whiskers. Crack bridging is distinguished from whisker pullout as the effect caused by intact whiskers behind the crack tip lead to a closing force retarding crack, this is visually represented in Figure 22.

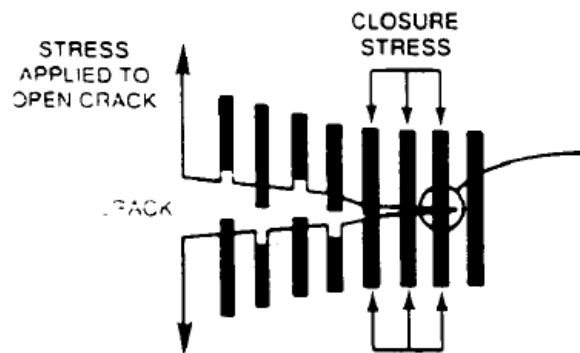


Figure 22: Fibre pullout and crack bridging toughening mechanisms in CMCs [21]

Fibre pullout or crack bridging will only activate in composites where the interface is sufficiently weak to ensure the fibre pulls-out rather than fractures; the fibre must also be aligned along the path of the crack. This mechanism is apparent both in composites reinforced by whiskers and continuous fibres and is much more apparent in the latter system. Equation (30) developed by Betcher et al models the toughening by the addition of whiskers due to crack bridging [100].

$$dK_b = \left\{ \left[K_0^2 + 4E_m V_f (\sigma_f^w)^2 l_{DB} / (1 - \nu^2) E^w \right]^{1/2} - K_0 \right\} / 2 \quad (30)$$

Where K_b is the fracture toughness of the composite, K_0 is the matrix toughness, E_m and E^w are matrix and whisker elastic moduli respectively, σ_f^w is the strength of the whisker, V_f is the volume fraction of whiskers perpendicular to crack path, ν is the Poisson ratio of the composite, and l_{DB} is the debond length. It can be seen that increasing the strength, volume fraction, or debond length of the whiskers will lead to greater toughening [100].

The overall toughening effect of whiskers is the sum of each individual toughening mechanism. With the correct optimization of whisker content and geometry, toughness has been seen to improve by 50% in a ZTA system reinforced with SiC whiskers [101]. In plain alumina, 20 vol% SiC whiskers were found to improve the fracture toughness to 6.5 MPa m^{1/2} from ~3.5 MPa m^{1/2} of pure alumina [102].

Whiskers have also been shown to reduce the creep rate within ceramics. It has been hypothesized that this is due to intergranular whiskers locking grains in place, preventing the grain boundary sliding mechanism inherent in ceramic creep [44]. However, this effect can be reduced if the volume fraction of whiskers is too great; as whisker-matrix interfaces being favorable sites for void growth. At around 20% volume fraction the contribution of whiskers to creep resistance has been found to be the greatest [44]. Porter found that a 5% volume addition of SiC whiskers in alumina led to a creep rate reduction of

2 orders of magnitude and that 15% volume addition altered the creep mechanics and delayed the transition to stage II creep [103].

2.3.3 Ceramic Matrix

The matrix of the composite must exhibit desired properties at the temperature of 1200°C. Hillig has created a criterion for ranking different oxides on their high temperature suitability for structural ceramics [104]. This system is based upon melting temperature, elastic modulus to density ratio, and volatility, to generate a maximum temperature at which that oxide can operate. Hillig's results are shown in Table 4 [21].

Table 4: Hillig's Criteria for Ranking Oxides [104]

Oxide	T_m	Creep		E/ρ	Volatility	T_{max}	Rank
		$0.85T_m$	$0.7T_m$				
ThO ₂	3493	2970	2445	2290	2375	2290	3
HfO ₂	3117	2650	2180	2020*		2020	6
UO ₂	3113	2645	2180	2050		2050	5
MgO ₂	3098	2635	2170	2870	1825	1825	9
ZrO ₂	3037	2580	2125	2195	2775	2195	4
CaO	2882	2450	2015	2430		2430	1
BeO	2843	2415	1990	2710	2325	2325	2
SrO	2727	2320	1910	1750	2075	1750	10
Al ₂ O ₃	2327	1980	1630	2210		1980	7
Cr ₂ O ₃	2300	1955	1610	2015		1955	8

*Assume that E is the same as that reported for ZrO₂.

It can be seen that six different oxides rank higher than alumina on Hillig's scale; however, if secondary performance indices are included alumina becomes much more desirable. These secondary considerations are price, workability, compatibility, and available literature.

Calcium oxide, beryllium oxide, and thorium oxide are the three highest ranked oxides according to Hillig's criteria. Calcium oxide is highly reactive with water and not suitable as a structural oxide. Thorium oxide is very rare, as it is mainly produced in nuclear reactions; it is also radioactive due to its thorium content. Beryllium oxide is already used in specialised high temperature applications especially

in electrical components due to its high thermal conductivity; however, it is far more expensive than alumina. The other three oxides ranked higher than alumina include zirconia, uranium oxide, which is heavily controlled due to its military applications and hafnium oxide, which reacts with chlorine at high temperatures.

A quick overview of alumina's polycrystalline bulk ceramic properties is provided in Table 5.

Table 5: Selected Property Values for Sintered Fully Dense α -alumina [105]

Property	Temperature		
	20 °C	1200 °C	1500 °C
Elastic Modulus (GPa)	416	354	338
Density (g/cm ³)	3.984	3.868	3.834
Flexural Strength (MPa)	380	300	130
Fracture Toughness (MPa·m ^{1/2})	3.5	2.6	2.5
Hardness Vickers, 1 kg (GPa)	15	3.7	2.5
Creep rate at 150 MPa (x10 ⁻⁹ ·s ⁻¹)	0	280	24600
Thermal Expansion Coefficient (10 ⁻⁶ ·K ⁻¹)	4.6	8.3	8.6
Weibull Modulus	11	11	11

Although alumina has many favorable properties, its low fracture toughness, and proneness to coarsening are major concerns. One solution is to create a mechanical mixture of alumina and partially stabilized Zirconia (PSZ). This composite is known as Zirconia Toughened Alumina (ZTA) and has been widely studied as a tougher alternative to alumina [106] [107].

The history of ZTA ceramics has been covered very well in Wang and Stevens' review of ZTA ceramics [54]. The primary mechanisms which enhance ZTA include a martensitic transformation toughening mechanism of the PSZ, the grain boundary pinning of alumina grains by PSZ inclusions which retard grain growth and grain boundary sliding in creep, and the creation of internal stresses within the matrix due to coefficient of thermal expansion mismatch which leads to toughening.

The martensitic transformation toughening of ZTA is the primary room temperature toughening mechanism which PSZ imparts upon the alumina. This mechanism occurs through the stress activated conversion of tetragonal zirconia to monoclinic, with an accompanying volume expansion of ~4% [54]. The overall contribution to toughening of this effect has been modeled by either equation (31) or equation (32) [108].

$$\Delta K_c = 0.21 E e^T V w^{1/2} / (1 - \nu) \quad (31)$$

$$\Delta K_c \approx \left[\frac{0.44}{\pi(1 - \nu)} \right] E e^T V w^{1/2} \tan^{-1} \left(\frac{\Delta a}{w} \right) \quad (32)$$

Where ΔK_c is the change in toughening, E is the elastic modulus of alumina, e^T is the dilation strain associated with the transformation, V is the volume fraction of tetragonal zirconia, w is the transformation width, and Δa is the crack advance. Equation (32) is employed to model the accompanying change in R-curve behaviour due to the zirconia addition.

There is extensive literature published on ZTA composites with varying levels of alloying and different processing techniques. This literature has been surveyed to determine the zirconia alumina ratio which would yield the greatest fracture toughness at room temperature while still ensuring adequate strength. Results from Claussen's work in 1976 show an optimal volume fraction of 12 % for 0.03 μm and 16% for 1.25 μm unstabilized ZrO_2 inclusions shown in Figure 23.

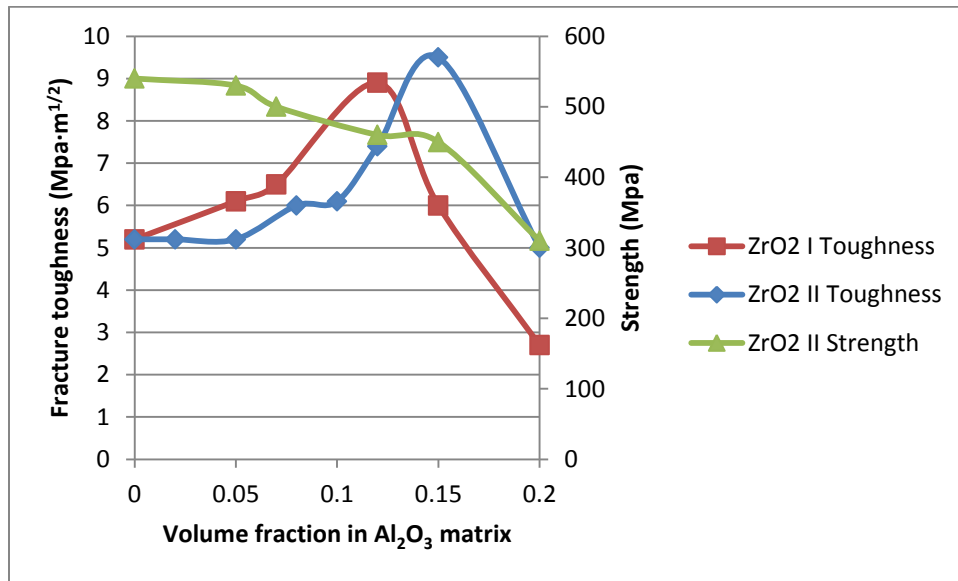


Figure 23: Fracture toughness and strength of alumina matrix containing I) 0.30 μm II) 1.25 μm unstabilized zirconia particles as a function of the volume fraction of zirconia additions [54] [109]

Subsequent work has shown the primary toughening mechanism of stabilized ZTA is the generation of microcracks within the composite through the tetragonal monoclinic transformation [54]. Work by Wang and Stevens has led to the development of equation (33) used to determine the relationship between crack development and size and degree of stabilization of zirconia inclusions [110].

$$X = R \left[\left(1 + \frac{\theta^2 \Psi^2 R}{\Pi \gamma} \right)^{1/2} - 1 \right] \quad (33)$$

Where X is half the toroidal crack length, R is the size of the zirconia inclusion, Ψ is the degree of stabilization, γ is the fracture surface energy of alumina, Π is the reciprocal modulus of the composite

and θ is a constant [54]. Although an increase in vol% of zirconia inclusions can lead to toughness increase, it has an effect of reducing the strength at the same time. This is illustrated by Figure 24 from work done by Wang and Stevens; it can be seen that a significant drop in strength occurs around 12 vol% of stabilized zirconia.

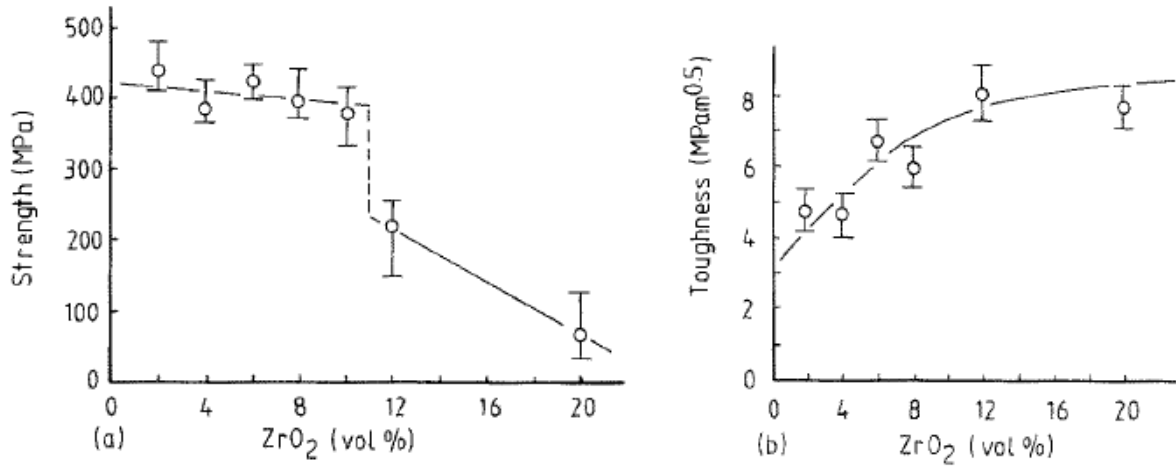


Figure 24: Vol % inclusion of ZrO₂ in Al₂O₃ matrix plotted against a) strength and b) toughness [54]

The loss in strength is due to the increased occurrence of inhomogeneity within the composite which could lead to crack initiation and propagation. Furthermore, inclusions above a critical volume fraction V given by equation (34) will lead to crack link up and coalescence which will greatly compromise the strength of the ceramic.

$$V_c = 0.52 \left(1 + \frac{\theta^2 \Psi^2 R}{\Pi \gamma} \right)^{-3/2} \quad (34)$$

To ensure an increase in toughness without overly compromising the strength of the composite a volume fraction of 10.66% stabilized ZrO₂ has been selected. This is the equivalent of a 15 wt% of ZrO₂.

2.3.4 Whiskers

The majority of the work done in strengthening high temperature ceramics has been done with SiC whiskers due to their ease of production and availability. The two primary oxide whiskers incorporated into high temperature materials are Al₂O₃ and mullite [111] [112] [113], while carbon nanotubes have attracted some attention due to their unique properties [36]. Table 6 compares relevant properties of the four primary strengthening whiskers used in modern CMCs.

Table 6: Whiskers available for reinforcement of oxides [36] [100] [114] [115] [116] [117] [118] [119]

Whisker	E (Gpa)	Production Method	Notes
SiC	580	Liquid-Vapor-Solid Method, pyrolysis of rice husks	Prone to oxidation above 1200°C Most common reinforcement Commercially available
Carbon Nanotubes	1000	Chemical Vapor Deposition	Prone to oxidation above 1000°C Properties vary depending upon single wall or multi-wall Commercial production is still in its infancy
Alumina	430	Grown through boehmite gel	Transforms into large elongated crystals in alumina matrix Commercial production is still in its infancy
Mullite	170	Molten Salt Method	Highly stable in oxidizing conditions Compatible with alumina and zirconia

Mullite has been selected in this research as the material for the whisker phase of the composite. The selection was made due to mullite's stability at temperatures above 1100 °C despite its low elastic modulus. Mullite is the common name of a mineral that occurs in the alumina-silica system. Mullite commonly takes one of two stoichiometric forms of 3Al₂O₃·2SiO₂ or 2Al₂O₃·SiO₂. Microstructurally, mullite is defined by the orthorhombic crystal symmetry with *a* and *b* values of .755 nm and .769 nm

respectively, the c value is typically 0.289 nm. Structurally, mullite is composed of edge sharing Al-O octohedra at the corners and centre of each unit cell parallel to the c -axis. These unit cells are cross linked by Si-O and Al-O corner sharing tetrahedra. This structure is distorted by Si^{4+} anions being replaced by Al^{3+} resulting in oxygen vacancies to maintain charge neutrality, the random distribution of Si and Al tetrahedra leads to corner sharing arrangements of oxygen deficient tri-clusters where three tetrahedra share one oxygen cation, a visual representation of the structure of mullite can be found in Figure 25 [120].

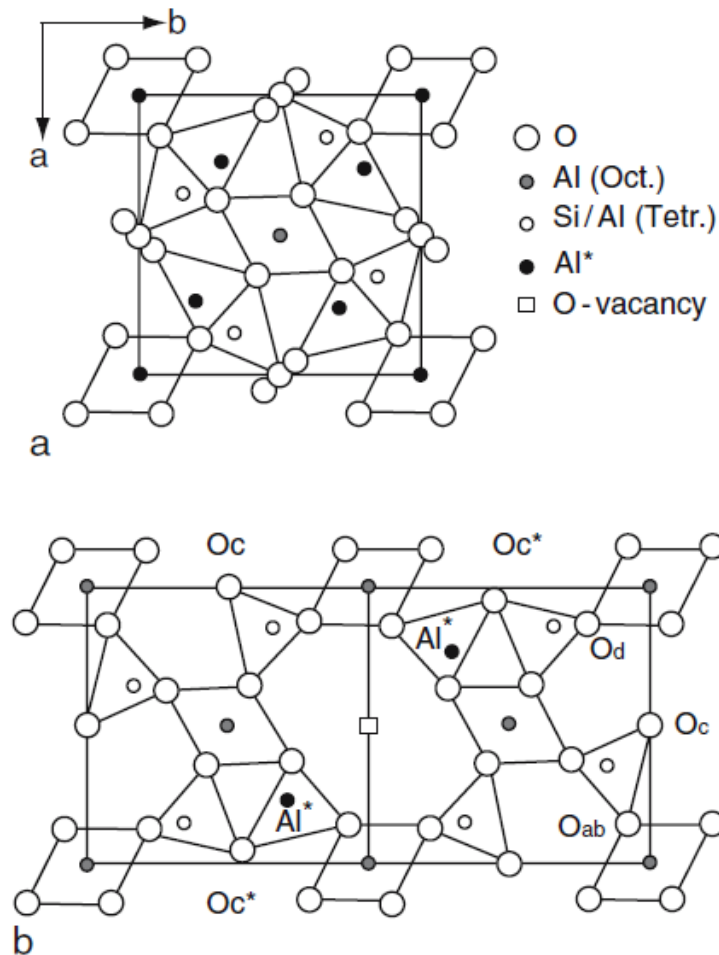


Figure 25: a) Standard mullite structure b) mullite structure arranged around an oxygen vacancy [121]

The binary phase diagram of the alumina-silica system has been mapped and is shown in Figure 26.

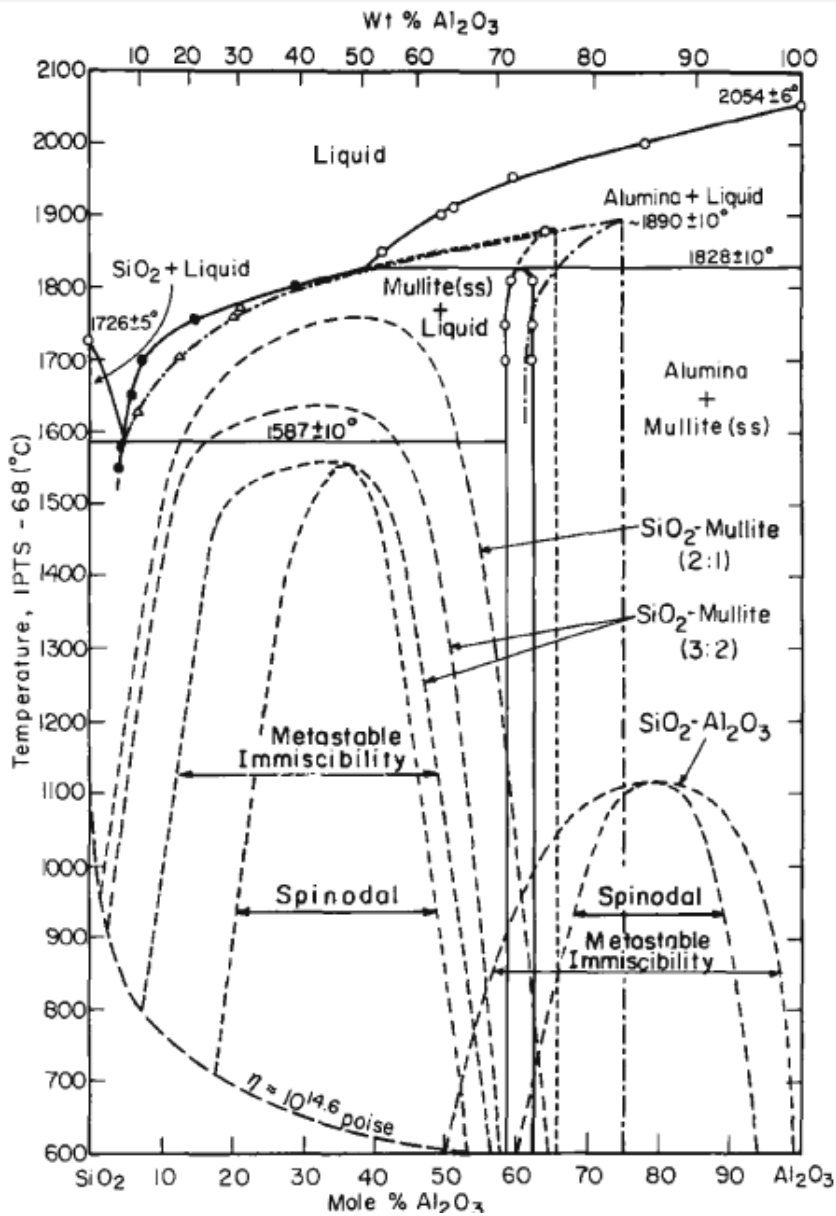


Figure 26: Binary Phase Diagram of alumina-silica System [122]

Mullite has attracted interest as a material for high temperature applications because its stable microstructure allows it to maintain excellent creep properties. This is due to the ingrained oxygen vacancy structure which shows little reliance upon temperature [123]. The mechanical properties of mullite at various temperatures are shown in Table 7.

Table 7: Fracture toughness (K_{ic}), fracture strength (σ_f), flexural strength and microhardness of 3:2 mullite at different temperatures [120]

T (°C)	K_{ic} (MPa m ^{1/2})	σ_f (MPa)	Flexural strength (MPa)	Microhardness (GPa)
22	2.5 ± 0.5			15
1000				10
1200	3.6 ± 0.1	260 ± 15	500	
1300	3.5 ± 0.2	200 ± 20		
1400	3.3 ± 0.2	120 ± 25	360	

2.4 Processing

The goal of this work has been to design a low-cost, high temperature CMC; it is therefore important to take the processing into account as this may greatly add to the cost and difficulty of producing the desired material. The proposed route has followed the path of powder selection, high energy ball milling, colloidal processing, followed by a sintering profile to ensure theoretical density.

2.4.1 Colloidal Mixture

A colloid is a dispersion in which at least one dimension of the dispersed phase is within the nano scale. Many different colloidal routes for processing ceramics have been developed and each has its benefits and drawbacks. Table 8 gives a quick overview of the most common and contemporary colloid processing methods and compares their consolidation mechanisms and the forms which can be produced by them.

Table 8: Different Colloidal Processing Routes [124]

Forming method	Consolidation mechanism	Component shape
	A. Fluid removal	
Slip casting	Fluid flow into porous mold driven by capillary forces	Complex, 3D, thin walled
Pressure filtration	Fluid flow through porous filter driven by an applied pressure	Simple, 3D
Osmotic consolidation	Fluid flow through a semipermeable membrane driven by osmotic pressure difference	Simple, 3D
Tape casting	Fluid removal due to evaporation	Simple, 2D, thin layers
Robocasting [†]	Fluid removal due to evaporation	Complex, 3D
	B. Particle flow	
Centrifugal consolidation	Particle flow due to applied gravitational force	Complex, 3D
Electrophoretic deposition	Particle flow due to applied electric field	Simple, 2D or 3D
	C. Gelation	
Aqueous injection molding (AIM)	Physical organic gel forms in response to a temperature change	Complex, 3D
Gelcasting	Cross-linked organic network forms because of chemical reaction	Complex, 3D
Direct coagulation casting (DCC)	Colloidal gel forms because of flocculation	Complex, 3D
Robocasting [†]	Colloidal gel forms because of flocculation	Complex, 3D

[†]Solid freeform fabrication technique (consolidation can be induced via mechanism A or C).

The suspended particles have a relatively large contact area which can influence colloidal behaviour. With a strong understanding of the competing forces within a suspension ceramic process engineers can tailor the properties of the colloid to produce a ceramic microstructure with desirable properties [125]. As such it is important to understand the various forces within a colloidal system and how they affect the final product which is produced.

The interparticular forces which occur within the suspension include van der Waal, electrostatic, steric, and structural. Van der Waals interactions are the long range attractions between particles. Electrostatic forces are caused by the charge of the particles and lead to particle separation. Steric forces occur through the repulsive interactions between polymeric adlayer coating suspended particles. Structural forces control the suspension stability and are caused by non-absorbed species within the suspension, examples from the current research being alumina and zirconia particles coated with a dextrin adlayer [124]. This research is primarily focused upon using colloidal processing to reduce agglomeration of nano particles, creating a more uniformly dispersed microstructure and retaining nanoscale grains. Both steric and electrostatic forces are optimised to achieve this effect. Work done by Safinajafabadi et al has shown that the organic compound dextrin, derived from sugar is an effective polymer for maximizing steric forces [126]. The molecular formula of Dextrin is pictured in Figure 27.

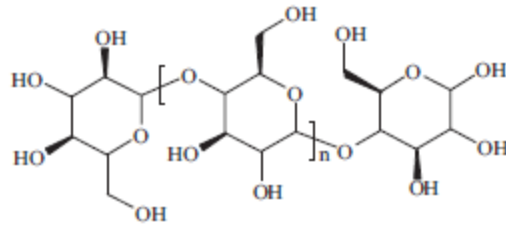


Figure 27: Organic structure of Dextrin [126]

Dextrin is absorbed by the surface of the alumina and zirconia particles to create a repulsive adlayer preventing agglomeration. Further repulsive potential is induced by controlling the pH of the solution. It can be seen from the zeta potentials shown in Figure 28 that at pH level above 12 and below 3 electrostatic repulsion between suspended ZTA powders is maximized [126] [127].

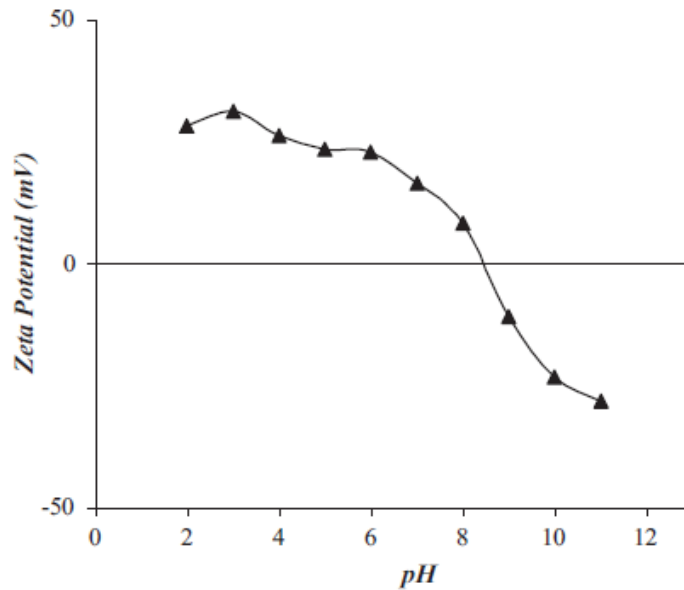


Figure 28: Zeta potential of ZTA mixture in aqueous solution with Dextrin as a dispersant [126]

Certain forming techniques will require a proper analysis and adjustment of the flow properties or rheological behavior of the colloid. This is especially important in near net shape applications such as injection mold casting and robocasting. The rheological behavior is derived from the apparent viscosity,

the yield stress under shear and compression, and the viscoelastic properties; these are controlled by the suspension, structure and stability of the colloid.

The consolidation and drying of the colloid will have a large effect on the final properties of the sintered ceramic, it is therefore important to control these processing steps carefully. The approach to consolidation employed in this research is through fluid removal, although consolidation through gelling will also be examined with the goal of reviewing gel casting as a potential processing technique.

This system relies upon a vacuum to create a pressure differential across the filter and remove the liquid. After 24 h of filtration the solid phase has effectively blocked all channels of fluid flow reaching the filter and evaporation is employed to remove the remaining fluid. Gel casting relies upon gelling to consolidate the colloid, the advantage is a near net shaped green compact with a much stronger elastic modulus which allows for green machining. In gel casting a chemical gelation method is induced to create a polymeric network which captures and retains the ceramic powder phase. The procedure relies upon a precursor monomer organic, which is polymerized through a combination of a chemical and thermal reaction, creating the network [124]. Chabert et al. have had success using a polyvinyl alcohol solution cross linked by adding 2,5-dimethoxy-2,5-dihydrofuran and heating to 60 °C, in this work complex rotor shapes were formed and green machined before sintering [128]. In preformed bodies the drying stage must be carefully engineered to avoid stress concentrations and cracking in the green body. The drying of a formed consolidated colloid is achieved through evaporation, diffusion and capillary action transporting liquid from the inside of the body to the evaporative layer. When the rate of evaporation exceeds the rate of capillary liquid transport, liquid meniscus collapses back into the capillaries and is removed through vapor phase diffusion.

2.4.2 Whisker Growth

Mullite whiskers have been formed through several methods including thermal decomposition, sol-gel processing, in situ formation, and high energy ball milling. The molten salt method (MSM) was selected for this work because the temperature needed is relatively low and the method can be completed in an air atmosphere. Zhang et al original research in 2010 showed that MSM could be adapted to produce mullite whiskers and the work has been followed up with several additional studies examining the optimization of precursors [129] [130] [131]. Molten Salt method uses salt sources of aluminum ion, oxygen, a salt flux, and a source of silica. The most successful flux so far has been Na_2SO_4 , while $\text{Al}_2(\text{SO}_4)_3 \cdot 18\text{H}_2\text{O}$ has been used as the source of alumina and oxygen ions and various forms of silica have been employed. The precursors are mixed in an alumina crucible and heated to 1000 °C at a rate of 3.3 °C/min. The mixture is held at 1000 °C for 200 min then returned to room temperature. To obtain the whiskers the Na_2SO_4 which has formed is washed off using boiling water. The agglomerated whiskers are then separated in an ethanol mixture using ultrasonic agitation.

Molten salt method works through the melting of the precursors followed by seeding of mullite crystals and growth along the (111) crystal plane resulting in mullite crystals with a high aspect ratio. The work by Zhang et al. examined the melt mixture using differential thermal analysis (DTA) and thermogravimetric analysis (TG) to examine the thermodynamics of the melt process, their results are shown in Figures 29 and 30.

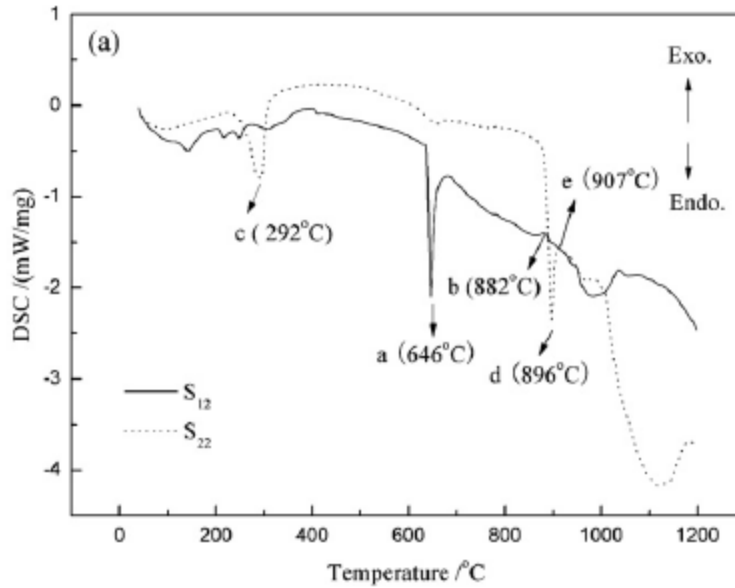


Figure 29: Differential thermal analysis of $\text{Al}_2(\text{SO}_4)_3$, SiO_2 , Na_2SO_4 in ratio 2:1:8 (S_{12}) and $\text{Al}(\text{OH})_3$, SiO_2 , Na_2SO_4 in ratio 2:1:8 (S_{22}) [130]

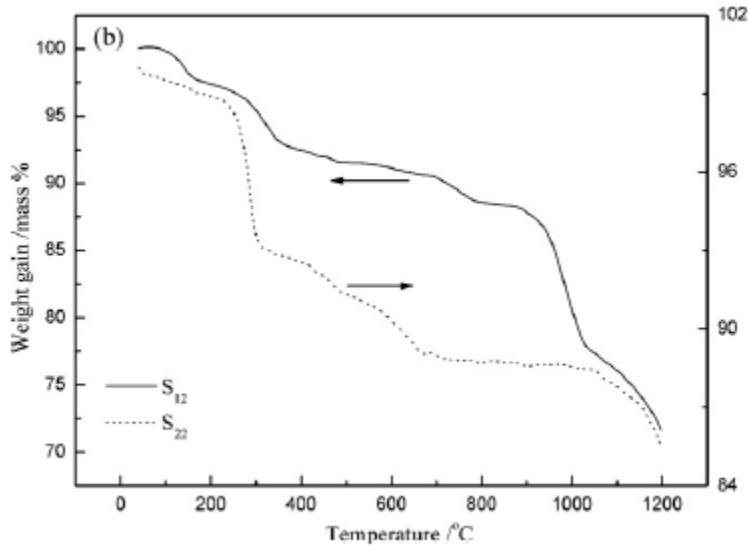


Figure 30: Thermo gravimetric analysis of $\text{Al}_2(\text{SO}_4)_3$, SiO_2 , Na_2SO_4 in ratio 2:1:8 (S_{12}) and $\text{Al}(\text{OH})_3$, SiO_2 , Na_2SO_4 in ratio 2:1:8 (S_{22}) [130]

It can be seen that at 646 °C the $\text{Al}_2(\text{SO}_4)_3$ began to melt followed by the Na_2SO_4 at 882 °C. In this flux the Al^{3+} ions dissociated then the mullite crystals formed from the coalescence of alumina ions on the silica sources, this process is shown graphically in Figure 31.

The reactions take place during this process are:

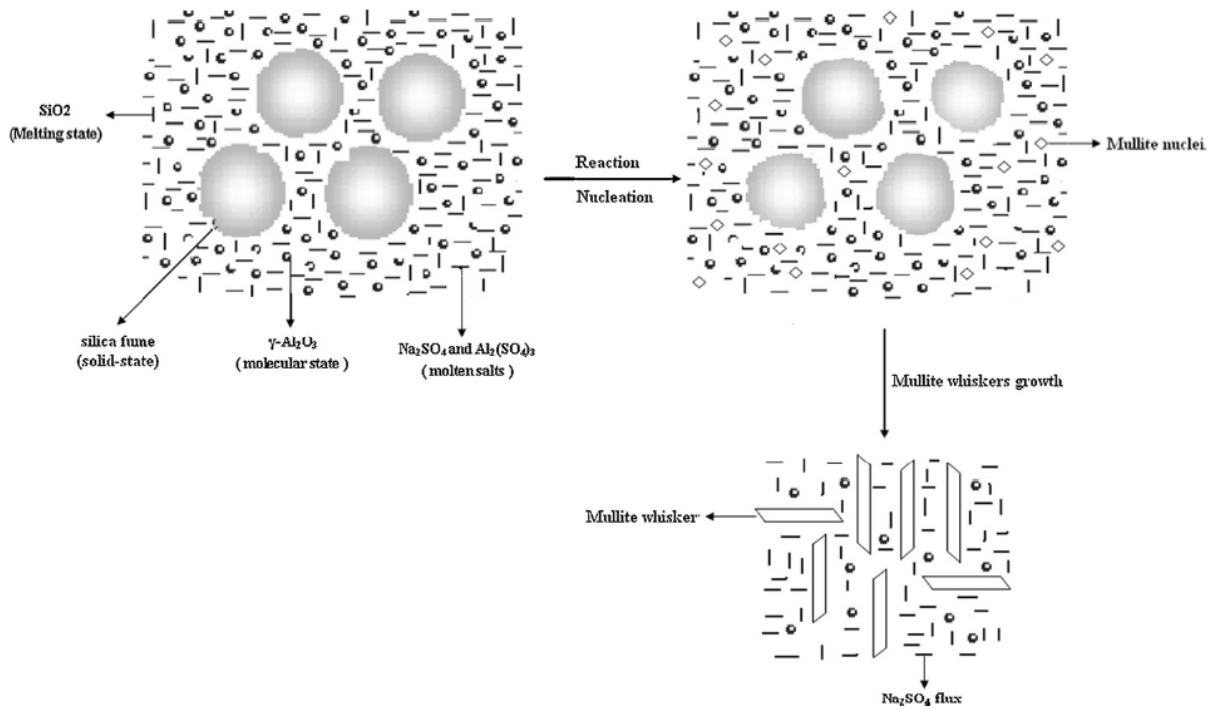
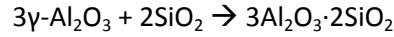


Figure 31: Formation of mullite whiskers through MSM [131]

2.4.3 Sintering

Sintering is the most common ceramic processing technique to convert a green body into a consolidated ceramic. The goal of the sintering process is to fuse individual powder particles together and remove pores from the microstructure. Sintering has been broken down into the initial stage, the intermediate stage and the final stage. In the initial stage sintering is dominated by neck growth between connected particles; this is the stage in which pores are formed and the ceramic transitions from a body of powder held together by a binder to a solid. The intermediate stage is defined by the formation of grains from

coalescing powders and a pore network made up of long interconnected pores. During this stage grains grow by shrinking the pore network, eventually cutting off the long continuous pores into smaller sealed individual pores. This stage usually yields sintered body with 70%-90% density. Sintering enters the final stage when the pore networks have collapsed and remaining porosity is made up of individual pores with an inherent pressure defined by equation (35). The only mechanism for pore elimination in this phase is vacancy diffusion which reduces the densification process. Provided crystal growth mechanisms are still activated during the final stage of sintering coarsening can become an issue, especially when a nano-crystalline ceramic is required. Some examples of whisker reinforced ceramic matrices are shown in Figures 32-34.

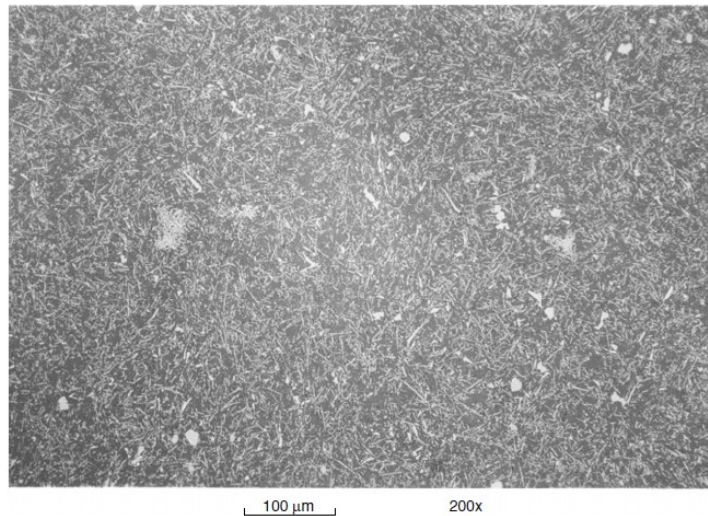


Figure 32: Alumina matrix reinforced with SiC whiskers with evidence of particulate contamination within the matrix [132]

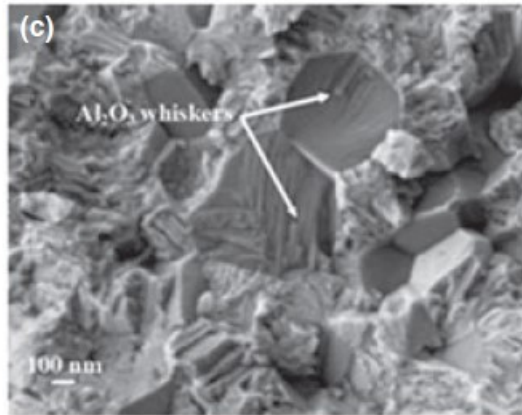


Figure 33: ATZ reinforced with alumina whiskers [133]

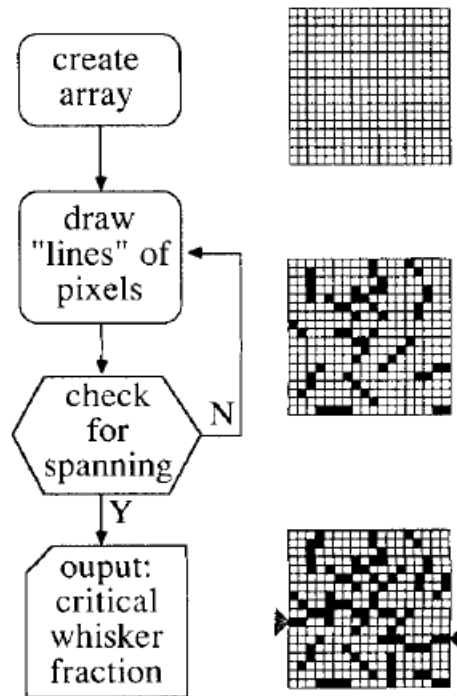


Figure 34: Graphical representation of a computer algorithm used to estimate the 2D packing factor of whiskers within a matrix [134]

In crystalline ceramic sintering there are six primary mass transport mechanisms of sintering which account for the coalescence, densification, and coarsening. These mechanisms are surface diffusion, lattice diffusion, vapor transport, boundary diffusion, lattice diffusion along grain boundaries and lattice

diffusion through dislocations. In general sintering mechanisms which move particles closer together and lead to densification are to be encouraged and mechanisms which grow the necks between particles leading to coarsening are to be avoided. Evaporation-condensation and surface diffusion are two mechanisms which lead to coarsening, evaporation-condensation occurs because the vapor pressure is lowered at necks with small negative curvatures. Equation (35) g expresses the change in vapor pressure due to negative curvature.

$$\Delta p = \frac{p_o \gamma V_m}{RT} \left(\frac{1}{\rho} \right) \quad (35)$$

Where Δp is the change in pressure, p_o is the vapor pressure of a flat surface, γ is the surface energy, V_m is the molar volume, R is the universal gas constant, T is the absolute temperature and ρ is the density. Equation (35) can be combined with the Langmuir equation for condensation to result in an equation for neck growth between particles (36)

$$\left(\frac{x}{r} \right)^3 = \left[\frac{3\sqrt{\pi}\gamma M^{3/2} p_o}{\sqrt{2} R^{3/2} T^{3/2} \rho^2} \right] t / r^2 \quad (36)$$

Where x is the distance between the centre of the two particles, r is the radius of curvature of the neck, M is the molar mass, and t is time. Equation (37) has been derived to describe neck growth by surface diffusions.

$$\left(\frac{x}{r} \right)^n = \left[\frac{J\zeta D_s V_m \gamma_{sv}}{RT r^4} \right] t \quad (37)$$

Where J is a numerical constant, ζ is the surface thickness, D_s is the surface diffusion coefficient and n will have a value between 5 and 7 depending upon neck shape.

Mechanisms of densification are driven by the stress gradient between the surface of the neck and the grain boundary plane. The mechanisms transporting matter from the grain boundary to the neck

include vacancy diffusion, grain boundary diffusion, lattice diffusion from the grain boundary and lattice diffusion from dislocations. Sintering will be dominated by the fastest mechanism of neck growth; the slowest species of the fastest mechanism will determine the rate of sintering.

In general, particle size will play an inverse power role in determining the rate of sintering as shown by equation (38)

$$\left(\frac{x}{r}\right)^n = \frac{C}{r^p} t \quad (38)$$

Where C is a constant, n has a value between 2 and 6, and p a value between 2 and 4. The exact values of n and p will depend upon the rate limiting mechanism. It can be seen that in general as the powder size is reduced the sintering time is also greatly reduced.

As can be seen by equation (38), creating a fully dense ceramic with minimal grain size through sintering is very challenging. This is especially true in ceramics where coarsening mechanisms activate and dominate at lower temperatures than densification mechanisms. This has led to several novel approaches to sintering. The most common approach is liquid phase sintering in which the powder is doped with another species which will liquefy at sintering temperatures. The liquid phase will assist accelerate mass transfer from grain boundaries to necks speeding up the densification of the ceramic. The dopant may also act to accelerate other densification mechanisms such as pore migration and grain boundary diffusion. This method is used extensively in heavily covalent ceramics such as SiC and Si₃N₄, which would not reach 100% density in a timely matter without a dopant. It has also been employed to densify alumina by doping with magnesia or zirconia species [19].

A second method is to apply pressure to the green body while sintering. This process is known as hot pressing and pressure can be applied either uniaxially or isostatically [135]. The increased pressure

supplements the capillary driving force at the contact area between particles [136]. The overall pressure at the contact point can be expressed by equation (39)

$$P \approx \frac{\gamma}{\rho} + \frac{P_a r}{\pi \rho} \quad (39)$$

Where P is the overall pressure and P_a is the applied pressure. The first term represents the pressure at the neck due to capillary forces and the second term is the additional pressure at the neck due to the applied pressure. An applied pressure of around 70 MPa will increase driving force of densification of a single phase system of 1 μm particles by 20 times. Furthermore applied pressure increases the driving force for densification without increasing the driving force for coarsening mechanisms [19].

A third technique is electric field assisted sintering (EFS) which is also called spark plasma sintering has been used to sinter ceramics to full density in very short time periods [137]. This technique compresses the sample between two graphite dies and pulses a strong DC current across them. This is a relatively new technique and is not fully understood. EFS is a promising method, however, the technique so far is only able to produce simple shapes and is therefore not suited to near net shaping production and will not be covered in depth in this thesis.

A final approach is to use several different thermal and pressure profiles throughout the sintering process. This method is often called two stage sintering and may take several forms. The most common form is to rapidly heat the sample to its regular sintering temperature and hold it there briefly before reducing the temperature to a lower level and soaking the sample for a while. The goal of this method is to complete the initial and secondary stages of sintering at the elevated temperature and then to bring the sample to a temperature at which final stage densification mechanisms will still be active but coarsening mechanisms will be reduced [138]. A second form of the two stage sintering soaks the sample at the lower temperature for a long period first and then brings the sample to the elevated

temperature for a shorter soak time to densify it. This technique relies on Ostwald ripening during the initial soak period to homogenize the particle sizes throughout the ceramic so that densification can proceed rapidly at the elevated temperature without flaws due to larger grains growing at a much greater rate than smaller ones [139]. A third two stage sintering technique is to soak the sample at an elevated temperature in a pressureless atmosphere until all the surface pores are sealed. The sample is then HIPed, with the goal being to accrue the benefits of HIPing without the difficulties of mold design and to allow near net shaped pieces to be HIPed [140].

The rate at which the ceramic sinters is of practical interest, because the amount of time required from sintering can be calculated from the rate. One method is known as the Master Sintering Curve (MSC) method, and the other relies on understanding the activities of the species at the sintering temperature. In the MSC method, the linear shrinkage rate of the powder compact is related to material and thermodynamic properties through equation (40)

$$-\frac{dL}{Ldt} = \frac{\gamma\Omega}{kT} \left(\frac{\Gamma_v D_v}{G^3} + \frac{\Gamma_{bo} \zeta D_{bo}}{G^4} \right) \quad (40)$$

Where γ is the surface energy, Ω is the atomic volume, k is the Boltzmann constant, T is the absolute temperature, G is the mean grain size, t is the time, L is the sample length, D_v and D_{bo} are the coefficients of volume and grain boundary diffusion, ζ is the thickness of the grain boundary, and Γ_v and Γ_{bo} are scaling parameters which are related to geometric features. In MSC methodology, equation (39) can be simplified by assuming that one sintering mechanism dominates, either grain boundary or volume diffusion, and that the microstructure will evolve based solely on density. After some manipulation the simplified equation is presented as equation (41)

$$\frac{k}{\gamma\Omega\zeta D_o} \int_{\rho_0}^{\rho} \frac{(G(\rho))^n}{3\rho\Gamma(\rho)} d\rho = \int_0^t \frac{1}{T} \exp\left(-\frac{Q}{RT}\right) dt \quad (41)$$

Where Q is the activation energy of the sintering process, D_0 is the diffusion constant, ρ is the density of the sample and n takes the value of 3 for volume diffusion and 4 for grain boundary diffusion. To determine the master sintering curve, several different samples of the same powder are heated at different rates while undergoing dilatometric measuring. The density of the ceramic under various heating profiles is matched against the right hand of equation (41). An example of a master sintering curve is given in Figure 35.

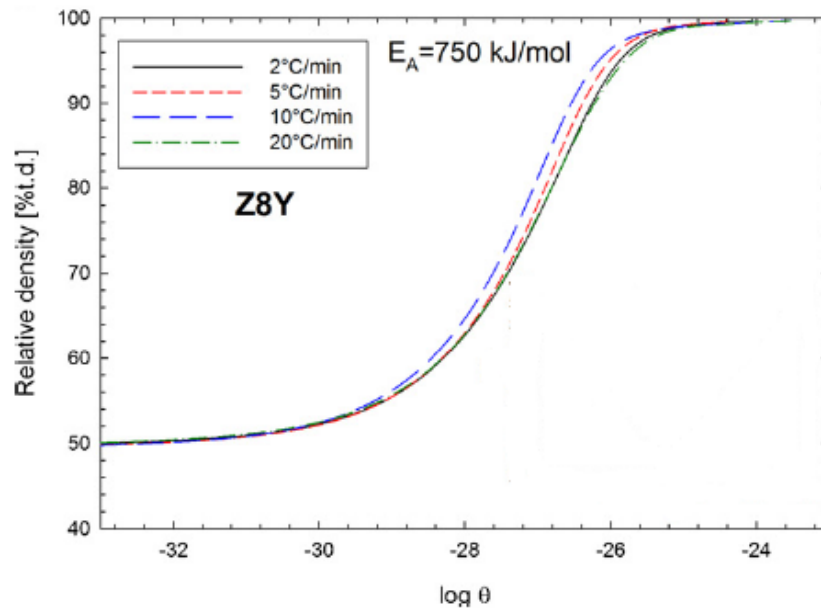


Figure 35: Master sintering curve of 8% Ytria partially stabilized ZrO_2

The MSC method can be used to predict activation energy for the primary sintering mechanism as well as predict the time required to reach full density.

An empirical examination of sintering has shown that in simple systems porosity can be related to grain growth through the expression given in equation (42)

$$G = \theta G_0 / \psi^{1/2} \quad (42)$$

In this equation G is final grain size, θ is a constant having the value of 0.6 for simple systems with spherical uniform grains, G_0 is the initial grain size and ψ is the porosity. A second formula for the rate of grain growth can be combined with equation (42) to calculate the sintering time required [141].

Densification can also be expressed in terms of Q , the lowest activation energy for the different diffusion mechanisms, T , absolute temperature, d and n , grain size and a constant which is 3 if the diffusion mechanism is lattice controlled and 4 if it is grain boundary controlled and $f(\rho)$, a function based on the density.

$$\dot{\rho} = A \frac{\exp(-Q/RT) f(\rho)}{T d^n} \quad (43)$$

$$A = \frac{C\gamma V^{2/3}}{R} \quad (44)$$

In equation (43) expressing A , C is a constant, γ is surface energy, and V is molar volume. This equation is useful in comparing densification rates between different mechanisms with different activation energies. It can also show the effect of grain size upon densification. It should be noted, however, that grain size may change during densification, and this must be accounted for. Wang and Raj completed a study to determine the effect of ZrO_2 content on the activation energy for sintering of ZTA. Within this study it was determined that activation energy for sintering will be relatively unchanged at ZrO_2 vol% of between 5% and 95%, and will be larger at those volume fractions than for either pure Al_2O_3 or ZrO_2 . They also examined the effect of 2.8% yttria in the ZrO_2 and found it did little to effect the activation energies [142].

Whiskers present an addition boundary to the formation of fully dense ZTA_w due to their interaction with sinter mechanics. It has been shown that above a certain volume fractions, hard inclusions within a ceramic matrix may form an inflexible network greatly reducing grain boundary mobility and trapping

pores within the matrix [143]. Holm and Cima have created a model to study the percolation of a whisker network in 2D; this model shows the dependence upon aspect ratio and volume fraction and sets the limit at 27% volume fraction with an aspect ratio of 7 [134]. This model agrees with experimental work which limits the whisker volume fraction at just below 20% [100].

3. 0 Summary and Thesis Objectives

The introduction has outlined the need for new, higher temperature structural materials for the next generation of gas turbines. CMCs have been identified as likely candidates to replace superalloys, and the advantages, disadvantages and mechanical properties of many ceramic, and CMC systems has been reported. A discontinuously reinforced oxide/oxide CMC was selected for this study as a starting point for research into CMCs at Carleton and the NRC.

As covered in the literature review, SiC whiskers have improved the toughness, strength, and creep resistance of oxide matrices. At temperatures above 1100°C there is evidence that SiC whiskers oxidize creating glassy phases and voids which annul the improvements seen at room temperature. This study investigates the use of mullite whiskers as a reinforcement stage. Mullite whiskers were selected both for their high temperature stability and the recently reported low temperature production technique using a molten salt bath. Zirconia toughened alumina was selected for the matrix due to improved mechanical properties over single oxide phase matrices and high temperature stability. There has been no reported mullite whisker enhanced zirconia toughened alumina composites in the literature.

Colloidal fabrication was chosen as the production method of choice due to control over interparticle forces and adaptability to near net shape forming techniques. The microstructures of produced composites are examined to evaluate the colloidal production method selected. Mechanical properties and high temperature stability are investigated including flexural strength at room temperature and 1200°C, fracture toughness and hardness at room temperature, and phase stability during thermal cycling between room temperature and 1200°C.

The objective of this research is to examine the possibility of using mullite whiskers as a stable high temperature reinforcement of zirconia toughened alumina. This research will examine production methods to determine a production route which will result in excellent mechanical properties and low

porosity. The research will measure: room temperature strength, room temperature fracture toughness and room temperature hardness and compare these results to various ceramic materials currently available. It will also measure flexural strength at 1200 °C and thermal stability during thermal cycling from room temperature to 1200 °C. These properties will be measured to examine the stability and suitability of mullite reinforcement in oxide/oxide discontinuous ceramic matrix composites for high temperature applications.

4.0 Materials and Experimental Procedures

The general production route for ZTA_w has been guided by published work covered in the literature review. This chapter will outline the powder selection, modified processing and sintering techniques and various methods used to characterize the composite and its properties.

4.1 Materials Selection

Commercial powder was selected as the raw material for the ZTA matrix. The powder route was selected based on its simplicity and the ability to include the whisker phase. The alumina powder used was ALO-101 from Praxair Canada (99.0% purity, 325 mesh). The zirconia powder used was ZRO-271-3 from Praxair Canada (7.5 wt % Y₂O₃, Bal. ZrO₂, 325 mesh). The chemicals used in the molten salt method (MSM) to grow the mullite whiskers were sourced from Sigma-Aldrich Canada. Alumina ions within the salt were provided by Al₂(SO₄)₃·16H₂O. Silica Fume (amorphous SiO₂, D₅₀ of 0.2-0.3 μm) provided the silica ions; the amorphous nature of the silica fume ensures that the silica was able to dissolve within the salt bath more readily. The D₅₀ measurement given for the silica fume is the log-normal distribution mass median diameter of the silica particles. The molten flux was created by melting sodium sulfate (Na₂SO₄) anhydrous from Fisher Scientific. For the colloidal slurry, the polysaccharide adlayer was produced by Dextrin (derived from corn) from Sigma-Aldrich Canada. The pH of the slurry was adjusted using 0.1M HCl acid from Fisher Scientific. The binder used during compaction was created with polyvinyl alcohol pellets from Sigma Aldrich Canada.

4.2 Molten Salt Method (MSM) Whisker Growth

Section 2.4.2 of the literature review covers the theory behind the molten salt method used to grow the mullite whiskers. A mixture of SiO₂, Al₂(SO₄)₃·16H₂O, and Na₂SO₄ with a weight ratio of 1:8.5:9.5 was placed within a Fritsch Pulverisette 6 eccentric motion ball mill and milled at 200 rpm for 3 h (the grinding media was 5mm ZrO₂ balls in a ball to mixture weight ratio of 15:1 ; the container was

hardened steel.) The milling was done to ensure thorough mixing of the MSM precursors so that the melting reaction occurs uniformly. After milling, the mixture is placed in an alumina crucible with a covering and heated in the Sentro Tech Corp STT-1600C-4-12 High Temperature Tube Furnace. The heating profile of the MSM mixture is shown in Figure 36.

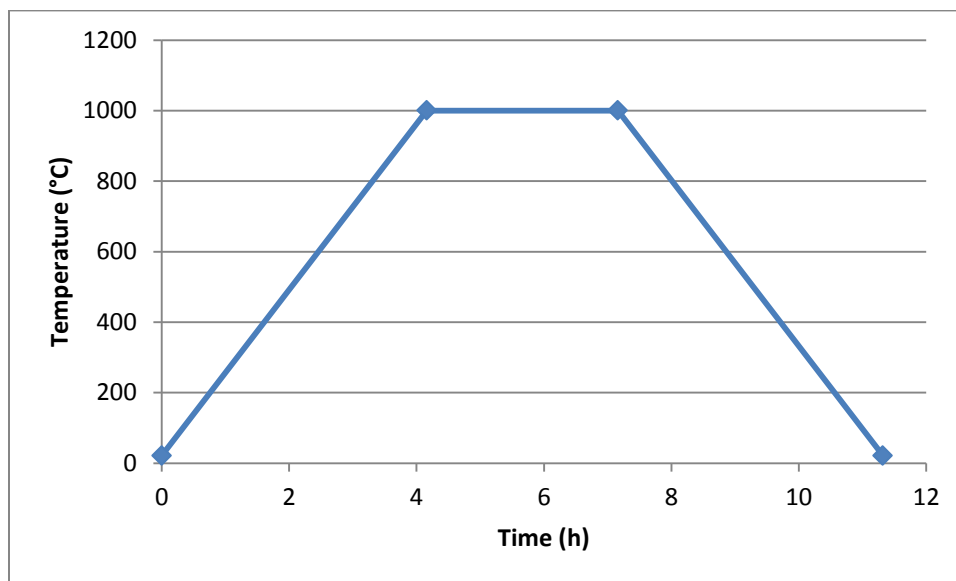


Figure 36: Heating profile for MSM

The ramp up time was determined based on the thermal shock coefficient of the alumina tube and crucible. The hold time was determined by examining the results of TGA reported by Zhang et al. [129]. The whiskers were recovered by soaking the heat treated mixture in distilled water held at 99 °C. The distilled water dissolves the Na_2SO_4 produced and was filtered away from the whiskers through pressurized filtration system with a 0.1 μm pore filter.



Figure 37: Filter system used to remove liquid slurry and salt solution. As water runs through the aspirator on the right a vacuum is formed within the beacon to assist with filtering

The remaining whiskers were placed in another distilled water solution and ultrasonically processed for 30 min to separate individual whiskers which were separated through sedimentation then further filtered.



Figure 38: Batch of filtered whiskers before ultrasonic treatment

4.3 Slurry Preparation and Consolidation

To reduce the powder size to a nanometer range a Fritsch Pulverisette 6 high energy ball milling process was employed. It has been shown that the most effective method of high energy ball milling is a dry powder process with an eccentric milling pattern [126]. A mixture of alumina and zirconia (85:15 weight ratio) powders was placed within the ball mill and milled for 8 h at 200 rpm (milling media is 5mm zirconia balls, 15:1 weight ratio of milling media to mixture). The milled powder was recovered through a sieving process and a slurry is prepared with the milled power. Dextrin was required to form an adlayer on the ZTA particles, increasing both steric repulsion and charging of individual particles within an acidic solution. The dextrin was dissolved in the distilled water in a weight ratio of 5:95, dextrin to ZTA powder. Once the dextrin was dissolved the ZTA powder was added, the distilled water is topped up to ensure that total solids content does not make up more than 30% of the volume of the solution. The volume of ZTA powder was calculated using theoretical density of 85ZTA. For the ZTA_w the mullite whiskers were added in a quantity such that they formed a volume fraction of 20% of the final

composite. The pH of the slurry was adjusted to 2.0 using HCl acid and the slurry was stirred vigorously using a magnetic stirrer for 3 h. The liquid was then filtered off with the same pressure filtration system shown in Figure 37. After filtering, the powder was dried at 120°C for 4 h and then at room temperature for 24 hours. The dried powder was combined with a 3% PVA solution at a PVA to ZTA ratio of 5:95 (in weight) using the Pulverisette 6 ball mill without a milling media at 350 rpm for 20 min. The final powder mixture was placed within hardened steel mold and pressed at 175 MPa for 10 min before sintering.



Figure 39: Pressed green compact prior to sintering with diameter of 76.2 mm

Table 9: Sample Compositions

Sample	Alumina (wt. %)	Zirconia (wt. %)	Mullite (wt. %)
ZTA _n	85	15	0
ZTA _w	71.6	12.7	15.6

4.4 Sintering

The sintering temperature profile must be controlled to ensure complete binder burn out and consolidation to near theoretical density for ZTA_n and to at least 92% theoretical density for ZTA_w.

The two organic agents used during processing are Dextrin and PVA. It has been shown that these organics will volatilize and burn out of the matrix at temperatures above 450°C [144]. When selecting the temperature profile for binder burnout the ramp time must be controlled to ensure volatilization is not too rapid, creating pores with high pressure gas and undermining the integrity of the green compact [124]. The atmosphere must also be taken into account; if there is insufficient free oxygen a carbon based residue will form within the sintered ceramic which will reduce the desired properties [145] [146]. The original sinter profile used to fire the samples is given in Figure 40a, this firing was undertaken in an argon atmosphere at standard atmospheric pressure using CFV900 Turbo vacuum furnace from Oxygen Industries. Earlier samples fired in an argon atmosphere showed signs of carbon residue (from pyrolysis) as evidenced by Figure 40b.

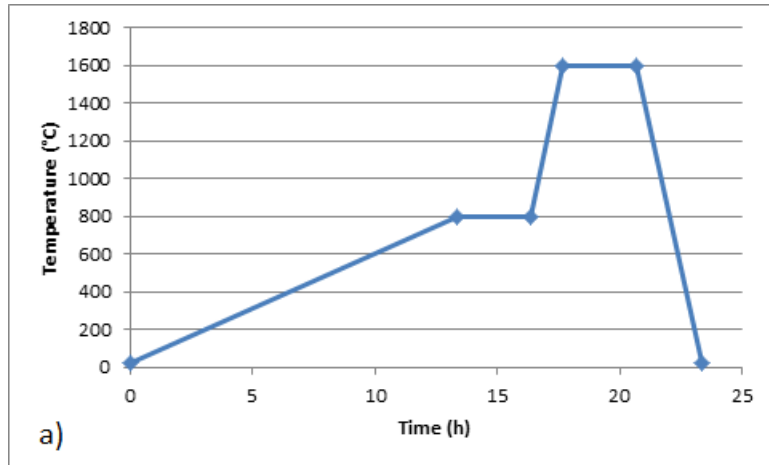


Figure 40: (a) Original sinter profile for ZTA_n and ZTA_w (b) ZTA_n sample after sinter profile 1, with black carbon residue patches

The ramp up and final soak temperature are dependent upon the microstructure and chemical properties of the green compact as shown in section 2.4.3. A final temperature of 1600°C and a soak time of 4h did not produce the desired results, therefore the procedure was adjusted to include a slow ramped burn-out phase in a standard atmosphere furnace followed by a slow ramp to 1600°C in the CFV900 Turbo vacuum furnace and a dwell time of 20 hours with a controlled cool down. To prevent damage to the green compact during burnout a ramp up rate of 1°C/min was used to a burn out temperature of 800°C, with a cool down rate of 4°C/min. The ramp rate of the vacuum furnace was 4

°C/min up to 1600 °C and the cool down rate was 10 °C/min; these ramp rates also ensures that smaller thermal gradients appear within the sample which reduces undesirable warping within the sample [147]. The dwell temperature was selected based upon previous literature sintering profiles and the dwell time was selected to ensure a greater density.

The final sintering profile is shown in Figure 41.

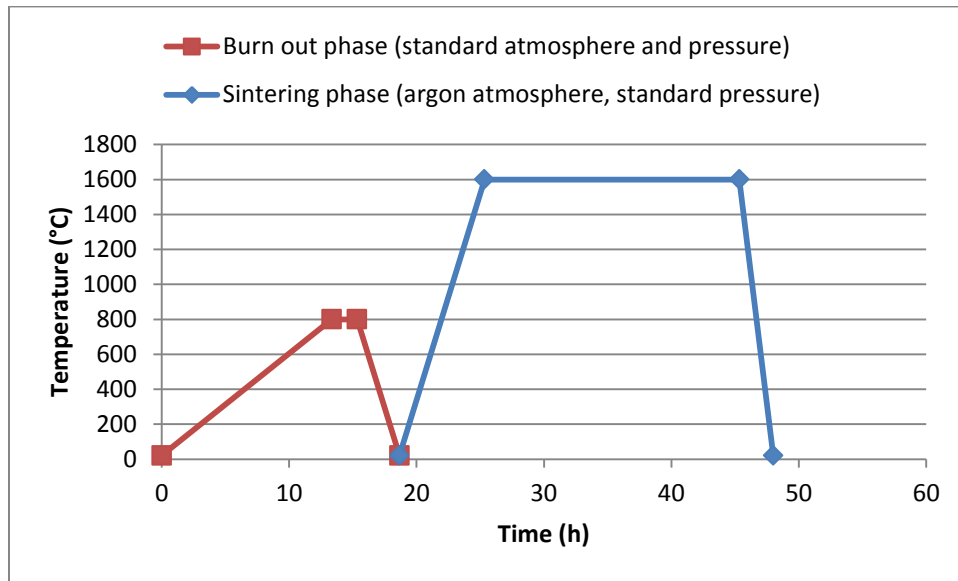


Figure 41: Final sinter profile for ZTA_n and ZTA_w

A programmable STT-1500-4-12 High Temperature Furnace operating under a standard atmosphere was used for the burn out phase and the CFV900 Turbo vacuum furnace from Oxygon Industries was used for the sinter phase.

The secondary sintering phase of ZTA_w takes place within a HIP press. A pressure of 480 MPa and a sintering temperature of 1600 °C for 2 h was used. As covered in section 2.4.3 the increased pressure of the HIP press allows the composite to reach near theoretical density without increased grain growth.

4.5 Characterization

The microstructure and the mechanical properties of the produced samples have been characterized. The microstructure has been examined to ensure that the processing steps produced the composite as desired.

4.5.1 Powder Characterization

Powder characterization is undertaken before and after the milling process. The median size and size distributions of the alumina and zirconia constituents are of primary interest. The degree of mixing and the presence of soft agglomerates of whiskers, ZrO_2 or Al_2O_3 particles after milling are also important aspects for process development.

ASTM standard E2651-10 specifies proper powder particle size analysis techniques. The technique selected for this research was static image analysis. A sample of powder was gathered on carbon tape and coated with 0.18 nm gold (using an Anatech LTD Hummer VII sputtering machine) since the powder is non-conductive. A Tescan Vega-II XMU SEM at 20.00 kV (with a tungsten filament) was used to capture the images. To determine zirconia particle size the quantitative image processing program ImageJ2 was used [148]. The SEM images were appropriately scaled and then converted into a black and white image for the particle analysis program, an example of an image after conversion is given in Figure 42.

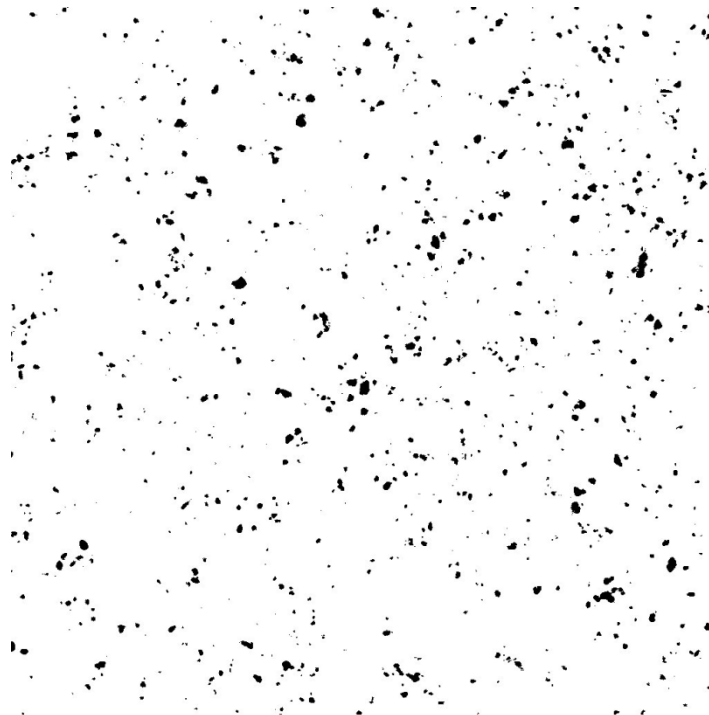
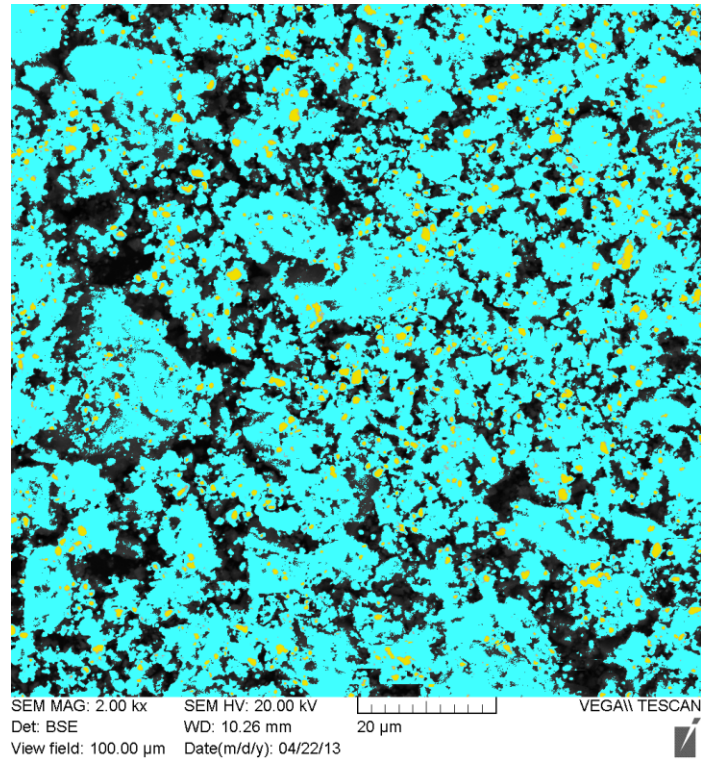


Figure 42: ZTA powder color distribution and conversion to black and white for ZrO_2 particle size analysis

The outlines of the particles counted are shown in Figure 43.

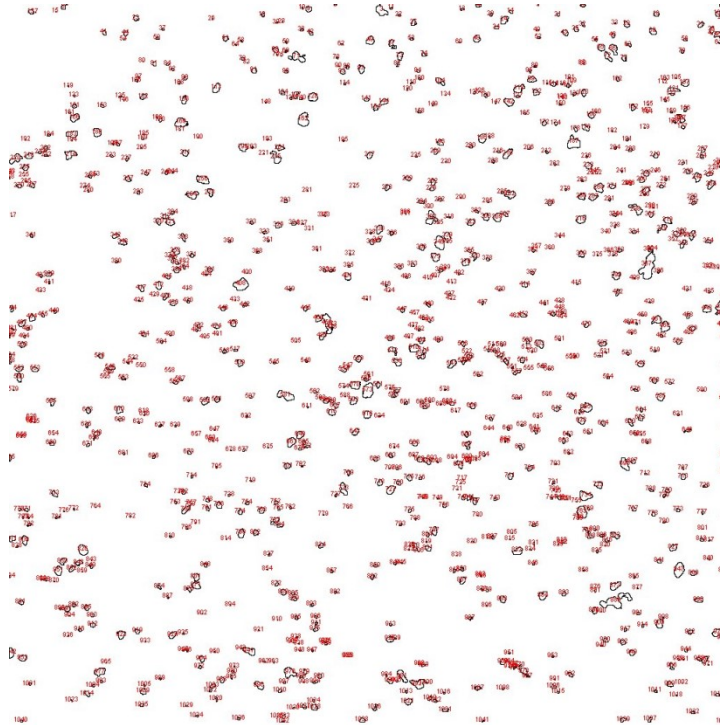


Figure 43: Outlines of particles counted for particle size analysis

The size distributions were then exported into Microsoft Excel and examined on a cumulative diameter basis with the same method being used to measure zirconia grain size as well. The ImageJ2 particle analyser could not be used to measure alumina particles and grain sizes because the grey scale gradient of each alumina particle was too difficult to mask to a black and white scale accurately, and the particles were overlapping too much to use a color distribution. To measure grain sizes and particles an automated line intercept method was adapted using ImageJ2 again. An ImageJ2 line plot was used to detect grain boundaries and where each particle begins or ends based on the level of grey scale. An example of a line plot is shown in Figures 44a and 44b.

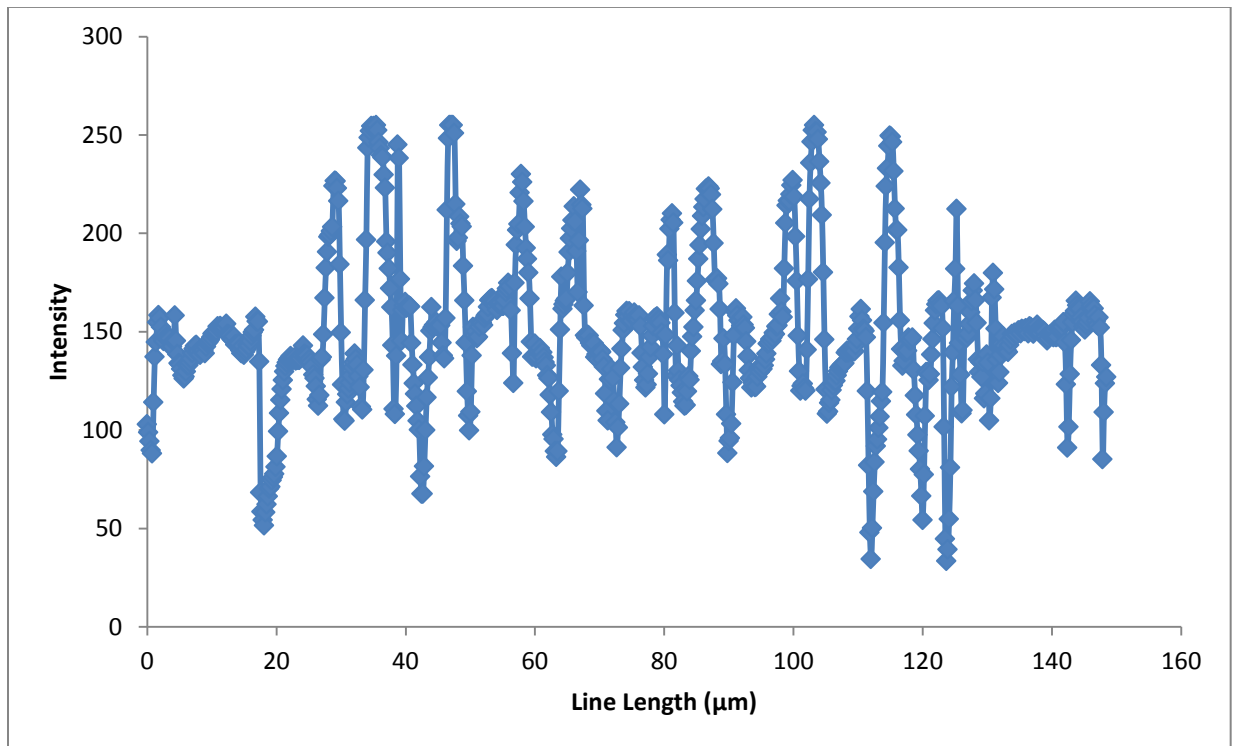
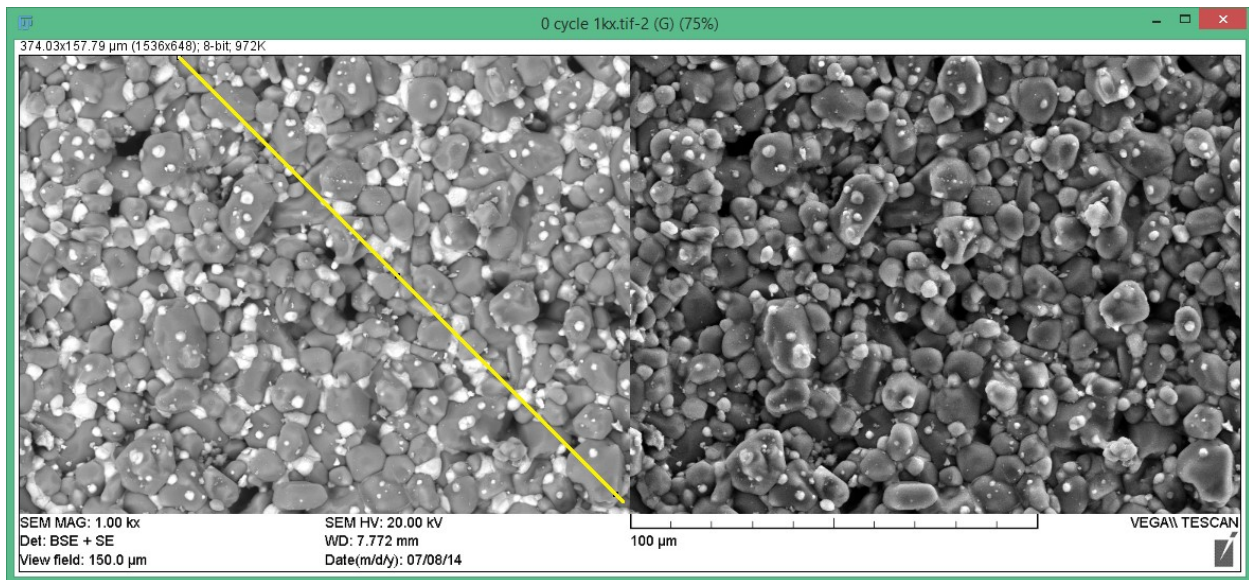


Figure 44: a) line drawn on SEM image of ZTA and b) corresponding line plot of shading intensity where valleys occur at grain boundaries and peaks at zirconia grains

Sharp changes in the grey scale presented on the line plot indicate grain boundaries. An excel algorithm was used to detect changes in grains and return grain sizes for each sample.

4.5.2 Microstructure of Sintered Samples

The microstructure of post sintered samples is examined using a Tescan Vega-II XMU SEM and a Bruker D8 Advance X-ray diffractometer. Features of interest include grain size and distribution of the phases; the size, occurrence, and type of pores present within the microstructure; the chemical composition of each phase; and the crystal structure of the phases.

4.5.2.1 Scanning Electron Microscopy

Post sintered samples were polished with SiC sand paper with grit sizes 180, 240, 400, 600 before a final polishing using a 6 μm diamond suspension. To create a greater contrast between the grain boundaries and grains the samples were thermally etched in an ambient atmosphere at 1200°C for 2 hours [149]. To conduct electricity samples were coated with 9 nm of Au. Energy dispersive x-ray spectrometer (EDS) was utilized to examine the chemical compositions in bulk samples as well as each phase. The EDS was able to determine the elements present but was unable to determine the weight percentage of each composition due to the conductive coating, the electron build up on the surface of the sample, and the limited electron spot size. The grain size was determined using the methods covered in section 4.1

4.5.2.2 X-ray Diffraction

XRD was used to examine the crystal structure of the phases of pre-sintered ZTA_w and ZTA_n powder, sintered ZTA_n, HIPed ZTA_w and post-thermal cycled samples. It is important to know how the sintering affects the crystal structure of the composite. It is also important to determine the effect of the thermal cycling on the crystal structure. As mentioned in section 2.2.3 and 2.2.6, diffusion of oxygen from atmosphere to the samples can alter the phases and potentially reduce the properties of the ceramic.

The XRD was carried out with a Bruker D8 Advance X-ray diffractometer, which is operated at an accelerating voltage of 40 kV and a current of 40 mA using Co K α radiation in the 3 θ range of 25 - 100°.

4.5.2.3 Porosity

The ability for a sample to HIP properly depends on the nature of porosity in the sample. If pore networks within the sample are still exposed at the surface then HIPing will have little effect on the density of the composite. Remaining pores within the microstructure will also act as stress concentrators and lead to early failure of the sample, reducing the strength and fracture toughness. Porosities of the post sintered and post-HIPed samples were determined using Archimedes principle in distilled water. The weight of dry samples was measured, the samples were then immersed in distilled water and the weight of the samples was measured again. Finally, samples were removed from the water and their wet weight was measured. Equations (45) through (47) were used to determine the density, %theoretical density and the exposed and interconnect pore content.

$$\rho = \frac{(A \cdot B)}{(A - F)} \quad (45)$$

$$\% \rho = \frac{\rho}{\rho_{th}} \quad (46)$$

$$AP = \frac{(C - A)}{(C - F)} \quad (47)$$

Where ρ is the density, $\% \rho$ is the %theoretical density, ρ_{th} is the theoretical density, A is the mass of the specimen in air, B is the density of the distilled water, F is the mass of the specimen in water with the support mass tarred, AP is the open and interconnected pore content, and C is the mass of the specimen saturated with water.

4.6 Room Temperature Testing

The two mechanical properties of greatest interest at room temperature are flexural strength and fracture toughness.

4.6.1 Strength

A three point bending fixture was used to determine the flexural strength of the composite. ZTA_n and ZTA_w bars of 45 mm (length) x 3 mm (thickness) x 4 mm (width) were produced by diamond blade sectioning of sintered disks. Surface defects can have a large effect on the measured strength due to their ability to concentrate stress. To reduce the likelihood of surface defects samples were polished using the same polishing schedule outlined in section 4.2.1. These samples were then placed within a 3 point bending frame with a span of 20 mm and bearing diameter of 3.5 mm.

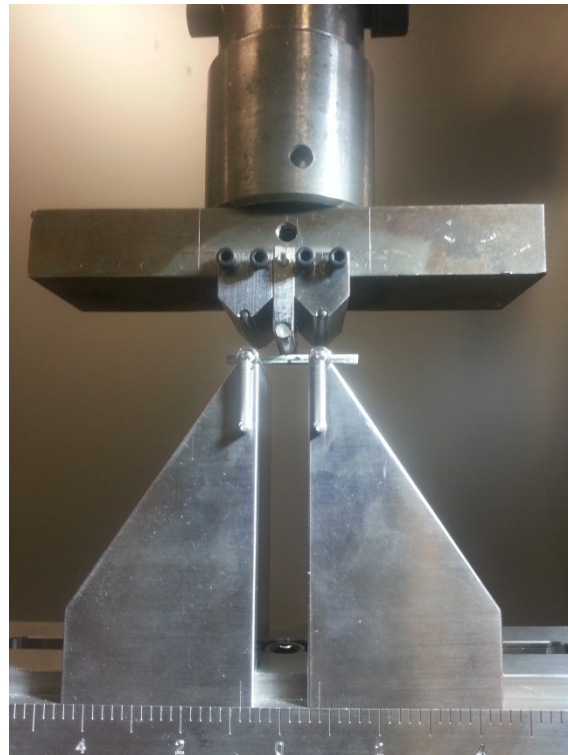


Figure 45: 3-point bending rig for room temperature flexural testing

The bending test was set up on an MTS test frame, controlled with Testware software. A maximum displacement rate of 0.5 mm/min was set and the corresponding force vs. displacement was plotted.

The fracture strength was calculated using formula (48) and the elastic modulus of the sample was calculated using equation (49).

$$\sigma = \frac{3 PL}{2 w z^2} \quad (48)$$

$$E = \frac{L^3 s}{4 w z^3} \quad (49)$$

Where σ is the maximum stress within the sample, P is the force measured when the sample fractures, L is the span, w is the width, z is the thickness of the sample, E is the elastic modulus and s is the slope of the linear portion of the force/displacement plot generated from the test.

4.6.2 Fracture Toughness

A modified indentation test was used to determine the fracture toughness of the samples. This technique, developed by Palmqvist in 1957 and later refined by Ponton and Rawlings [150] [151] [152], estimates the fracture toughness by examining micro cracks caused by a micro indenter. The size of the crack can be correlated to the material's hardness and elastic modulus and a value for the resistance to crack growth can be determined.

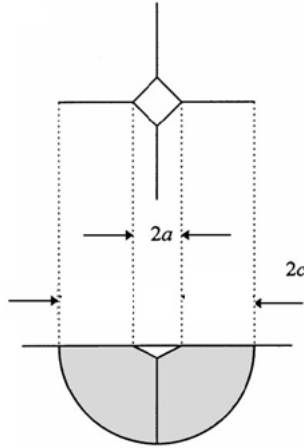


Figure 46: Theoretical crack shape caused by a micro indentation [153]

This method depends upon the assumptions that the plastic zone in relation to the crack size is very small, and that the crack shape is half –penny. Gong has further adapted the process, incorporating true hardness into the fracture toughness equation for a closer fit to results from notched bending tests [153].

$$P = \varphi_0 + \varphi_1(2a) + \varphi_2(2a)^2 \quad (50)$$

$$H = (1.8544)\varphi_2 \quad (51)$$

$$K = 0.046(EH)^{1/2} \left(\frac{a^2}{c^{3/2}} \right) \quad (52)$$

Where P is the force used to indent the specimen, φ_i terms are curve fitting coefficients, H is the calculated hardness, K is the fracture toughness, E is the elastic modulus, a is the half width of the imprint left by the micro-indenter and c is half the length of the crack created by the indenter. Where E was determined through the three-point bending test from section 4.2.1.

4.7 High Temperature Testing

The high temperature mechanical properties of particular interest flexural strength and creep resistance. High temperature fatigue is another property of interest; however, characterizing the fatigue is beyond the scope of the current thesis. Creep characterization was also delayed due to force control issues caused by the load cell. The temperature range of 1200 °C for measuring high temperature properties was selected as a benchmark temperature above the current 1100 °C limit of oxide based porous CMCs.

4.7.1 Strength

The determination of high temperature strength follows a similar procedure as the determination of room temperature strength. ASTM standard 1211-02 stipulates that the temperature must be held at the desired temperature within $\pm 2^\circ\text{C}$ for the duration of the strength test. A customized Applied Test Systems rig was used to determine the material's strength at 1200°C. Type B-thermocouples were used to control the temperature within the furnace which has a range up to 1700°C while a type S-thermocouple was used to report the test temperature. Silicon carbide bending fixtures were supplied to comply with the at-temperature strength and hardness specifications of ASTM C1211 – 02. The span was 40 mm, with bearing diameter of 3.5 mm. An MTS test frame supported the set-up with hydraulically controlled armatures to supply the force. Figure 47 shows the high temperature bend test equipment.

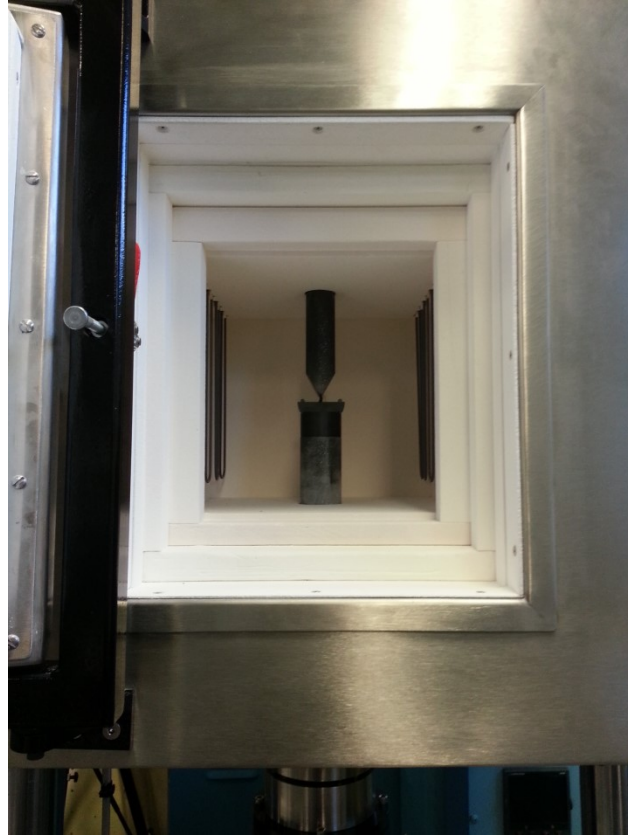


Figure 47: High temperature 3-point bending fixture and surrounding furnace

4.8 Cyclic Testing

The sample is subjected to cyclic thermal loading condition to test the thermal stability of the phases as well as thermal fatigue lifecycle of the sample. 12 polished samples of ZTA_w were placed in a CM Inc. Rapid Temp Furnace and cycled using to profile of a 10min ramp up to 1200°C, soak for 40 min then fan cooling to room temperature for 45 min. The samples were visually inspected after every cycle for the first 5 cycles, and then at specified cycle intervals until 450 cycles were reached. Any cracks or other features of note were inspected under the SEM for a closer analysis.

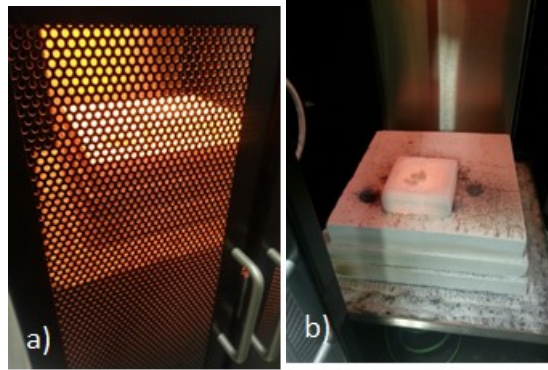


Figure 48: Cyclic thermal test equipment a) samples cycling from the furnace, heat shield intact b) heat shield open showing samples on porous alumina slab

Samples were examined for change in mass after cycles 1, 2, 3, 4, 10, 50, 100, 250, 300, 350, 400 and 450 cycles. XRD scans were taken of a sample after 250 and 450 cycles. The measurement of the change in mass was used as a quick test to examine if any oxidation or volatilization has occurred. XRD was used to determine the evolution of the crystalline phases, further SEM analysis was conducted to support the XRD results.

5.0 Results and Discussion

The characteristics of the ground powder, the effectiveness of the production route and the desired mechanical properties have been measured and will be presented in this section. A brief discussion of the results obtained will also be presented here.

5.1 Powder Characterization

A mixture of 85 wt % alumina powder and 15 wt% stabilized zirconia were mixed by dry ball milling for 8 hours. Figure 49 shows the mixture of the powders prior to milling. And Figures 50-54 show the powder mixture after 1 h, 2 h, and 8 h of dry milling at 200 rpm.

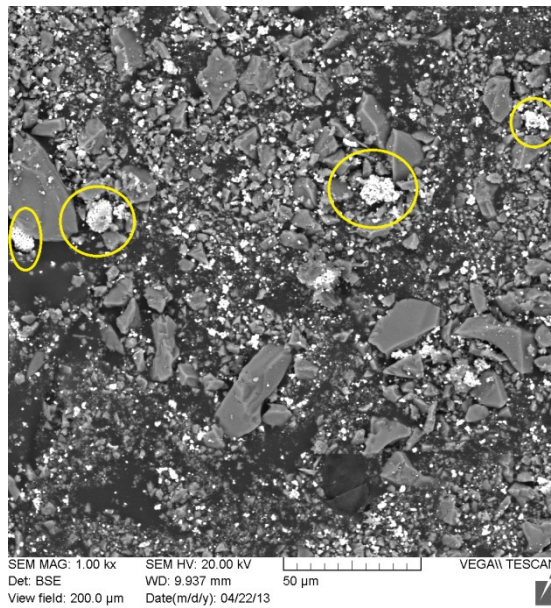


Figure 49: 85 wt.% Al_2O_3 powder and 15 wt.% ZrO_2 powder prior to ball milling. Zirconia agglomerates are circled in yellow

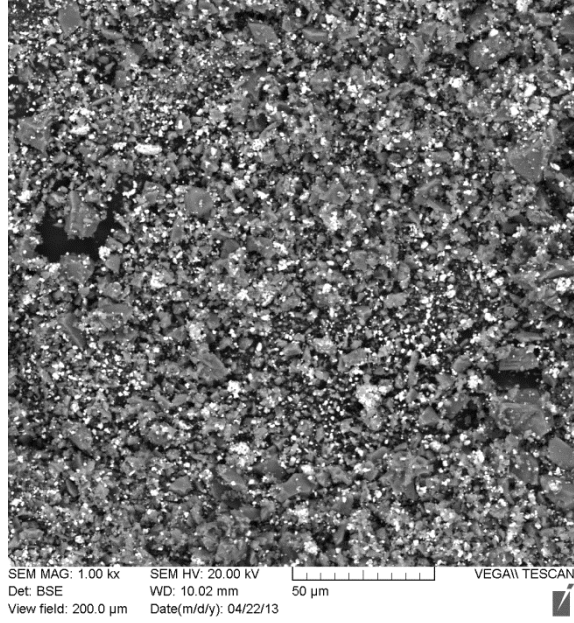


Figure 50: 85 wt% Al₂O₃ powder and 15 wt% ZrO₂ powder after 1 hour of ball milling

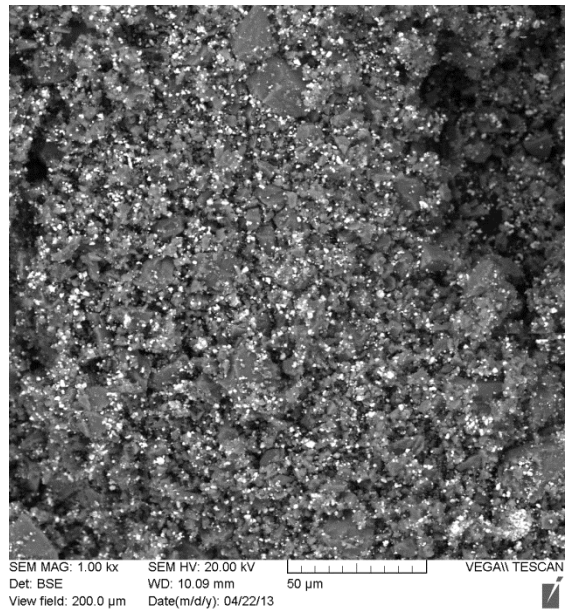


Figure 51: 85 wt% Al₂O₃ powder and 15 wt% ZrO₂ powder after 2 hours of ball milling

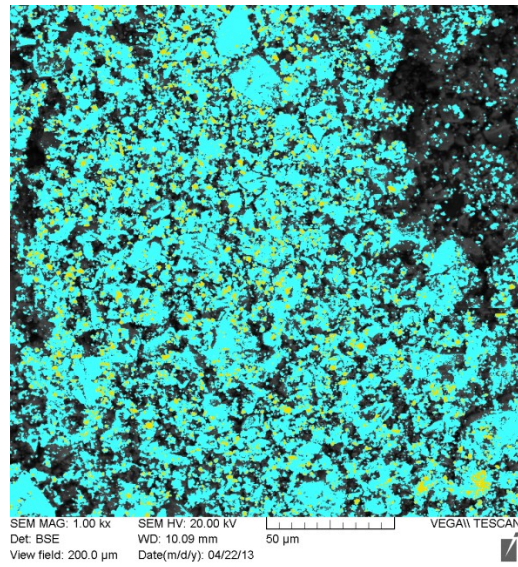


Figure 52: 85 wt.% Al_2O_3 powder and 15 wt.% ZrO_2 powder after 2 hours of ball milling shown with a color distribution to highlight the two phases (blue=alumina and yellow=zirconia black/grey=background)

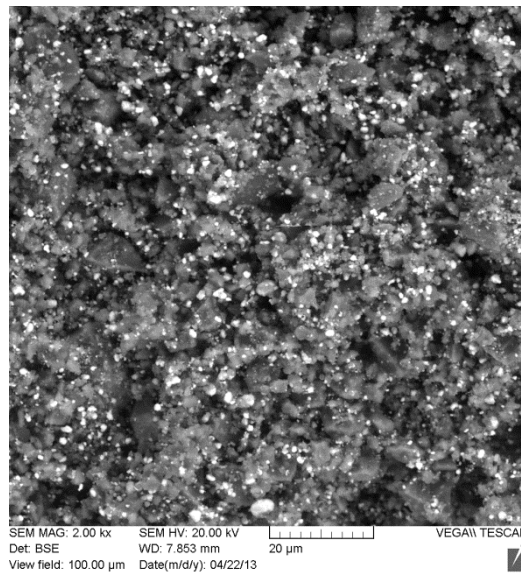


Figure 53: 85 wt.% Al_2O_3 powder and 15 wt.% ZrO_2 powder after 8 hours of ball milling

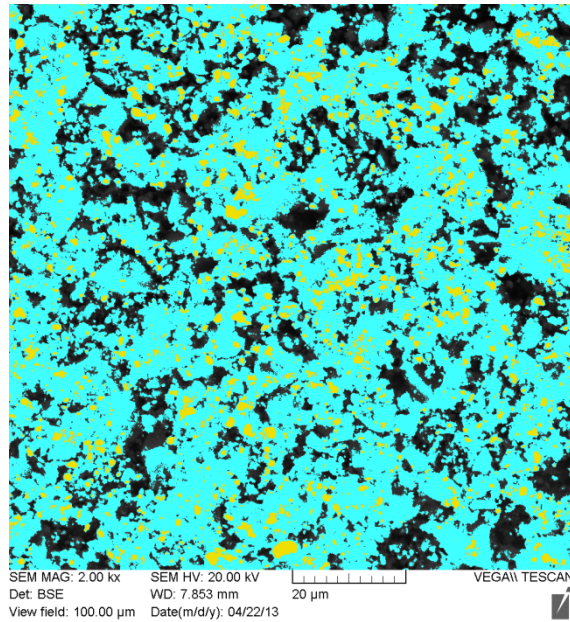


Figure 54: 85 wt.% Al₂O₃ powder and 15 wt.% ZrO₂ powder after 8 hours of ball milling shown with a color distribution to highlight the two phases (blue =alumina, yellow=zirconia, black=background)

It can be seen from the images that the pre-milled powder contains agglomerations and is hardly mixed. After 2 h of milling reduction of powder size undergoes diminishing returns. Figures 52 and 54 use a coloration program to highlight the level of mixing of the two powders. The teal colour exhibits the alumina phase while the yellow shows the zirconia phase. The average particle sizes of the alumina and zirconia powders as a function of ball milling time are summarized in Table 10. The cumulative distribution vs. size of alumina and zirconia particles for the 6 different milling times have been plotted in Figures 55 and 56.

Table 10: Average particle sizes after 8 h of dry ball milling

Time in Mill (h)	Al ₂ O ₃ Average Particle Size (μm)	ZrO ₂ Average Particle Size (μm)
0.25	4.33	1.41
0.5	5.01	1.98
1	3.99	0.93
2	4.37	0.65
4	2.47	0.25
8	2.97	0.23

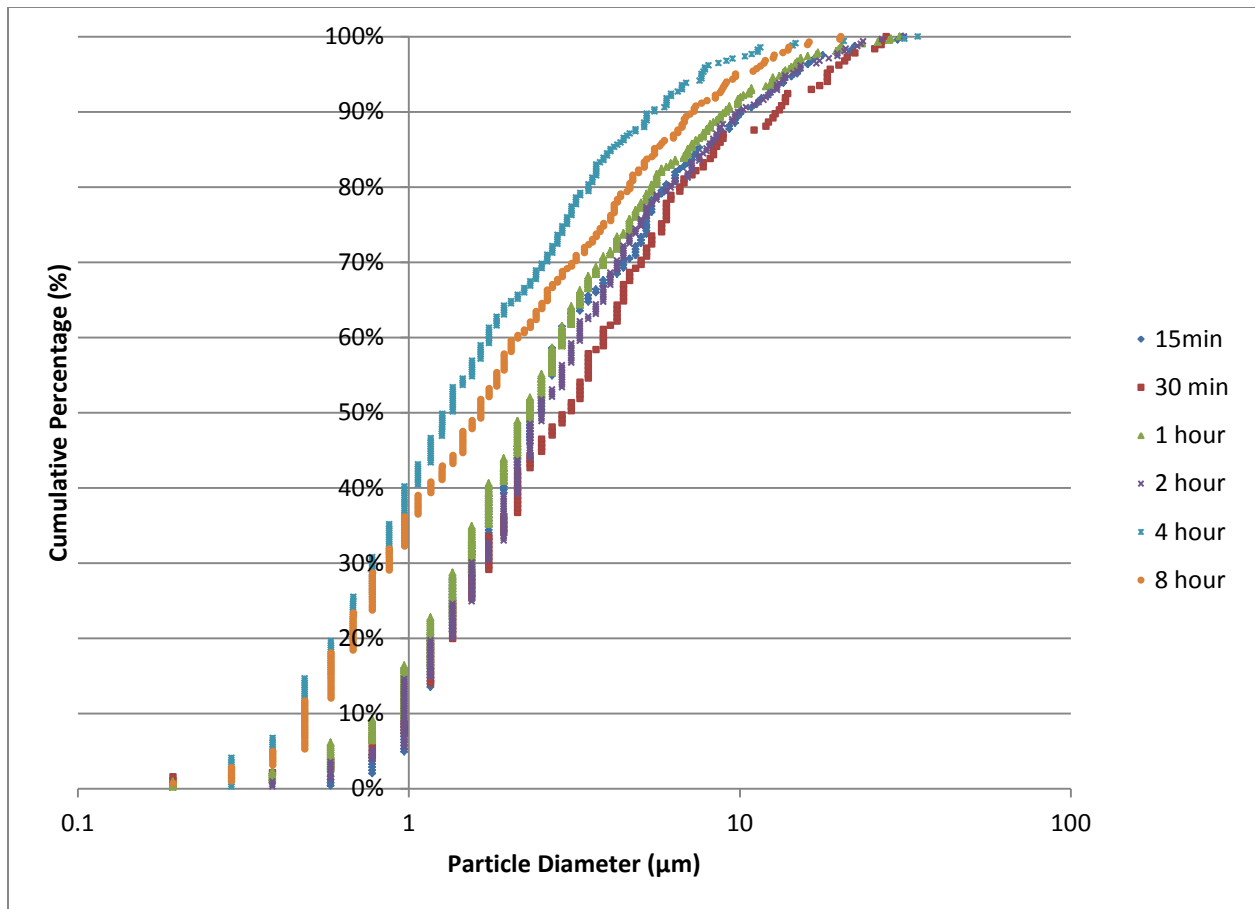


Figure 55: Cumulative mass percentage vs. diameter size for Al_2O_3 particles

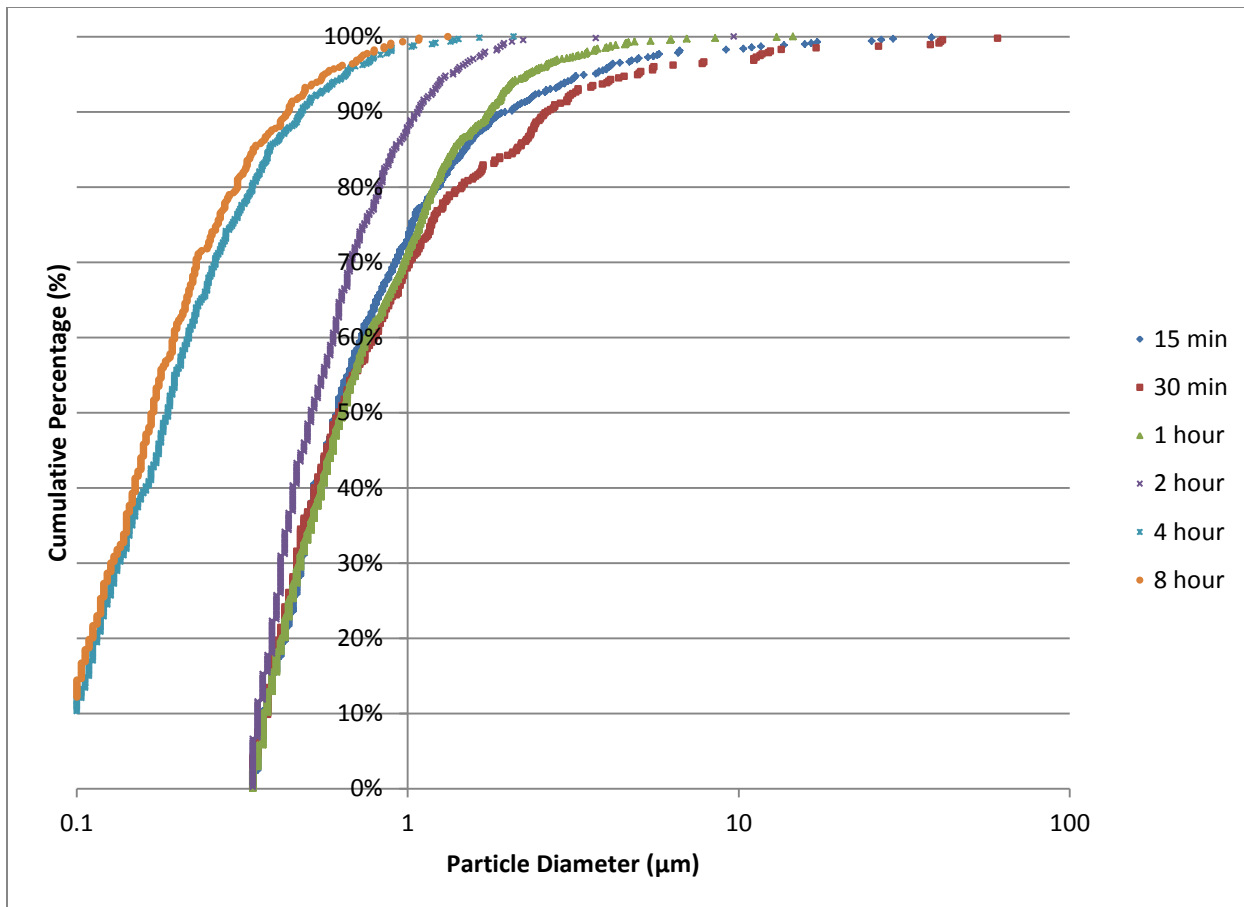


Figure 56: Cumulative mass percentage vs. diameter size for ZrO₂ particles

From these plots the D₅₀ particle size parameter can be determined for both oxides.

Table 11: D₅₀ Sizes of alumina and zirconia after various ball mill times

Time in Mill (h)	Alumina D ₅₀ (μm)	Zirconia D ₅₀ (μm)
0.25	2.52	0.61
0.5	3.10	0.62
1	2.33	0.63
2	2.52	0.51
4	1.36	0.19
8	1.65	0.17

There are a few conclusions to be drawn from Figures 55 and 56 and Tables 10 and 11. Firstly, for mill times less than 4 hours, little change occurs in the average particle size and the d_{50} values. Similarly, 8 hours of milling showed little improvement over 4 hours; therefore, 4-6 hour time frame is selected for milling the ZTA powder. Large particles remaining after milling is a concern due to weak link mechanics of ceramics. Coarsening during sintering is proportional to grain size, particles with order of magnitude sizes greater than the D_{50} will create points of accelerated coarsening leading to weak points within the matrix; these points have the potential to be the origin of failure. It can be seen that for zirconia, 1 hour of milling will reduce the largest particle sizes by roughly an order of magnitude. This process isn't actually reducing the grain size but breaking up agglomerates as seen in Figures 49 and 50. For alumina, milling time did not serve to reduce the largest particles detected by any great factor; however, the difference between the largest particle and the smallest particle of unmilled alumina was not as great as it was for zirconia. To avoid large alumina particles in future work it is recommended that a new source

of alumina particles with greater control over sizing is utilized. The batch of alumina used was sized using a mesh whereas nano-alumina particles produced through a sol-gel method will have a tighter size distribution. Sol-gel method creates particles through the precipitation of oxide from a gelled solution. The ability to control growth time allows for greater control of the products and a much tighter particle diameter distribution.

5.1.1 Whisker Characterization

Figure 57 shows the mullite whiskers produced by the molten salt method. Individual whiskers have clustered together to form an agglomerate. Agglomeration of the whiskers is expected due to van der Waal forces compounded by high specific surface areas. For rod shaped objects the surface area (SA) to volume (Vol) ratio is shown in equation (55) which can be simplified to equation (56).

$$\frac{SA}{Vol} = \frac{2\pi rh}{\pi r^2 h} \quad (55)$$

$$\frac{SA}{Vol} = \frac{2}{r} \quad (56)$$

It can be seen that the ratio will vary by $2/r$, as the radius of the whiskers decreases the ratio will increase. The whiskers produced have radii between 10 nm and 0.5 μm which means they will have SA/Vol ratios between 2×10^5 and $4 \times 10^4 \text{ cm}^2/\text{cm}^3$. This can be compared to alumina and zirconia powder SA/vol ratios of 3.6×10^3 and $2.5 \times 10^4 \text{ cm}^2/\text{cm}^3$ respectively. Experiments by Rance et al. have demonstrated that van der Waals forces obey a quadratic dependence upon surface area [154], therefore the greater SA/Vol of whiskers leads to greater attractive forces between whiskers.

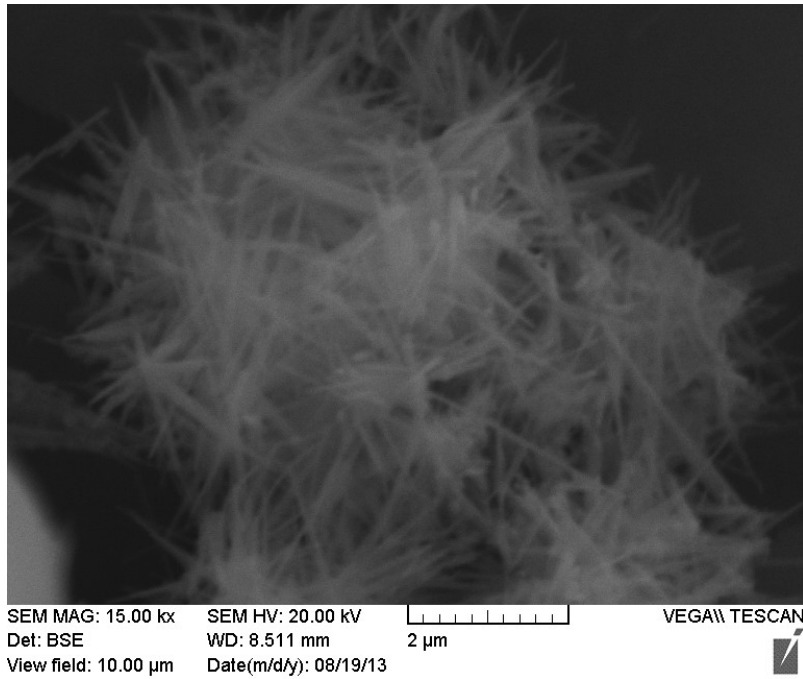


Figure 57: Agglomerated whiskers produced using the molten salt method

Another issue encountered with the mullite whiskers was the growth of multiple whiskers branching in different directions from a single seed as shown in Figure 58.

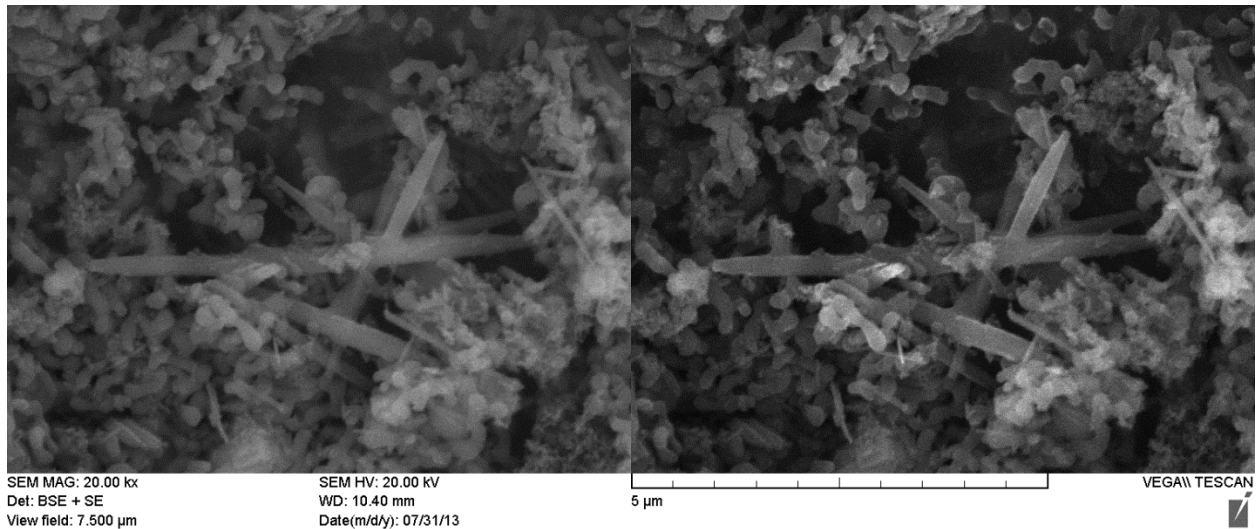


Figure 58: Mullite whisker with several secondary whiskers branching out

When experimenting with different sources of silica, Zhang et al. found that mullite whiskers grown from crystallised silica (quartz) rather than amorphous silica will form spike balls of whisker rather than

individual whiskers, this is due to quartz not completely melting and forming an inhomogeneous mixture in the salt bath as well as surfaces for whiskers to grow from [129]. The occurrence of branched whiskers shown in Figure 58 suggests that there was either a level of inhomogeneity within the molten salt mixture or unmelted silica surfaces for whiskers to form on. The branched nature rather than the centralised spike ball nature of the whiskers suggest that inhomogeneity is likely the reason. Furthermore, evidence of residual silica fume can be seen within Figure 59 showing that some reactants remain after the full 3 hours of 1000 °C.

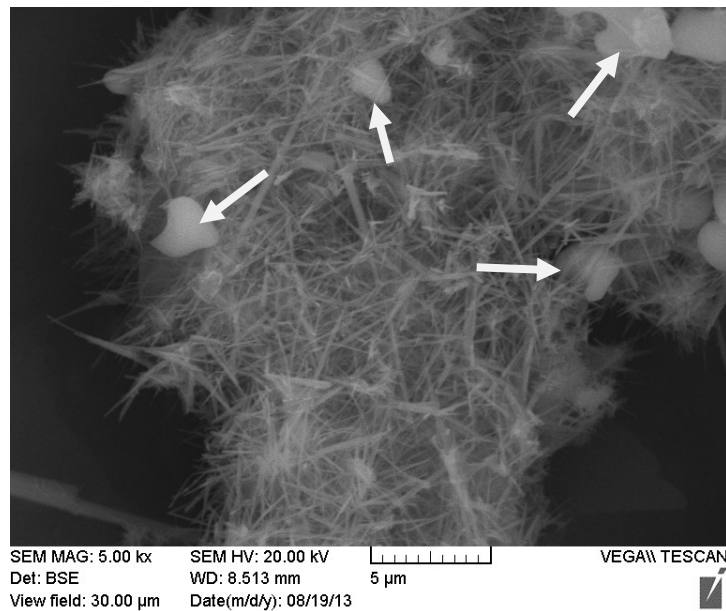


Figure 59: A second SEM image of whiskers produced using molten salt method with evidence of residual amorphous silica (as pointed by arrows)

Work by Wang et al. shows that the mullite whisker forming reaction is spontaneous after 750°C; however, little work has been done to measure and optimize the reaction kinetics to ensure high whisker yield [131]. This could be an area of further research if mullite whiskers are found to be an effective reinforcing material. To remove agglomerations of whiskers, two methods were attempted, the first method used the ball mill which had been previously used to mill raw powders. The rationale behind this method was to pulverise clusters of whiskers apart using the kinetic energy of the milling

media. The second method employed was immersing the whiskers within an ultrasonic bath. SEM scans of the results of both methods are shown in Figures 60 and 61.

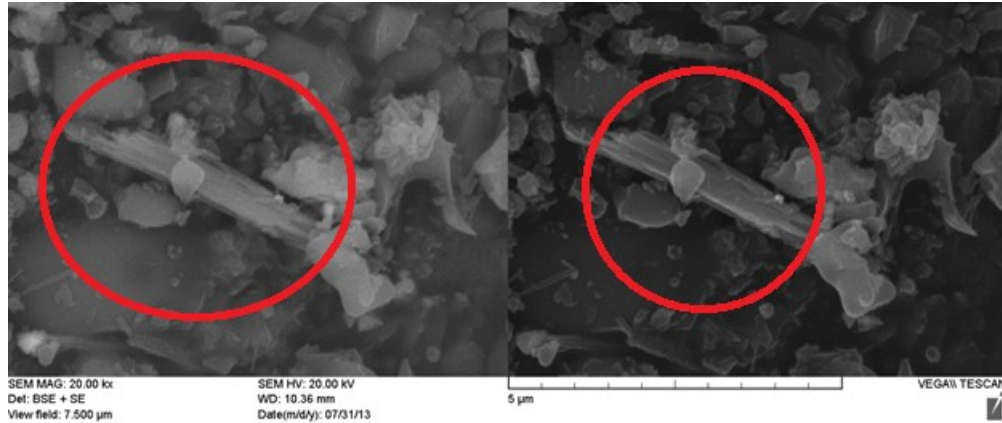


Figure 60: SEM image of mullite whiskers after 150 mins of ball milling at 200 rpm

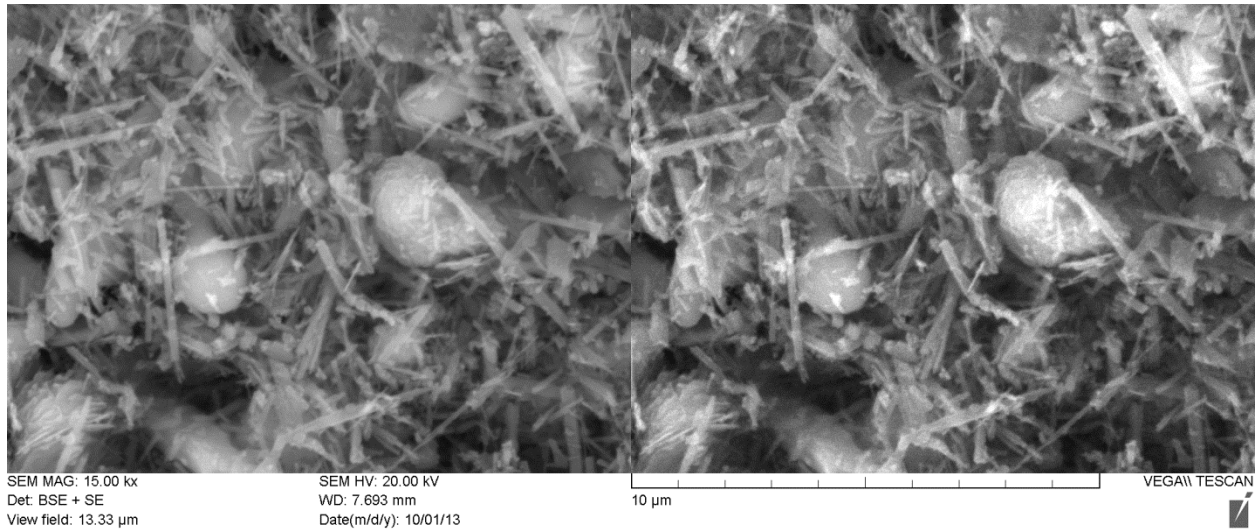


Figure 61: Whisker clusters deagglomerated through ultrasonic bath technique

It can be seen that the ultrasonic bath is an effective method of agitation to separate whisker clusters. The ball milling is effective at reducing the length of the whiskers but has trouble separating clusters of whiskers aligned along c-axis. The ultrasonically processed whiskers show an excellent dispersion in all

directions. It should also be noted that despite using a sediment settling technique, some non-whisker content is still present within the deagglomerated whiskers.

Future batches will utilize a more uniform distribution of whiskers with shorter lengths. This will be accomplished through an extra ball milling stage for the whiskers after the salt has been filtered from the mixture followed by sedimentary settling and further filtering. Shorter whiskers are less likely to interfere with growth kinetics while still providing almost the same level of toughening improvement provided the volume percentage of whiskers is maintained.

5.2 Microstructure of Sintered Samples

The methods outlined in section 4.2 have been utilized to examine the microstructural properties of interest within sintered and post HIPed samples.

5.2.1 Porosity

Table 12 shows the measured porosity of ZTA_n and ZTA_w after the initial stage of sintering for both sintering profiles as well as post HIPed ZTA_w.

Table 12: Porosity of Samples after two different sintering profiles

Sintering Profile	Sample	Porosity
1	ZTA _n	16.9
	ZTA _w	16.22
2	ZTA _n	13.2
	ZTA _w	8.09
Post-HIP	ZTA _w	3.31

It can be seen from the table that by altering the sintering profile porosity has been reduced by almost half before the HIP stage. This is likely due to the reduced ramp up speed controlling the volatilization of the binder and preventing the formation of gas pockets. The increased sintering time at 1600°C also allows longer diffusion time for the sintering mechanics to proceed which results in a greater density albeit greater grain size as well. The improved density is especially important for sealing the pore networks prior to the HIPing stage. The effect of HIPing on the density of ZTA_w is clear, with a reduction of porosity of 4.78% and values approaching the theoretical density. Figures 62 and 63 show the microstructure of the two composites after the different sinter profiles with a clear improvement of density and pore network sealing in the second sintering profile.

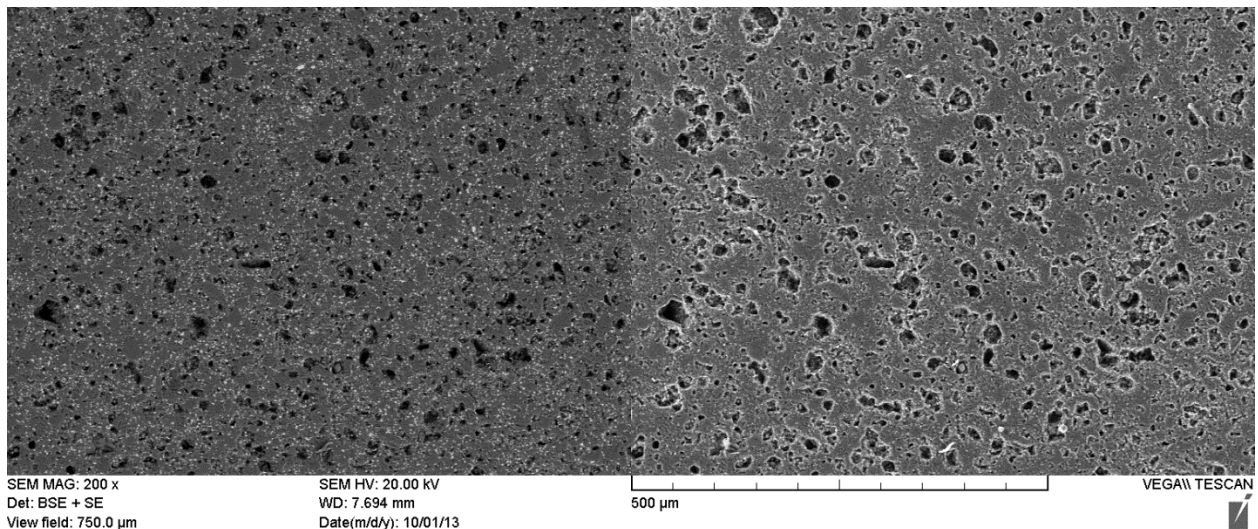


Figure 62: SEM image of the surface of ZTA_w after sintering profile 1

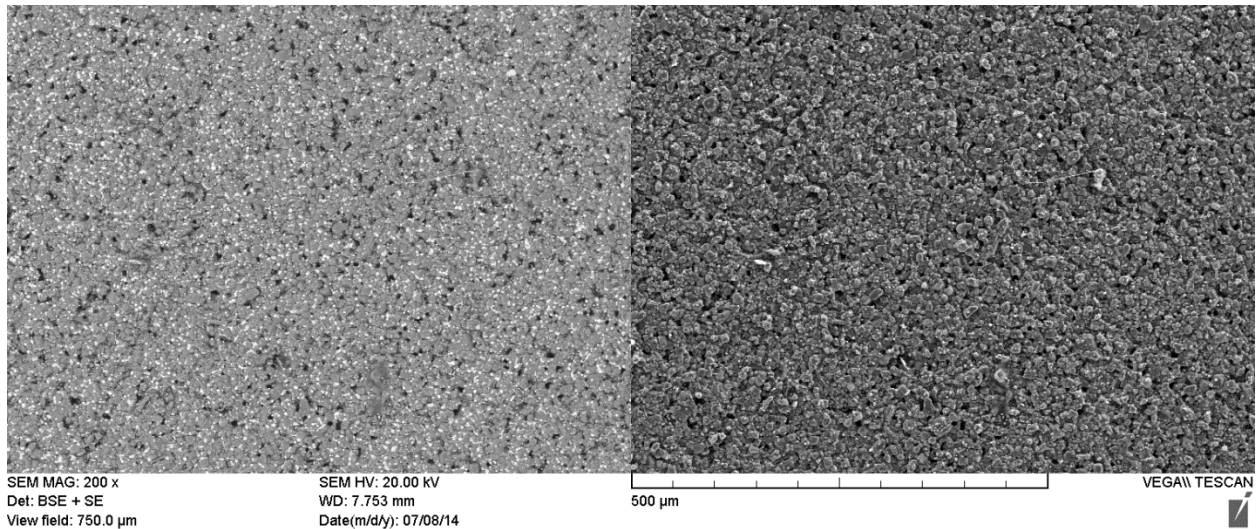


Figure 63: SEM image of the surface of ZTA_w after sintering profile 2

The control over the binder burn out phase also likely improved the density between the two sinter profiles. To ensure volatilization of the organics within the composite the second sinter profile used an oxygen atmosphere during the early ramp up and burn out phase. Work by Higgins et al. and Masia et al. has clarified the importance of oxygen in the binder removal process with Masia et al.'s results showing a 7.6 times reduction in carbon ppm in alumina sintered in air over argon [145] [155]. From a qualitative perspective, evidence of carbon residue exhibited by black patches within the sample was greatly reduced using the second sintering profile seen in Figure 64.



Figure 64: ZTA_w after second sintering profile with no visible evidence of residual carbon

5.2.2 Grain Size and Orientation

Figures 65 and 66 show SEM images of the surfaces of ZTA_w and ZTA_n after the second sintering profile.

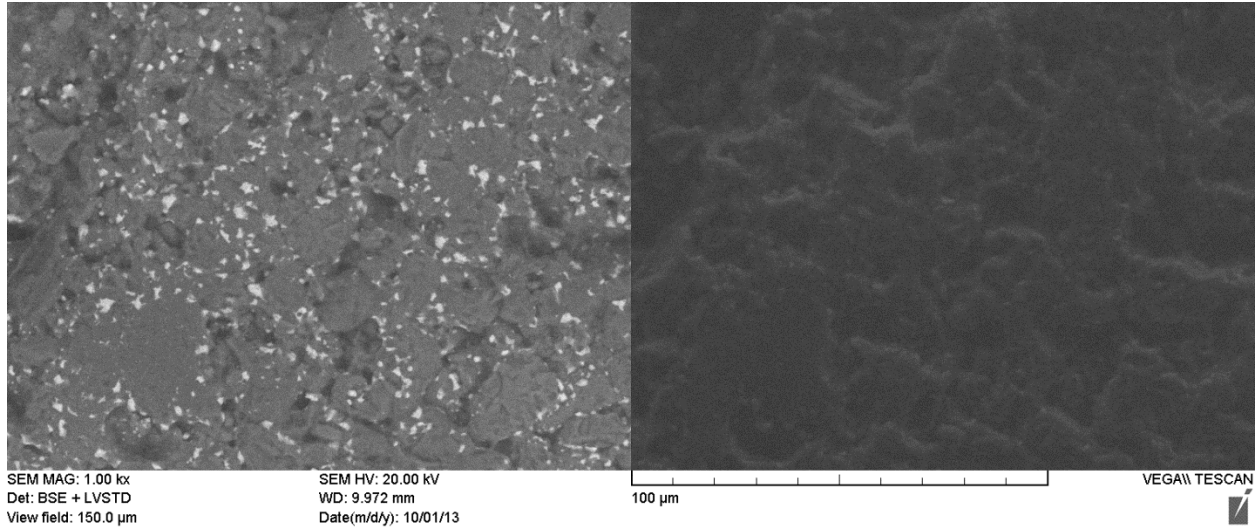


Figure 65: Polished and etched ZTA_n sample at 1 kx magnification

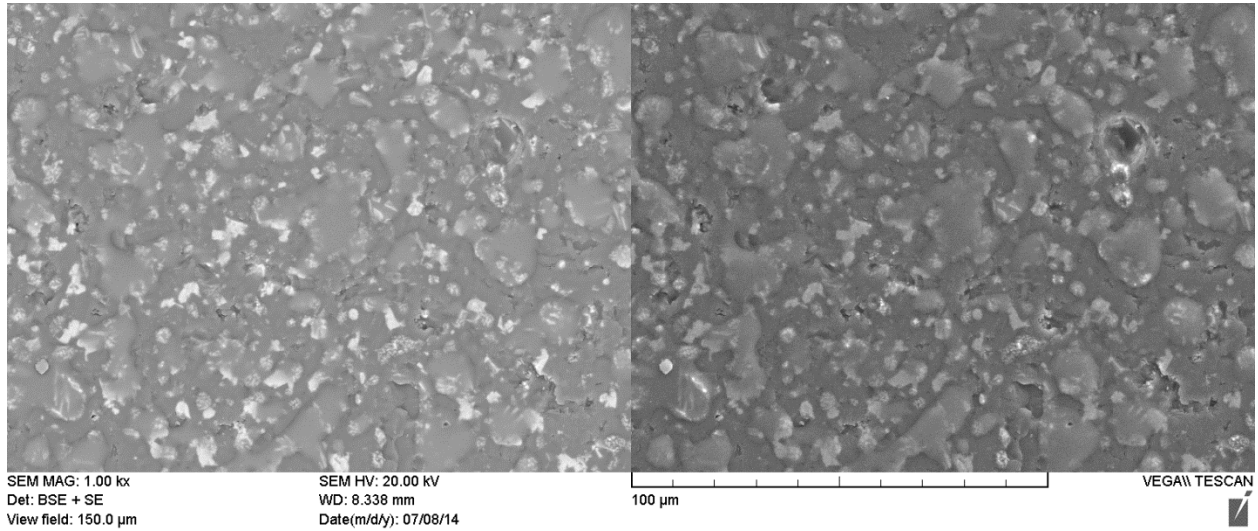


Figure 66: Polished and etched ZTA_w sample at 1 kx magnification

The linear intercept method was used to estimate the alumina grain size of ZTA_n and ZTA_w on polished and etched surfaces while the particle analysis method has been used to estimate the zirconia grain size; the values are reported in Table 13.

Table 13: Average grain size of ZTA_n and ZTA_w after sintering

Sample	Al ₂ O ₃ Grain Size (μm)	ZrO ₂ Grain Size (μm)
ZTA _n	6.71	0.78
ZTA _w	5.57	0.69

Smaller grain size is desirable in many materials; in metals the Hall-Petch relation given by equation (57) links grain sizes to strength in an inverse fashion.

$$\Delta\sigma \propto \frac{k}{d^x} \quad (57)$$

Where *k* is the strengthening coefficient, *d* is the grain size and *x* is a material specific exponent [156]. In ceramics the smaller grain size is correlated with less surface defects which also increases the strength [157]. The changes in grain size vs. particle size due to coarsening effects during sintering and HIPing are shown in Table 14.

Table 14: Change in size between particles and grains after sintering of ZTA_n and ZTA_w

Sample	Al ₂ O ₃ (% increase)	ZrO ₂ (% increase)
ZTA _n	126	239
ZTA _w	87.5	200

Figure 67 highlights the positioning of secondary phases within ZTA_w. The zirconia phase situated at the triple points helps pin the grain boundaries of the alumina phase and both prevents grain growth and reduces the strain rate of secondary stage creep [158]. Using equation (42) from section 3.4 one would expect pure alumina with a particle size of 2.97 μm to have a grain size of 9.81 μm at 3.3 % porosity, which is almost twice the average grain size measured, showing the contribution of ZrO₂ to grain growth retardation.

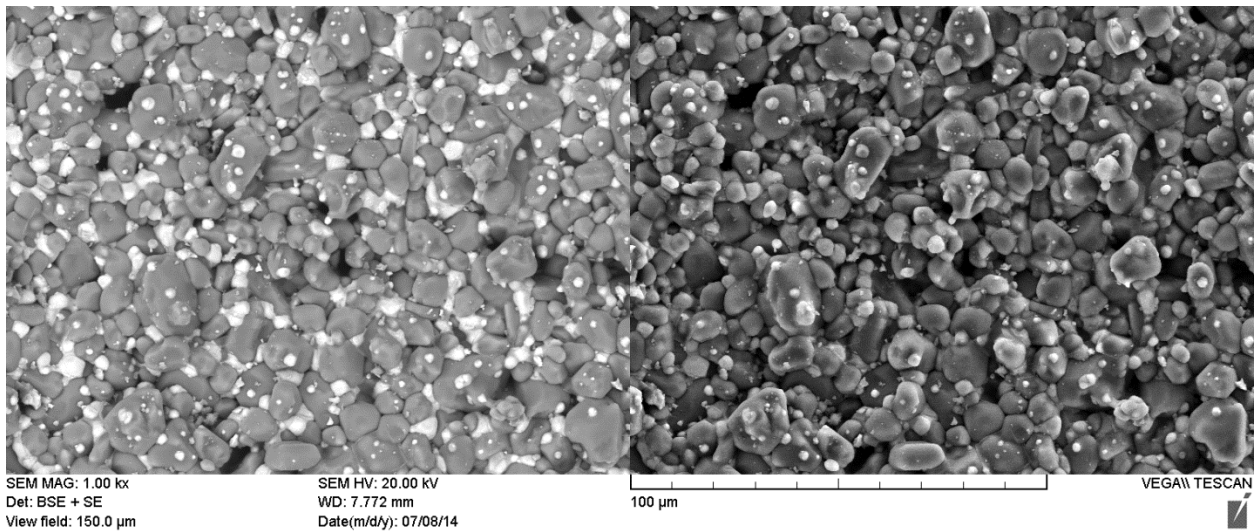


Figure 67: SEM image of ZTA showing ZrO₂ located at triple points of Al₂O₃, 1000 times magnification

The mullite whiskers are expected to play a role in preventing sintering and reducing creep. An example of an agglomeration of mullite whiskers leading to reduced density is shown in Figure 68.

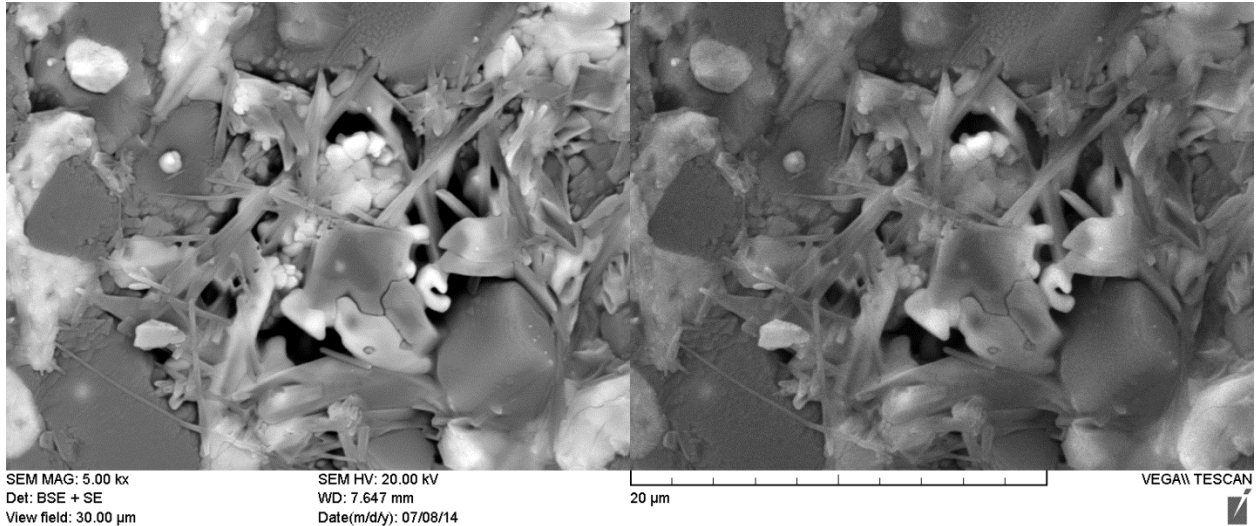


Figure 68: Clustered whiskers preventing ZTA_w densification

The whiskers were effective at preventing contact between adjacent particles and delaying sintering process. Some whisker clusters allowed effective densification as shown in Figure 69 where the surrounding particles were able to maintain contact during sintering.

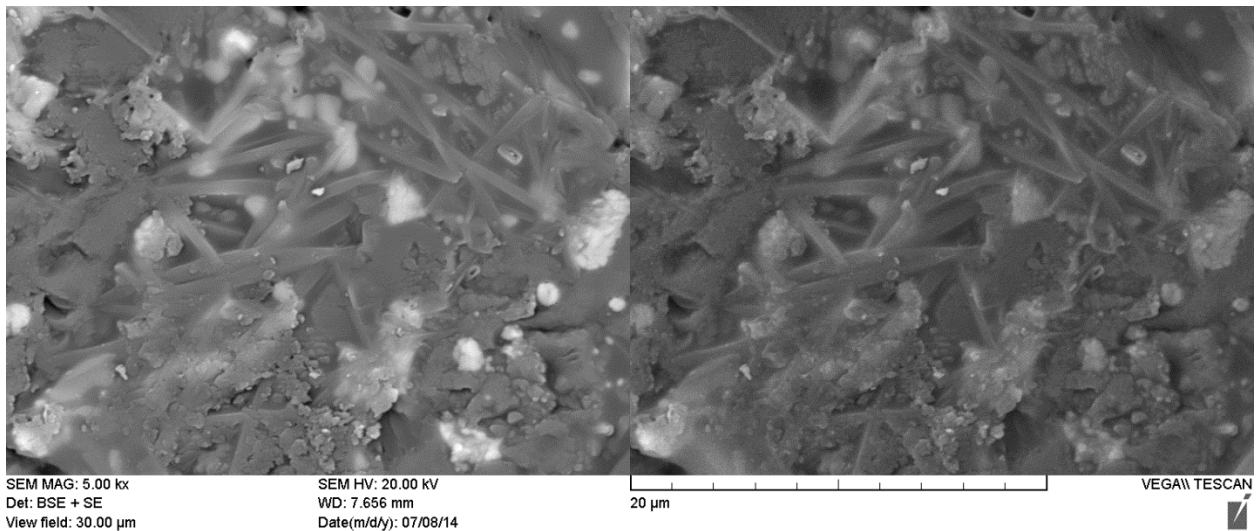


Figure 69: Clustered whiskers allowing ZTA_w densification

To allow for densification, particles between the whisker clusters must be able to contact and the whiskers must be able to adjust to each other without forming a network as covered in section 2.3.4. One method which may be explored in the future would be to examine the zeta potential of the

whiskers and tune the acidity of the solution so that the whiskers and particles have opposite charges, this would ensure that particles are attracted to the whiskers, coating them and preventing large whisker networks from forming prior to and during sintering.

Another issue which can occur is agglomeration of particles themselves. In the current iteration of processing method this issue predominantly occurred during the drying stage after filtration. These agglomerates sinter faster than the surrounding matrix and create large areas of local porosity as they pull away from the rest of the matrix. Evidence that this may have occurred in the second sintering batch is shown in Figure 70.

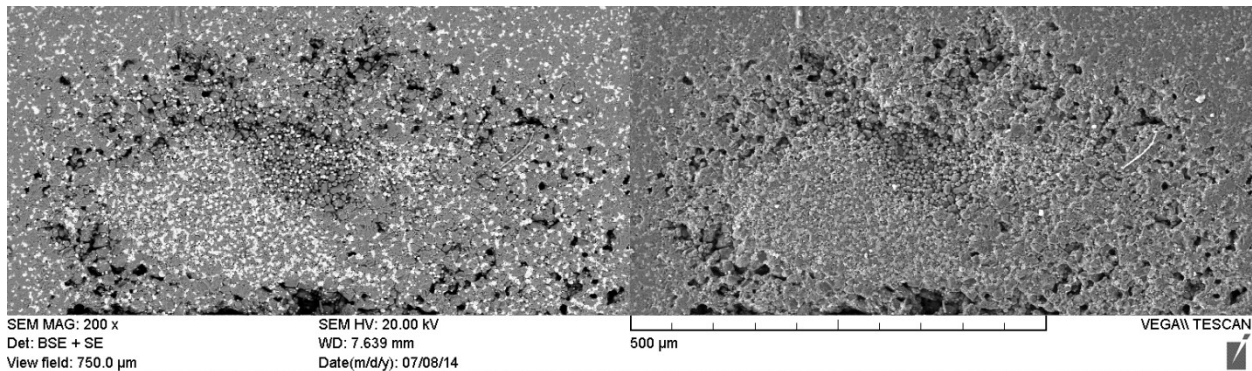


Figure 70: A microstructural defect characterised by increased porosity

As with the whisker agglomerates, these areas may act equivalent to a large void within the matrix most likely acting as a fracture initiating weak point. In future studies several methods will be employed to prevent this issue. One method is to add a sifting step after the PVA has been applied, this should prevent large agglomerates from being incorporated into the green compact. A second method to be explored is to add the PVA to the acidic slurry then filter the liquid content using a circular filter with the same diameter as the press. The tight packing of the particles during filtering would be preserved during the cold pressing, removing the likelihood of individual tightly packed agglomerates surviving through the PVA application process.

5.2.3 Crystal Structures of the Phases

The XRD scans of the powder and the sintered ZTA_n and ZTA_w samples can be seen in Figures 71 to 76.

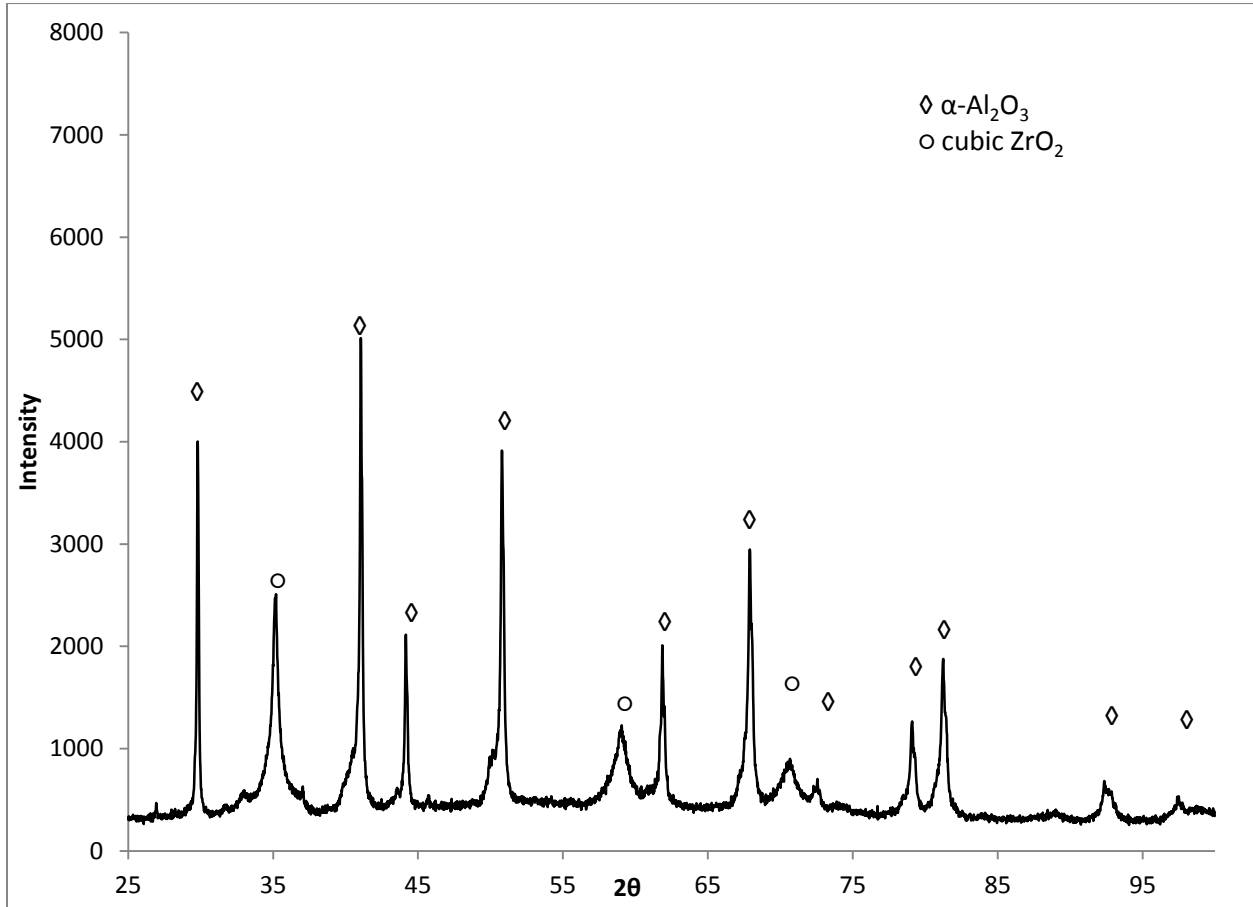


Figure 71: XRD spectrum of ZTA_n powder

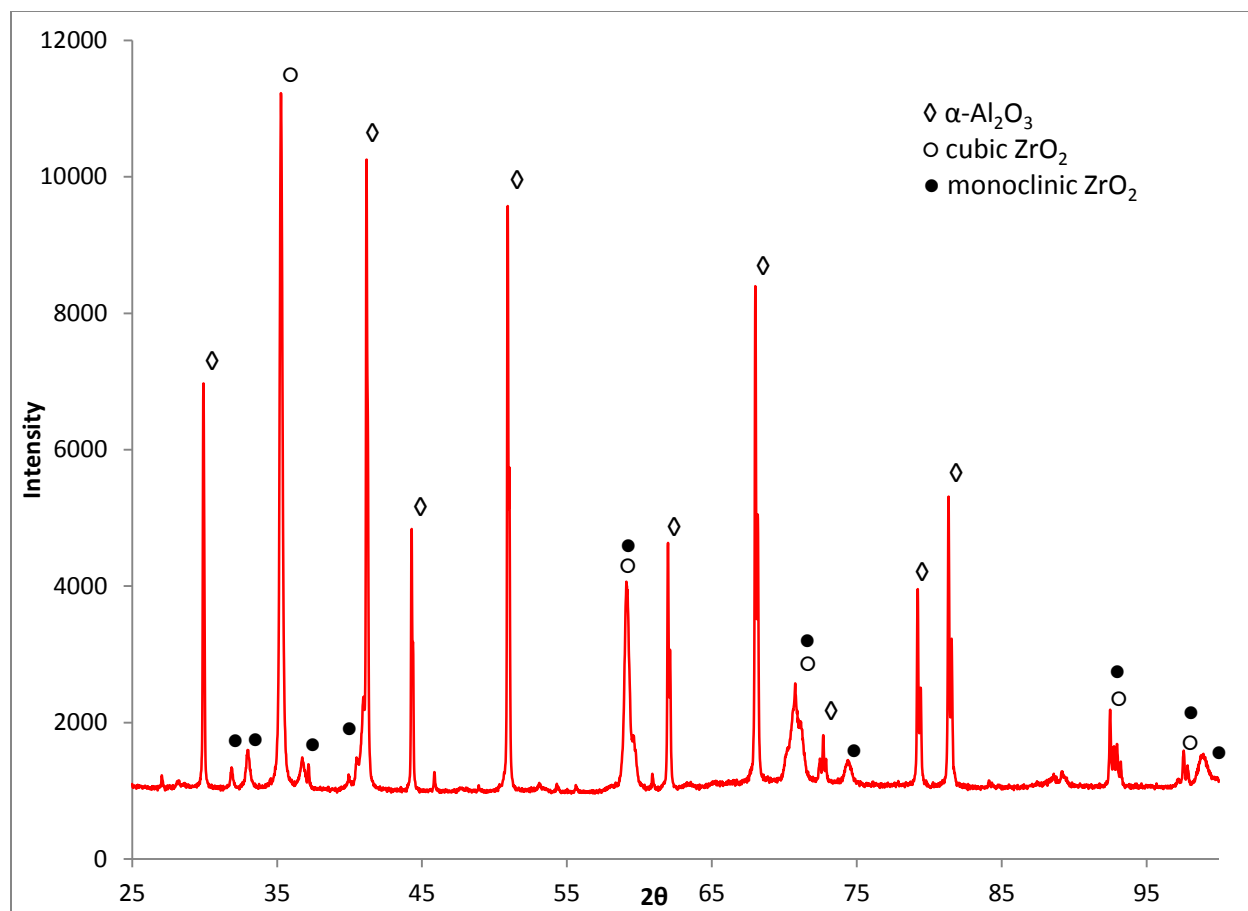


Figure 72: XRD spectrum of ZTA_n sample post-sintering

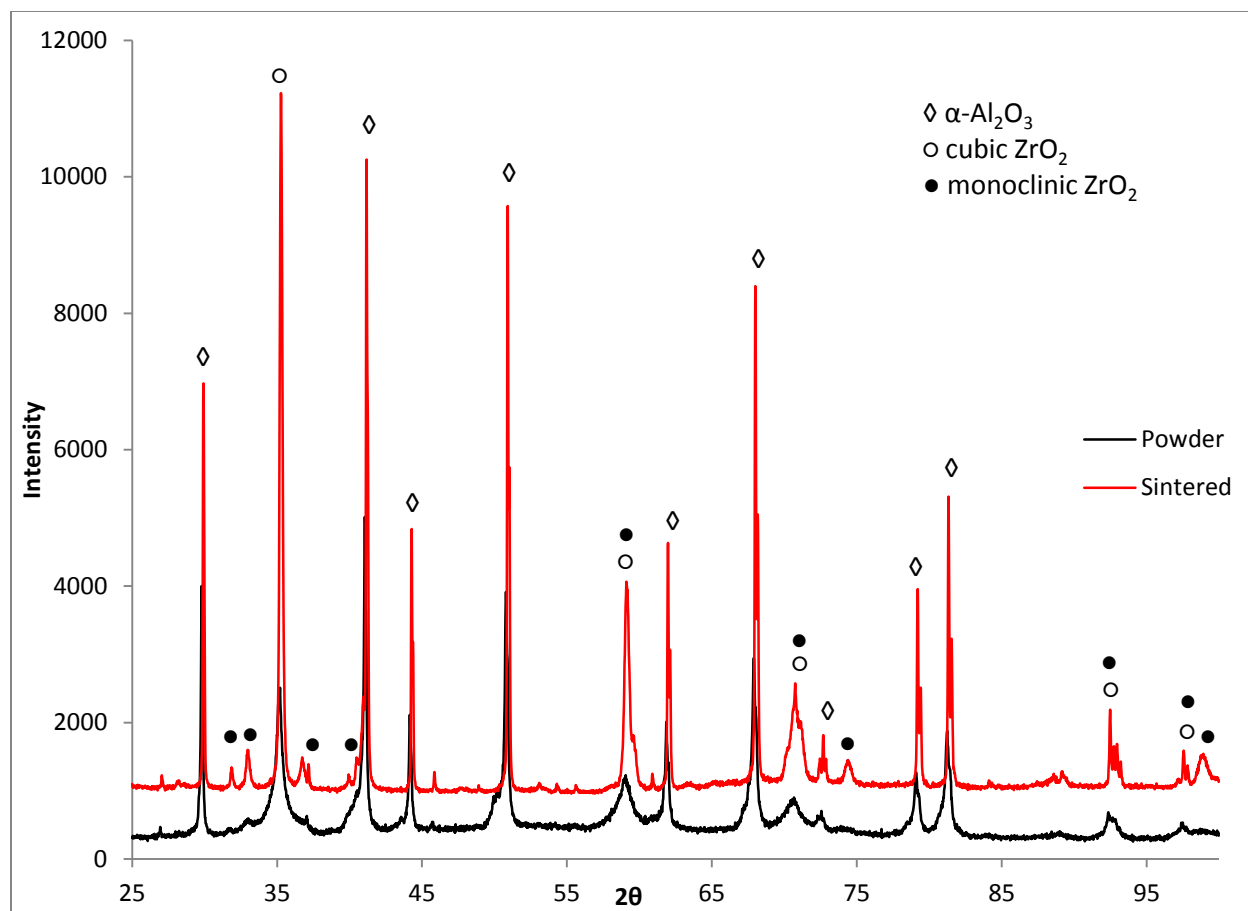


Figure 73: XRD spectrum of ZTA_n powder with sintered ZTA_n overlaid to show phase changes during sintering

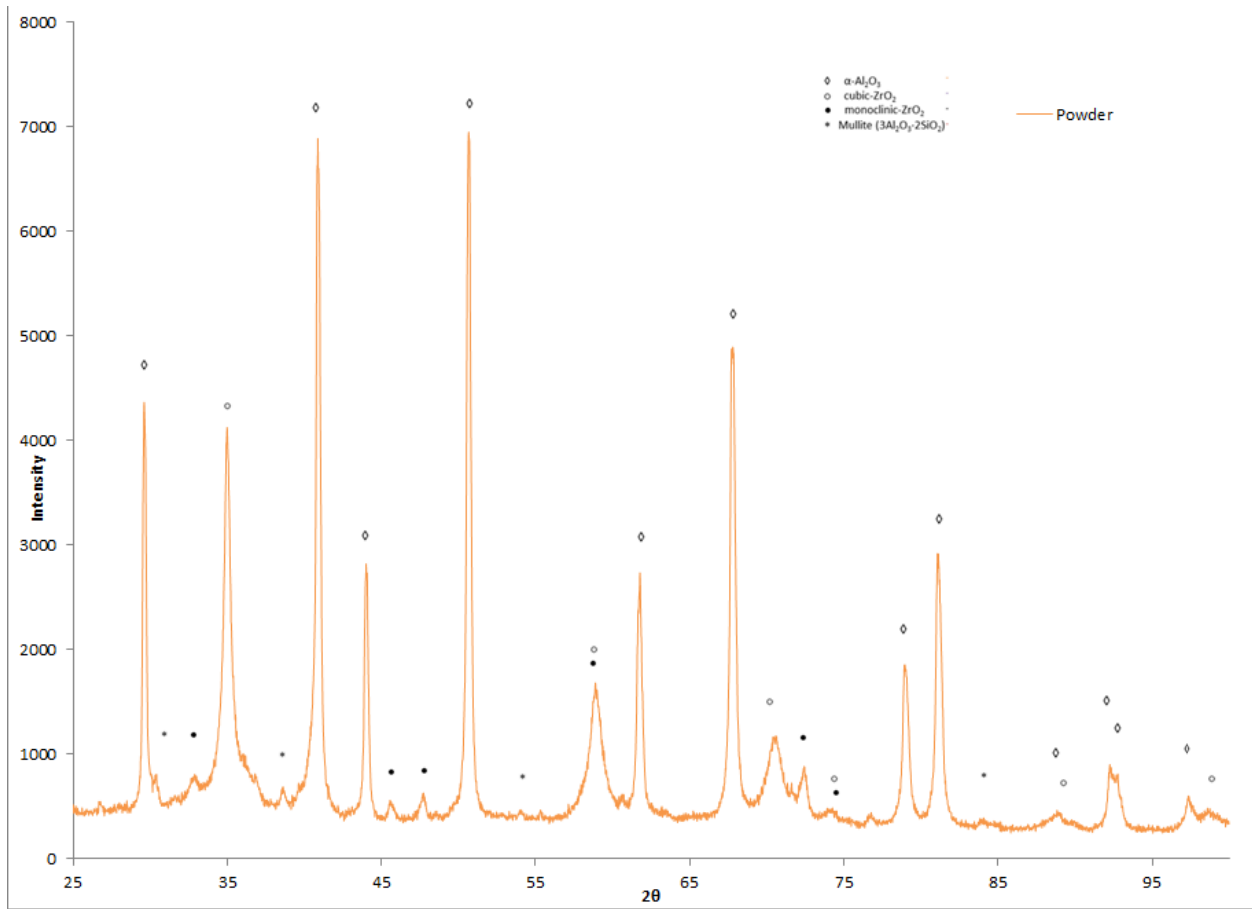


Figure 74: XRD spectrum of ZTA_w powder prior to sintering

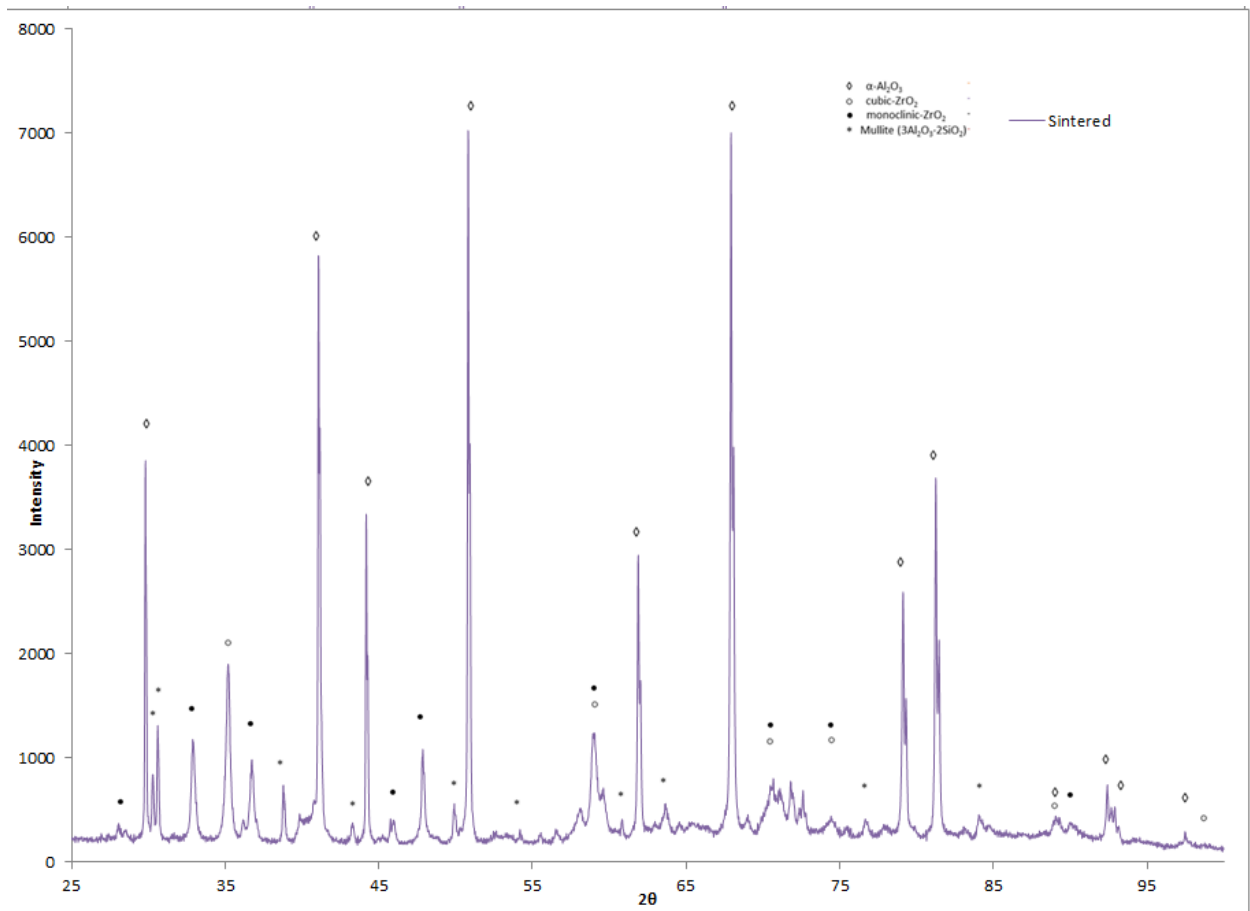


Figure 75: XRD spectrum of ZTA_w post HIP process

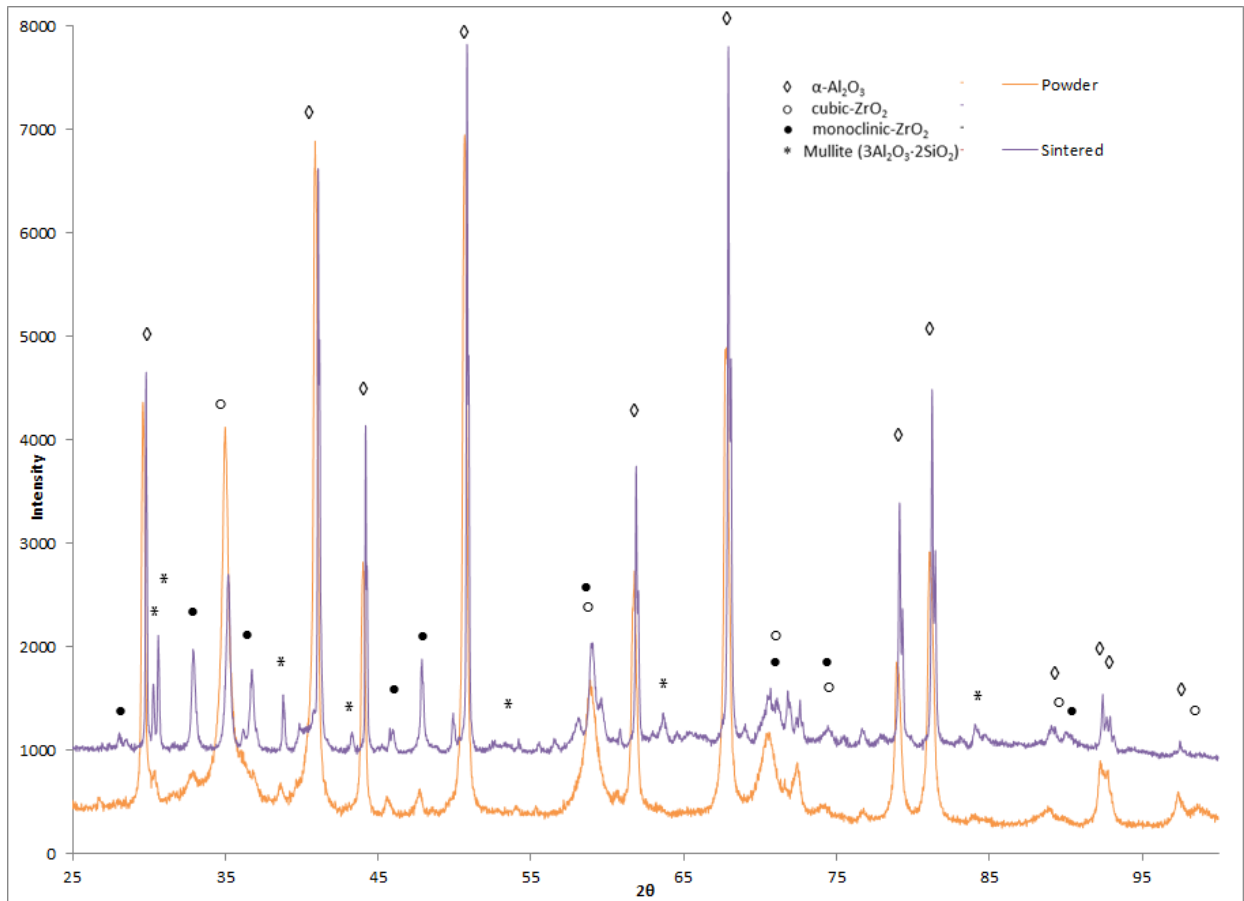


Figure 76: XRD spectrum of ZTA_n powder with sintered ZTA_n overlaid to show phase changes during sintering

ZTA_n powder primarily is made up of α -alumina and cubic-zirconia. The ZTA_w powder shows a similar composition as ZTA_n; however, there are several peaks representing the orthorhombic-mullite phase which makes up the whiskers. The XRD spectra of the sintered samples are compared to the powder samples to determine phase changes occurred during the sintering stage. Evidence of amorphous silica or yttria in the ZTA_w would suggest that the mullite whiskers are reacting with other oxides within the matrix during the heat treatment. The formation of glassy phases is undesirable since it would reduce the creep strengthening property of the whiskers and negatively affect the high temperature lifetime of the material [159] [160]. Figures 73 and 76 show XRD spectra of the powder and the sintered sample.

In Figure 73 the formation of monoclinic phase can be clearly seen. The phase diagram of yttrium stabilised zirconia is shown in Figure 77. The phase diagram shows that only cubic phase should appear during sintering; however, during cooling from sintering temperature and when cooling rate is sufficiently low, cubic phase will transform to tetragonal phase and then monoclinic phase ($c \rightarrow c+t \rightarrow c+m$). Work by Lakiza and Lopato has shown that the alumina-zirconia-yttria system will not produce any ternary products at the concentrations used in this work (Figure 78) [161].

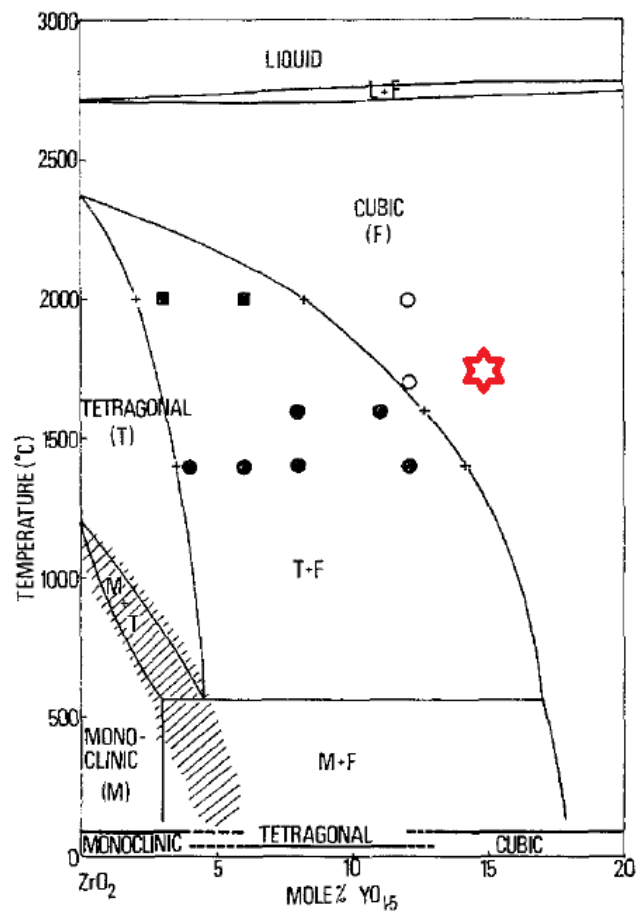


Figure 77: Phase diagram zirconia rich region of the zirconia-yttria system, ● represents compositions and temperatures which will result in monoclinic-cubic mixtures of ZrO₂ at room temperature, whereas ■ represents tetragonal + monoclinic, and ○ represents cubic. The red star represents the samples YSZ at sintering temperature [162]

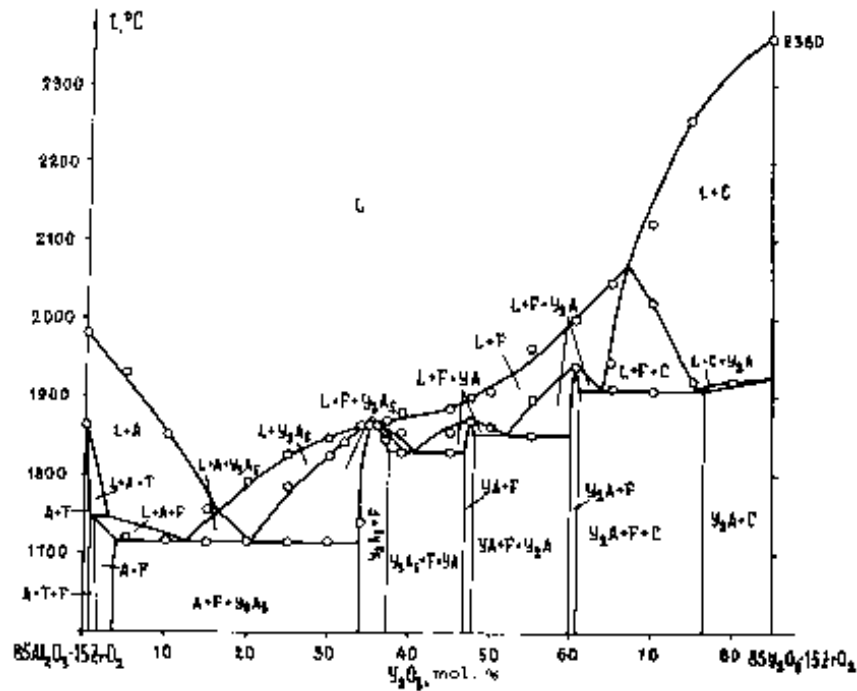


Figure 78: Phase diagram of 85%Al₂O₃-15%ZrO₂-Y₂O₃ system [161]

Impurities introduced during processing would also alter the X-ray diffraction peaks, either by altering the lattice spacing and crystal structure of the constituents if the impurity is dissolved by an already present phase, or by creating new products/phases.

5.2.4 EDS analysis results

EDS spectra of ZTA_n and ZTA_w are shown in Figures 80 and 82. It should be noted that an Au coating was used to provide conductivity during the SEM examination so while the presence of chemical constituents should be accurate, the weight percentages given by the EDS will be incorrect (as Au signal is also collected during EDS scans). Figure 80 confirms the presence of Al, Zr and O in the ZTA_n sample while Figure 82 clearly shows the elemental presence of Si, Al and O in the whiskers. Steel contamination was one concern due to the steel container used during ball milling; however, no traces of iron or carbon were detected in the sintered samples.

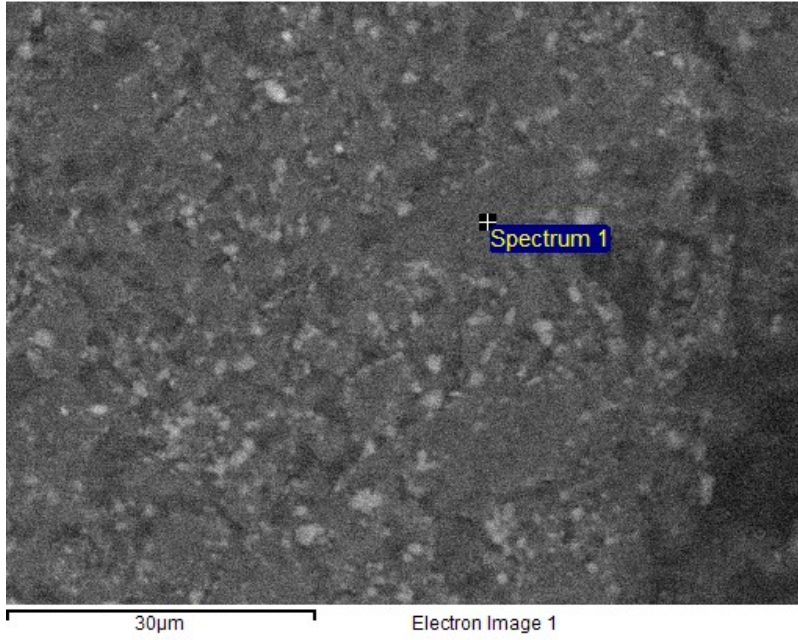


Figure 79: ZTA_n area scanned for EDS analysis

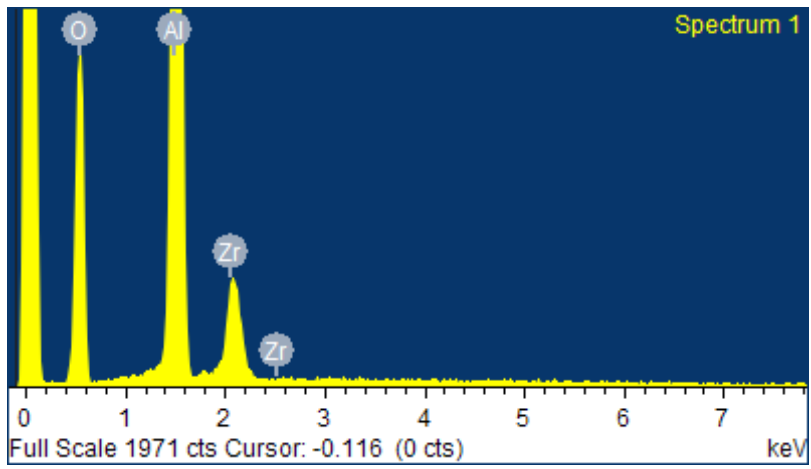


Figure 80: EDS analysis of ZTA_n

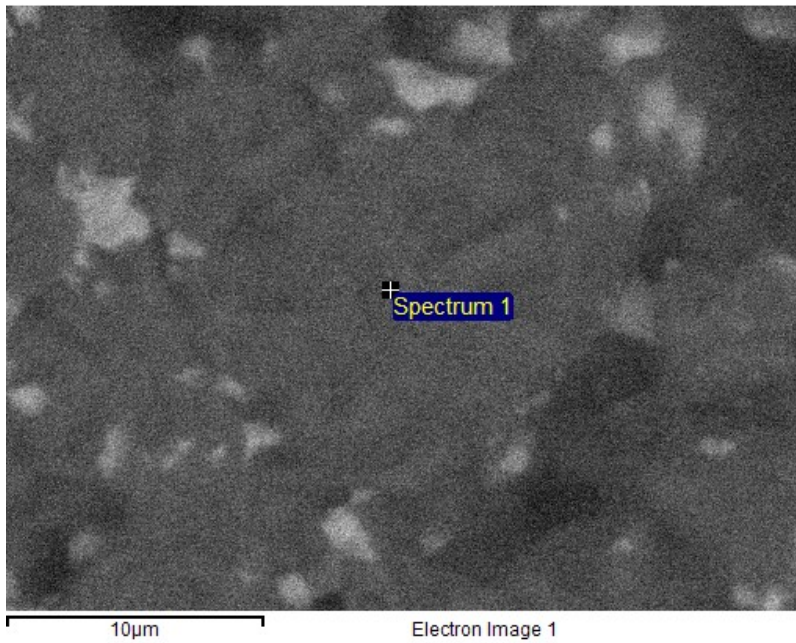


Figure 81: Area scanned for ZTA_w analysis

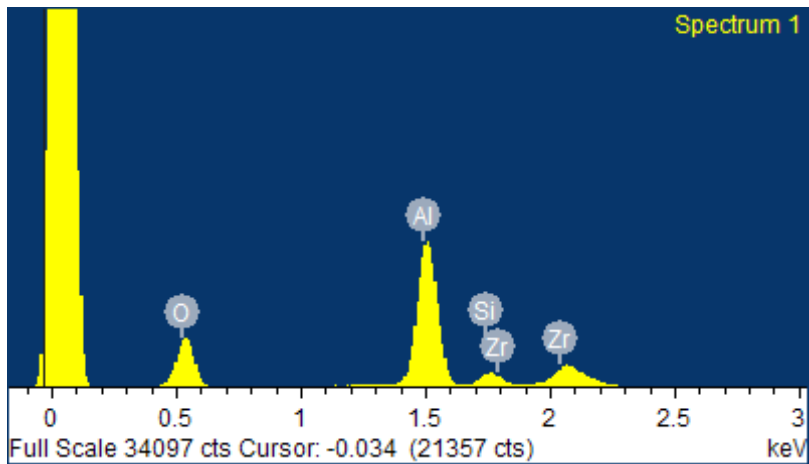


Figure 82: EDS analysis of ZTA_w

5.3 Room Temperature Mechanical Properties

The flexural strength and fracture toughness of ZTA_n and ZTA_w have been tested using a 3 point bend fixture and a microindenter. The results are presented in the following sections.

5.3.1 Room Temperature Flexural Strength of the Composites

Room temperature strength was measured for the two different sintering profiles reported in section 4.4. The Strength results from the first sintering profile are reported in Table 15.

Table 15: Flexural Strengths of Samples Sintered Using Sintering Profile 1

	Sample	Flexural Strength (MPa)
ZTA _n	1	22.44
	2	17.77
	3	23.86
	4	32.26
ZTA _w	1	39.52
	2	56.04
	3	39.87
	4	54.33
	5	39.55
	6	27.40

The low reported strengths led to the adoption of the second sintering profile, the strengths of the samples tested using the second sintering profile are reported in Table 16.

Table 16: Flexural Strengths of Samples Sintered Using Sintering Profile 2

	Sample	Flexural Strength (MPa)
ZTA _n	1	44.47
	2	80.61
	3	61.12
	4	69.55
	5	51.15
	6	65.62
	7	54.75
	8	66.44
ZTA _w	1	107.54
	2	160.94
	3	107.84
	4	200.90
	5	106.69
	6	130.65

The average measured flexural strength of the two composites are reported in Table 17. An example of a stress strain curve is reported in Figure 83, this curve shows linear elastic behaviour until failure which justifies the use of equation (48) from section 4.6.1.

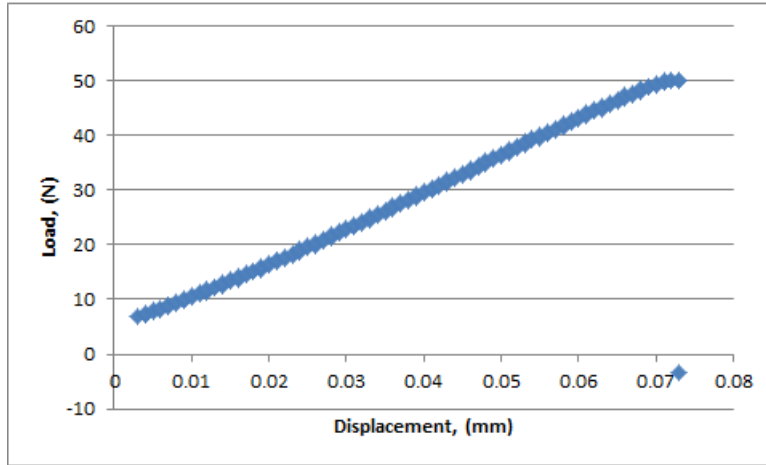


Figure 83: Load-Displacement Curve of ZTA_w Sample 3

Table 17: Flexural strength values of ZTA_n and ZTA_w after 2 different sintering profiles

Sintering Profile	Sample	Elastic Modulus, E (GPa)	Strength, Flexural strength, σ_f (MPa)
1	ZTA _n	11.78	24.09
	ZTA _w	13.47	42.78
2	ZTA _n	72.14 ± 2.05	61.71 ± 0.99
	ZTA _w	76.06 ± 1.42	135.76 ± 1.30

The first set of strengths and elastic moduli given in Table 15 are for samples sintered using profile 1. Due to the high porosity present in the samples, the strength values measured are far below what was an expected strength in the range of 350 to 600 MPa based upon ZTA strength values from the reviewed literature [54]. Furthermore, samples may have experienced internal crushing during the flexural test, as such the reported elastic modulus values may not be accurate. The second sintered samples (profile

2) display higher densities and behaviour closer to what was expected although strength values are still low, especially when compared to the desired properties 425 MPa from section 2.2.1. To improve the strength further, fabrication techniques will need to be refined to reduce and eliminate flaws within the microstructure. It can be seen in Figure 70 that even with the improved sinter profile, there are still areas within the sample where flaws are concentrated. Despite the low reported strengths, the improvement in flexural strength provided by incorporating whiskers is clearly seen in Table 17.

As covered in sections 2.2.1, 2.2.2, and 2.2.7 the strength of a ceramic or discontinuously reinforced CMC will be closely related to the fracture strength and flaw sizes. Using equation (8) from section 2.2.2 and the reported toughness in section 5.3.2 it can be predicted that the average flaw size which caused the failure was 1.68 mm for ZTA_n and 1.05 mm for ZTA_w. The flaw shown in Figure 70 is roughly half of that predicted for the failure of ZTA_w, it is possible that larger flaws exist. This is especially true in ZTA_n where the porosity is greater than ZTA_w. If both samples were to have a maximum flaw size of 1.05 mm than a reported strength of 77.97 MPa would be expected for ZTA_n. From Table 5 in section 2.3.3 it can be seen that commercial alumina possess a strength of 380 MPa and fracture toughness of 3.5 MPa·m^{1/2} at room temperature, based on these properties the maximum expected flaw size would be 21.5 μm. With an identical maximum flaw size the expected strength of ZTA_n and ZTA_w would be 545.02 MPa and 948.91 MPa respectively. It can be seen that the large inherent flaws within the produced ceramic greatly reduce the observed strength.

5.3.2 Microhardness and Fracture Toughness of the Composites at Room Temperature

Figure 84 shows an image of a crack generated during micro-indentation test used to determine the hardness and fracture toughness. The calculated toughness values for each test are reported in Table 18.

Table 18: Fracture Toughness measurements of ZTA_n and ZTA_w

	Sample	Fracture Toughness (MPa·m ^{1/2})
ZTA _n	1	4.46
	2	4.89
	3	3.87
	4	4.39
	5	7.71
	6	5.06
	7	4.86
	8	5.80
	9	5.59
	10	5.54
	11	5.11
	12	4.45
	13	3.49
ZTA _w	1	11.33
	2	7.26
	3	9.33
	4	8.52
	5	8.69
	6	7.22
	7	8.91
	8	10.04
	9	8.61
	10	11.30
	11	7.12
	12	6.59

Table 19 shows the calculated average values of hardness and fracture toughness gathered from the test.

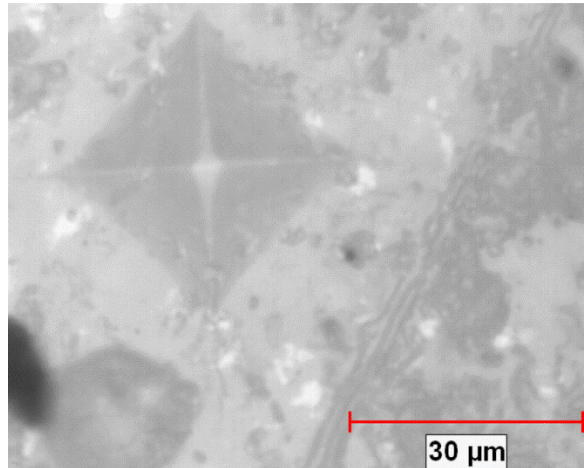


Figure 84: Micro indented ZTA_w with microcracks originating at the edges of the indentation (the arrow indicates the crack propagation from the tips of the diamond impressions)

Table 19: Fracture toughness and hardness of ZTA_n and ZTA_w

Sample	Fracture Toughness, K (MPa·m ^{1/2})	Standard Deviation (MPa·m ^{1/2})	Hardness, Vickers Hardness, H (GPa)	Standard Deviation (GPa)
ZTA _n	5.02 ± 0.21	1.01	10.73	0.26
ZTA _w	8.74 ± 0.24	1.50	11.99	0.86

It should be noted that using a micro indenter to determine toughness, while being an accepted test for brittle materials, will report the localized toughness surrounding the indented area [153]. By sampling many areas of the ceramic certain degree of confidence was established. However, the true toughness

of the material is better represented by a notched test which allows global toughening systems to take effect [163]. For the data presented here over 10 indentations from each sample were taken, and every indent was spaced at a minimum of 50 μm from any previous locations.

It can be seen from Table 16 the effect the whiskers have on toughening; an increase in fracture toughness by 74% is realized. This is 37% larger than the predicted value of $2.71 \text{ MPa}\cdot\text{m}^{1/2}$ which was calculated using formulas (29) and (30) from section 2.3.3. The experimental toughness has exceeded the predicted toughening increase by an absolute value of $1.01 \text{ MPa}\cdot\text{m}^{1/2}$, greater than that predicted based on known toughening mechanisms. Additional toughening mechanisms may include stress concentrations introduced by thermal expansion mismatches between the matrix and the whiskers and potential crack bowing due to whiskers [100]. The fracture surface of ZTA_w was examined for signs of whisker toughening. Figure 85 shows evidence of whisker pull-out along the fracture surface.

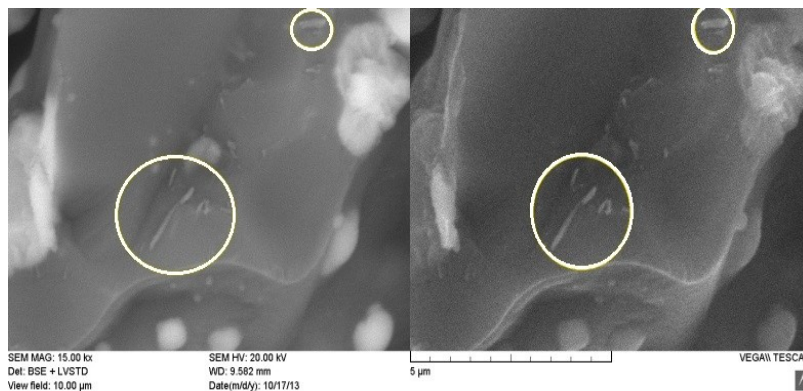


Figure 85: SEM image of ZTA_w fracture surface with evidence of whisker pull-out circled

Toughness values of composites from Table 3 show similar values of toughness for ZTA_n when compared to other alumina based composites. The measured toughness of ZTA_n was $5.02 \text{ MPa}\cdot\text{m}^{1/2}$ while $\text{Al}_2\text{O}_3/10\%\text{SiC}$ has of reported toughness of $5.2 \text{ MPa}\cdot\text{m}^{1/2}$, and $72\%\text{Al}_2\text{O}_3/11\%\text{mullite}/17\%\text{ZrO}_2$ has a reported toughness of 5.25. Similarly, ZTA_w with a reported toughness of $8.74 \text{ MPa}\cdot\text{m}^{1/2}$ can be compared with $\text{Al}_2\text{O}_3/20\%\text{SiC}_w$ which has a reported toughness of $8.7 \text{ MPa}\cdot\text{m}^{1/2}$.

It can be seen from the results that the whisker content has little effect on the reported hardness. Work by Nevarez-Rascon et al. [164] has shown similar results while Abdullah et al. [165] have found a slight increase in hardness due to whisker content. A difference seen in the work of Nevarez-Rascon et al. and Abdullah et al. was weight % of reinforcing whiskers where the former used up to 2 wt% and the latter 10 wt%. In both cases hardness was correlated much more closely with density. This conclusion is also supported by the findings of this work.

5.4 High Temperature Mechanical Properties

The expected temperature of operation of the composite has been set to at least 1200°C which is the expected value for advanced materials within the hot sections of the next generation of gas turbines (uncoated superalloys can operate up to 1150°C [6]). Secondly, this is also around the operating temperature for most oxide-oxide fibre based CMCs due to the volatilization of SiO₂ [166] and the region where oxide fibres creep becomes unmanageable [78]. Tests to determine the strength, thermal cycling behaviour and oxidation resistance of the composite have been undertaken at this temperature.

5.4.1 High Temperature Strength of the Composites

Samples were tested in a high temperature bending rig as specified in section 4.4.1. Only samples from following the second sintering profile were tested at high temperature. The measured strengths are exhibited in Table 20.

Table 20: Measure Flexural Strength Values of ZTA_n and ZTA_w at 1200 °C

	Sample	Flexural Strength (MPa)
ZTA _n	1	72.42
	2	46.81
	3	25.97
ZTA _w	1	96.83
	2	91.18
	3	49.73
	4	82.74
	5	91.51
	6	65.04
	7	86.60

The averaged values of strength are reported in Table 21.

Table 21: High Temperature and Room Temperature Flexural Strength of ZTA_n and ZTA_w

Sample	Flexural Strength at Room Temperature, σ (MPa)	Standard Deviation (MPa)	Flexural Strength at 1200°C, σ_{HT} (MPa)	Standard Deviation (MPa)
ZTA _n	61.71	10.68	52.34 ± 15.72	18.99
ZTA _w	135.76	34.94	80.52 ± 13.18	15.72

The force for the high temperature flexural strength was measured using a 5000 lbf (2.2kN) load cell.

The actual loads which the samples experienced were less than 100 N which caused issues for data acquisition. This was especially the case when the furnace was in operation because the transformer within the furnace interfered with the current within the load cell. A 50 Hz Besserer filter was applied to the load cell signal which reduced the interference range to ±10 N. The flexural strength at high

temperatures reported here bears this uncertainty. The flexural strengths of ZTA_n and ZTA_w have dropped to 78.33% and 59.31% of their room temperature values respectively. The properties for commercial alumina shown in Table 5 in section 2.3.3 show a 78.95% drop in strength at 1200 °C, which is similar to that in ZTA_n. From the measured flexural strength reported in Table 21, the effect of whisker additional is clearly demonstrated by a 52% increase although the improvement is not as significant as that at room temperature.

5.4.2 Thermal Cycling and Oxidation Resistance

The reaction of the composite to thermal cycling has been examined through mass analysis, scanning electron imaging and XRD analysis. Figure 86 shows the mass change vs. cycle count for 6 samples of ZTA_w for 450 cycles between room temperature and 1200°C with a dwell time of 40 min at 1200°C. The mass variance reported is the change in mass compared to ZTA_w at 0-cycles. ZTA_n was not tested during this round of tests to focus on the oxidation of the whiskers within the matrix. Previous studies on ZTA compounds have shown very little mass and phase changes during cyclic oxidation [167]. All samples were polished and cleaned in an ultrasonic bath prior to cyclic test.

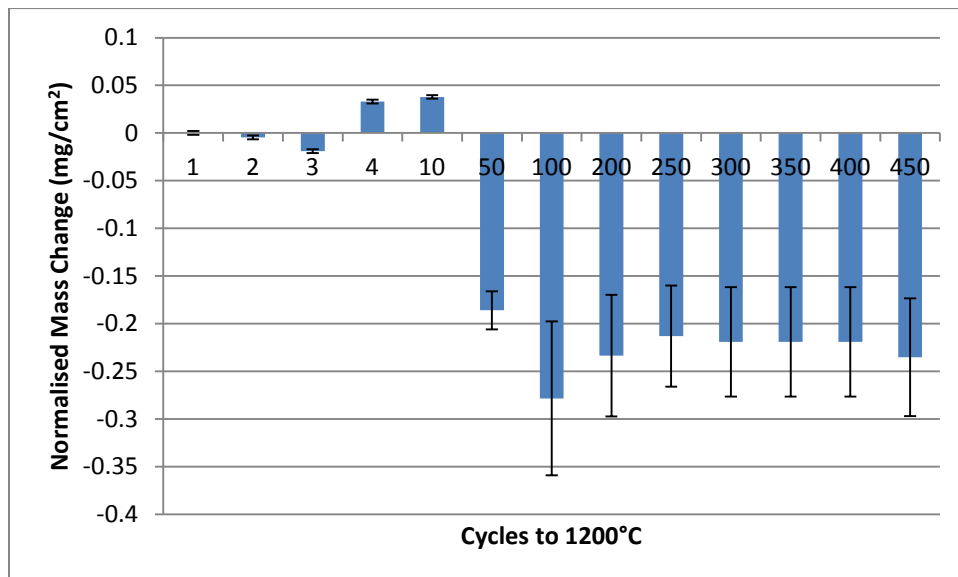


Figure 86: Normalised mass change of ZTA_w vs. number of cycles from room temperature to 1200°C

Figure 86 shows that there is a slight changes in mass for up to 10 cycles, with a small mass gain for the first 3 cycles followed by a slight mass loss. Between 10 and 50 cycles there is a loss in mass which is maintained through the run-out. This behaviour was not anticipated since all components in composite are oxides which should be stable within an oxidizing environment at 1200°C. Figures 87 through 91 shows the surface of the samples after 0, 10, 50, 100 and 200 cycles. There are several features noted. Some surface pores are observed Figure 87. Surface densification seems to have occurred after 10 cycles due to sintering effect.

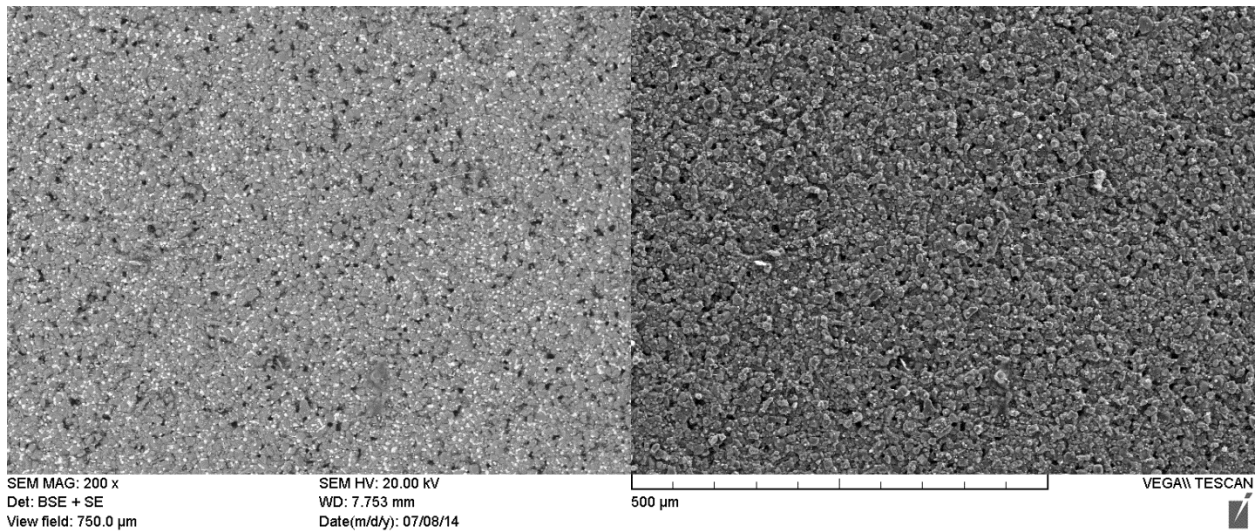


Figure 87: SEM image of ZTA_w after HIP process at 200 times magnification

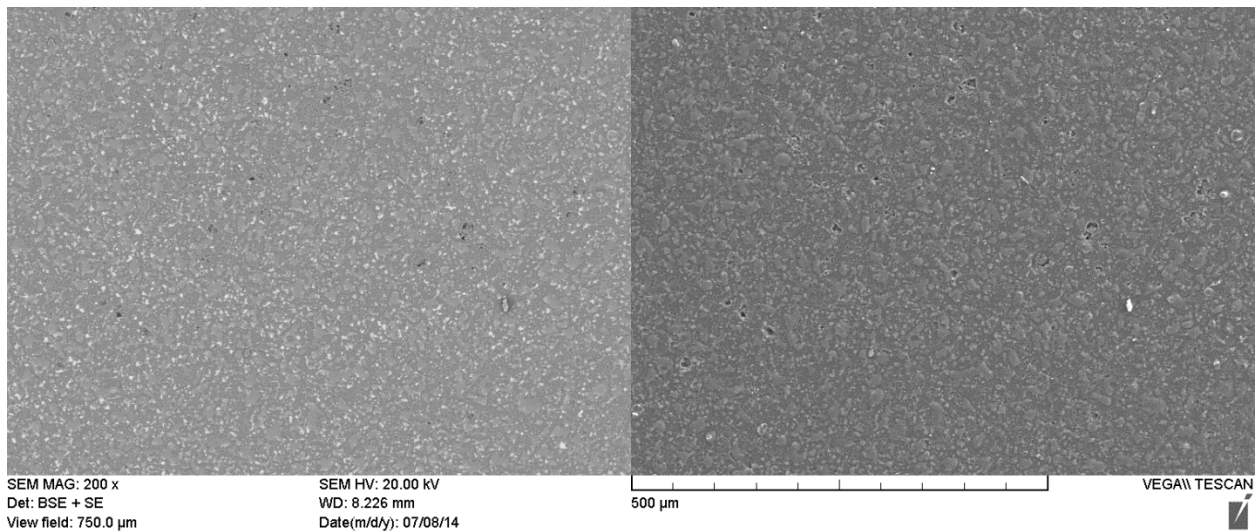


Figure 88: SEM image of ZTA_w after 10 cycles

Contrasting Figures 87 and 88 one can see the effect of 10 cycles to 1200°C. It is clear that some densification occurs but there isn't much evidence of grain growth. This can be seen through both the sizes of the grains as well as their shape, explored further in Figures 92 to 95.

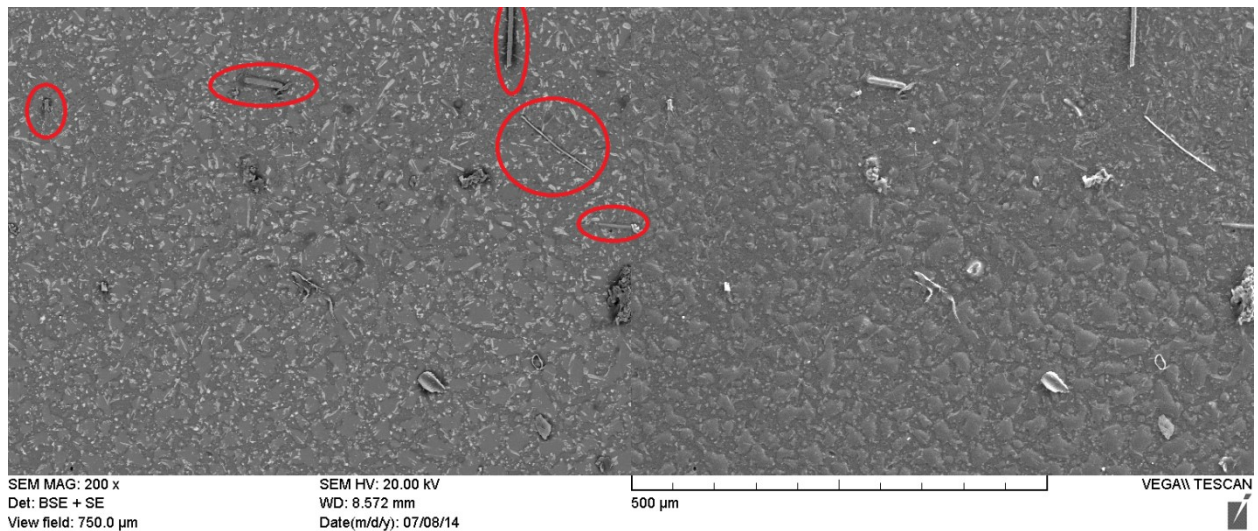


Figure 89: SEM image of ZTA_w after 50 cycles. Red circles point to whiskers.

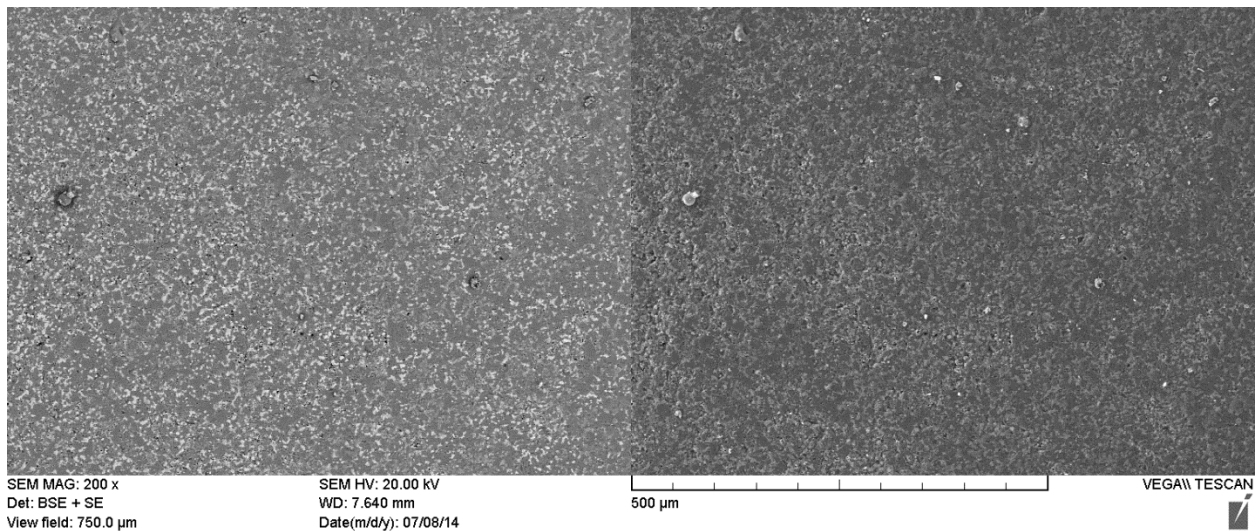


Figure 90: SEM image of ZTA_w after 100 cycles

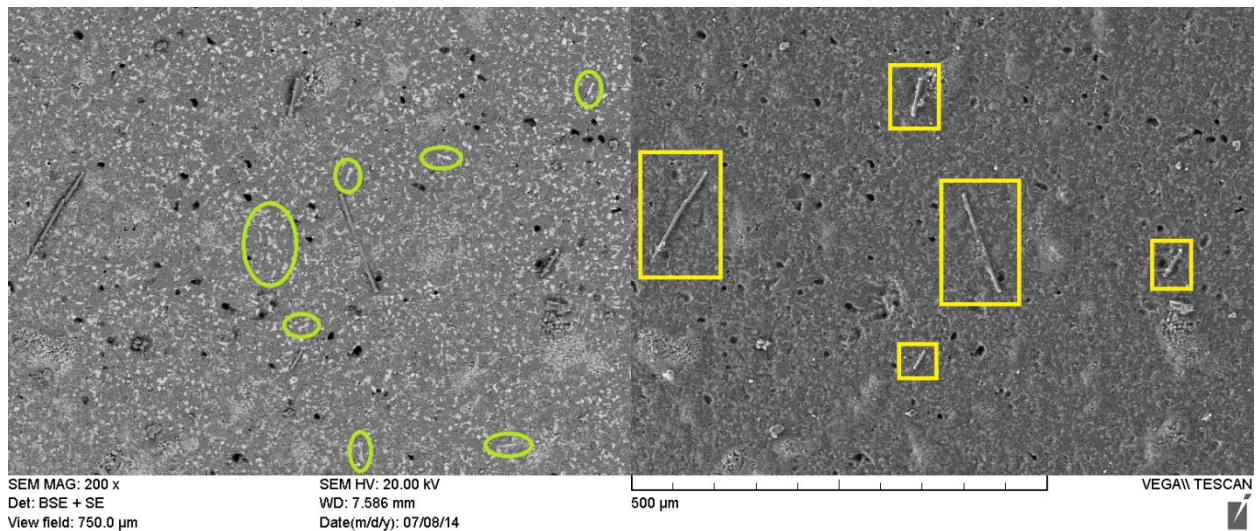


Figure 91: SEM image of ZTA_w after 200 cycles with whiskers in square boxes and examples of elongated zirconia grains in circles

Thermal cycling had no effect on the appearance of whiskers on the surface of the samples. The illusion of this effect is due to the random sampling of the images chosen to exhibit the change in the microstructure due to cycling. Each sample had areas where surface whiskers were apparent in roughly the quantity expected in samples with 20 vol% whisker content.

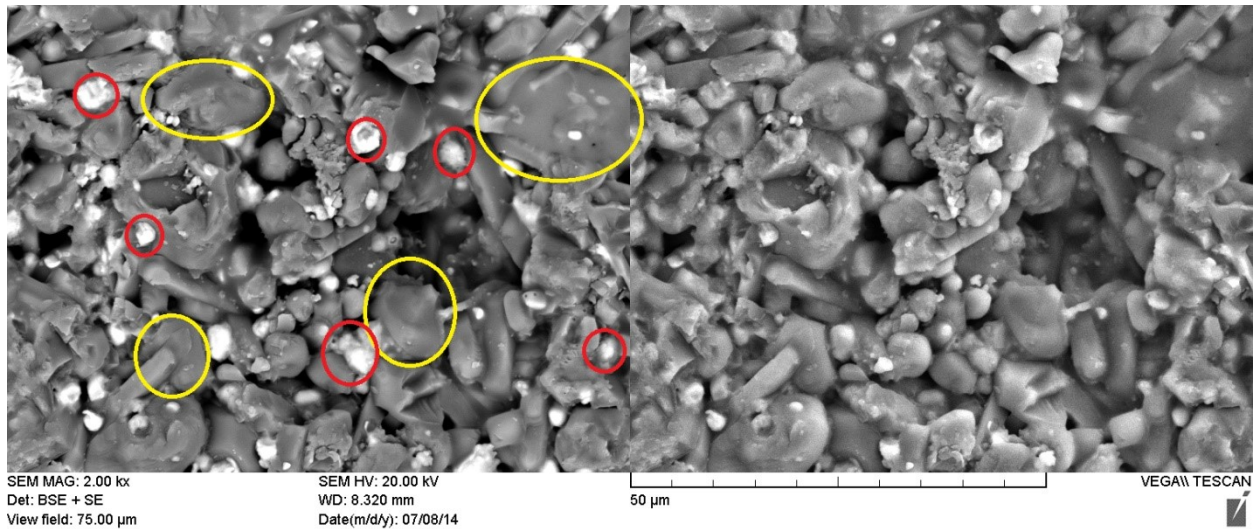


Figure 92: SEM image of ZTA_w before thermal cycling. Red circles highlight zirconia grains and yellow circles highlight alumina grains. There is no apparent whisker content in this sample.

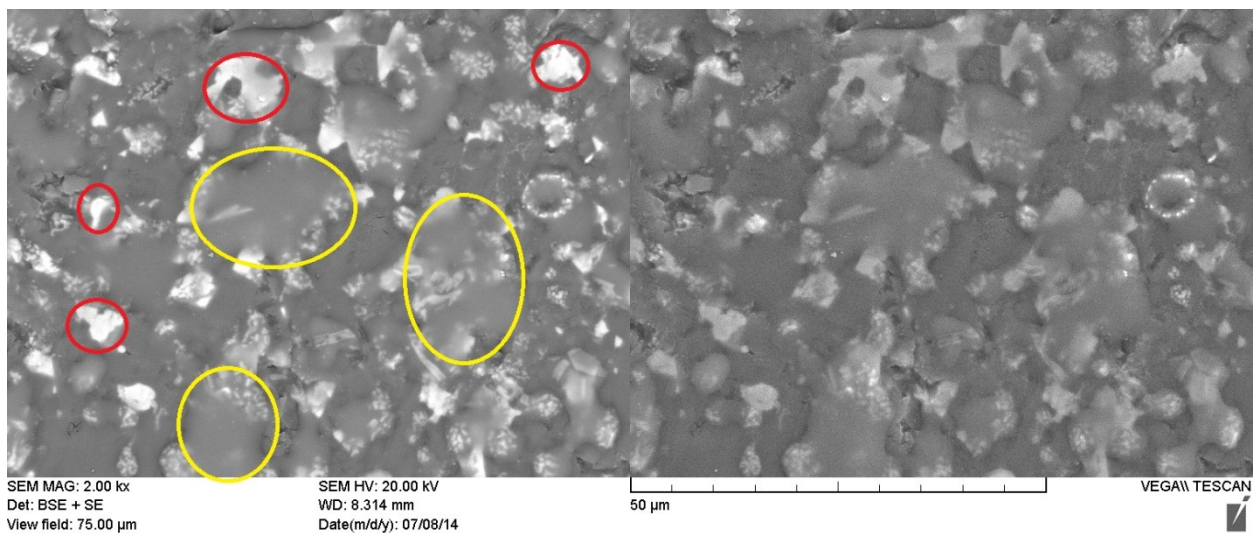


Figure 93: SEM image of ZTA_w after 10 cycles showing densification. Alumina grains circled by yellow and zirconia grains circled by red. There is no apparent whisker content in this sample

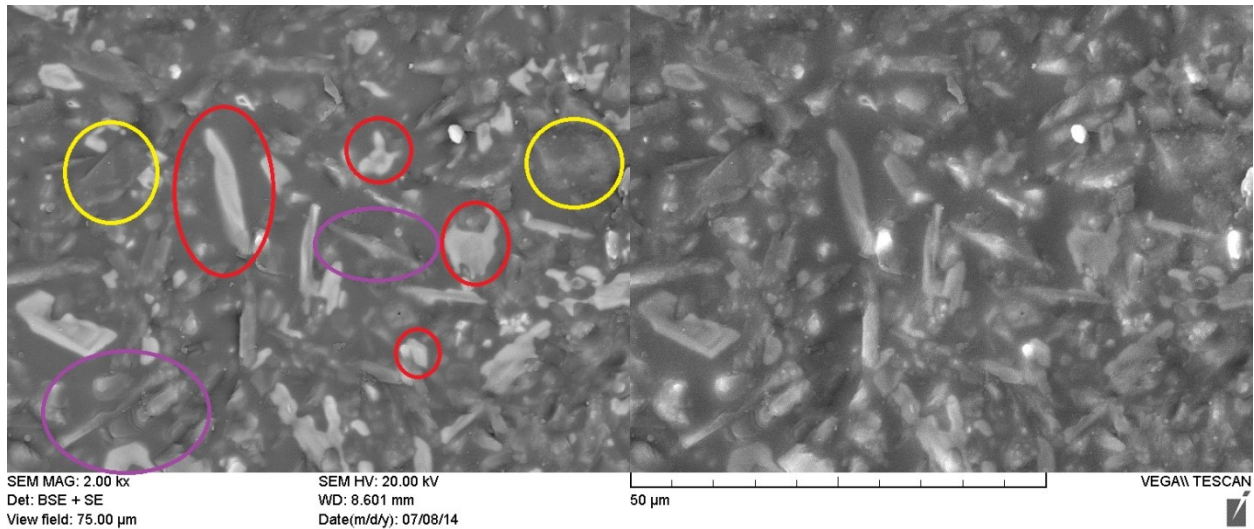


Figure 94: SEM image of ZTA_w after 50 thermal cycles. Purple circles highlight whiskers. Red circles highlight zirconia grains and yellow circle indicates an alumina grain

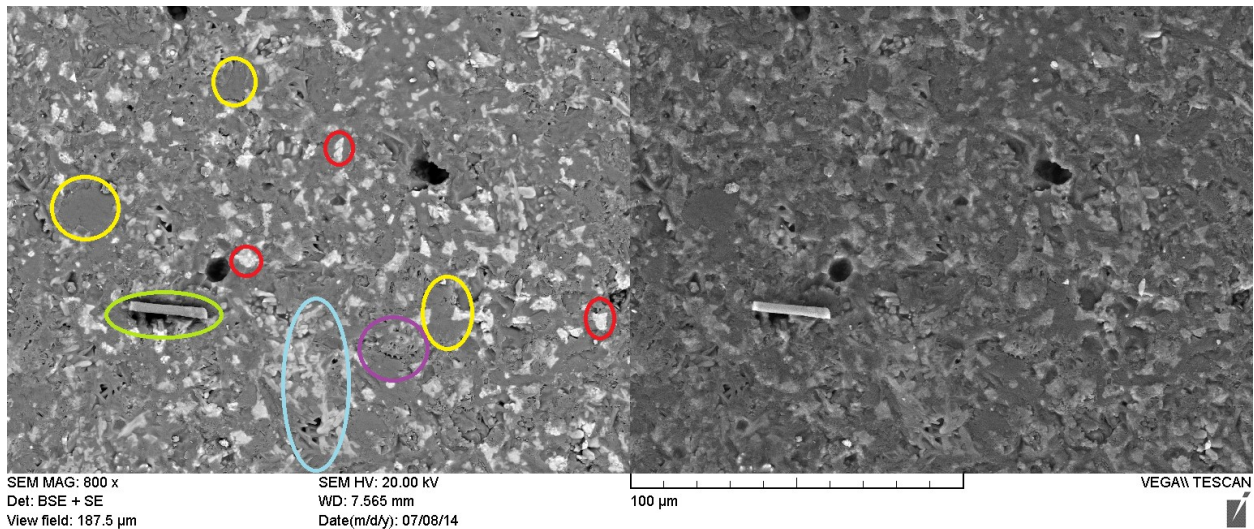


Figure 95: SEM image of ZTA_w after 100 thermal cycles. Purple circle highlights area of low density due to whiskers. Yellow circles highlight alumina grains and red circles highlight zirconia grains. The light blue circle shows a continuous zirconia grain which has formed between alumina grains. Light green circle shows whisker on the surface

Comparisons between Figures 92 and 93 show the effect of 10 cycles on densification. There is a slight increase in grain size shown as smaller grains are absorbed by larger grains; the overall grain growth is retarded by the pinning of alumina grain boundaries by zirconia grains, and the separation of zirconia grains by alumina grains as covered in the literature in section 2.3.3. Figure 94 shows a polished surface with mullite whiskers apparent. It can be seen that the whisker orientation is anisotropic which will lead

non-axis specific toughening. It can also be seen in that zirconia grains will take on an elongated shape when placed between two larger alumina grains. This highlights the restrictive role alumina grains play on the growth mechanics of zirconia. This is further underscored in Figure 95 where an abnormally long zirconia grain is highlighted by a light blue circle. This phenomenon is related to the level of sintering of the composite, it can be seen that as cycles increase and sintering increase, so too does the number of elongated zirconia grains. Also seen in Figure 95 is an area of lower density caused by a whisker network, this is highlighted by a purple circle.

XRD was used to examine the evolution of the crystal structure from initial powder, through sintering and thermal cycling. The XRD patterns of ZTA_w under all four conditions are overlaid in Figure 94 with the major crystal structures represented by large peaks marked.

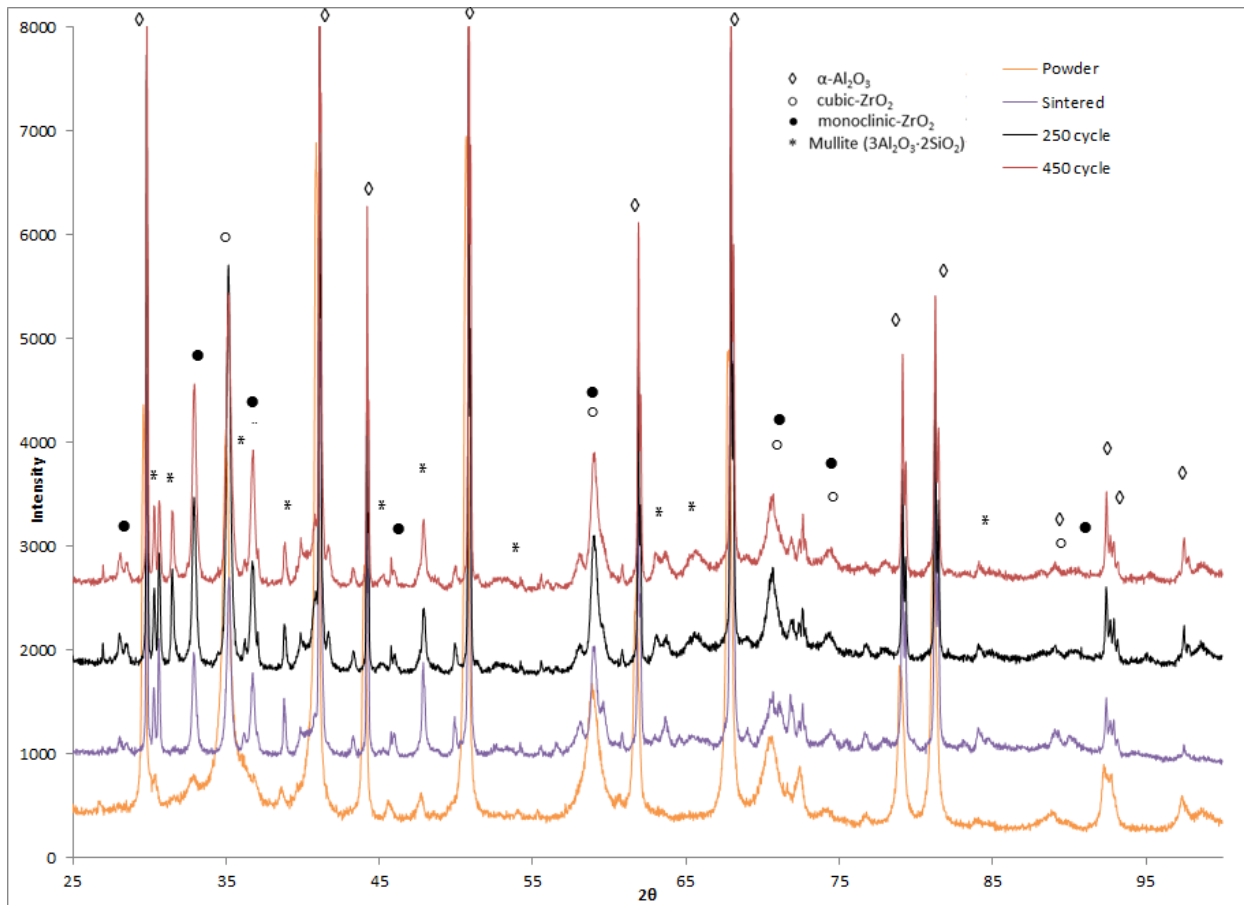


Figure 96: Progression of XRD scans for ZTA_w from powder to 450 thermal cycles

Most of the peaks are similar to Figure 76 from section 5.2.3. In Figure 97 the progression of the phases at $2\theta = 25-29^\circ$ is further examined. One trend to note is the slight increase of monoclinic zirconia after cycling. Tetragonal and cubic zirconia will transform into monoclinic zirconia. Mullite can also be seen to further develop through the intensifying of the mullite peaks during sintering, however, during thermal cycling it can be seen that the mullite content is somewhat reduced. This is especially highlighted in Figure 99. It can also be seen in Figure 97 that there is a slight growth of crystalline silica phase during thermal cycling of ZTA_w.

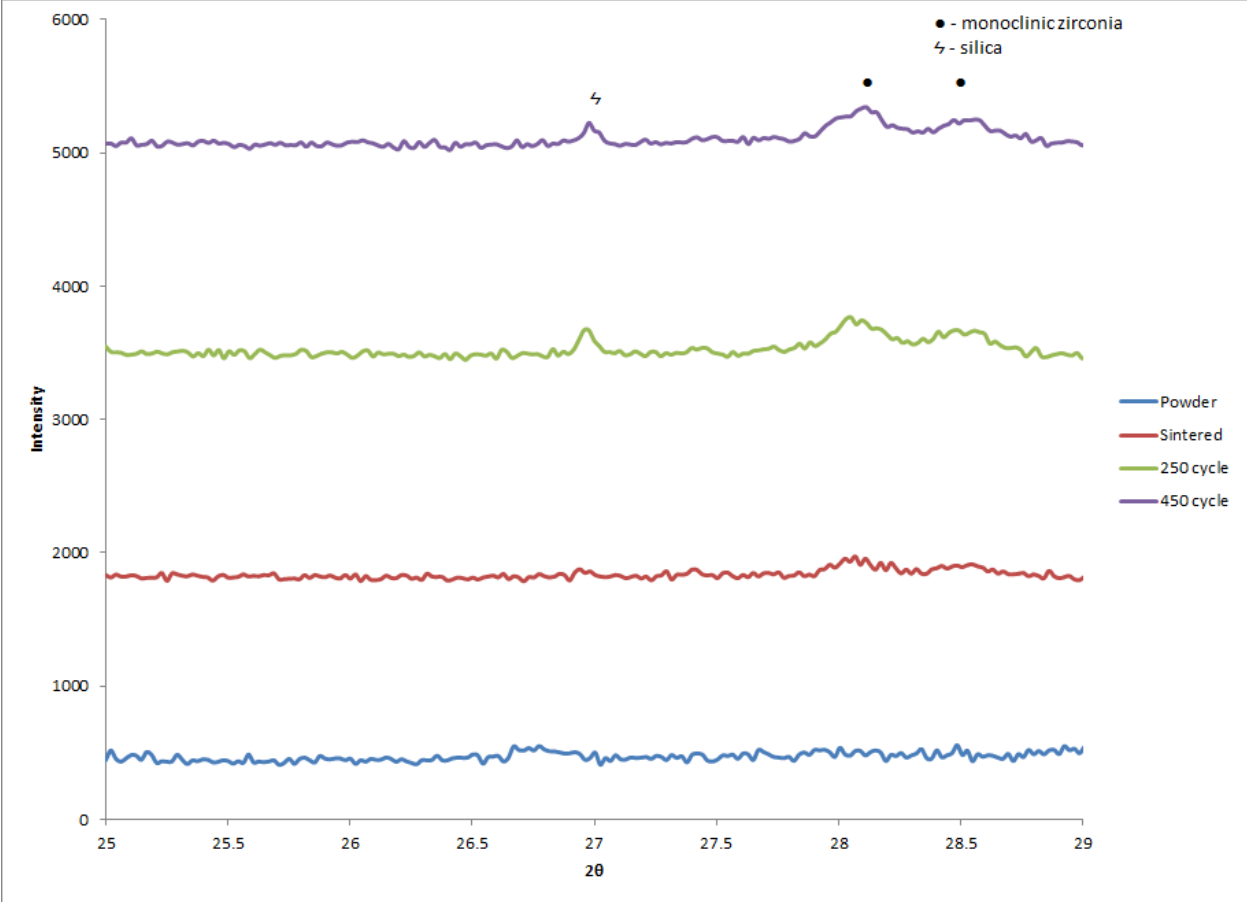


Figure 97: Progression of XRD scans for ZTA_w from powder to 450 thermal cycles with magnification of 25-29 region of 2θ

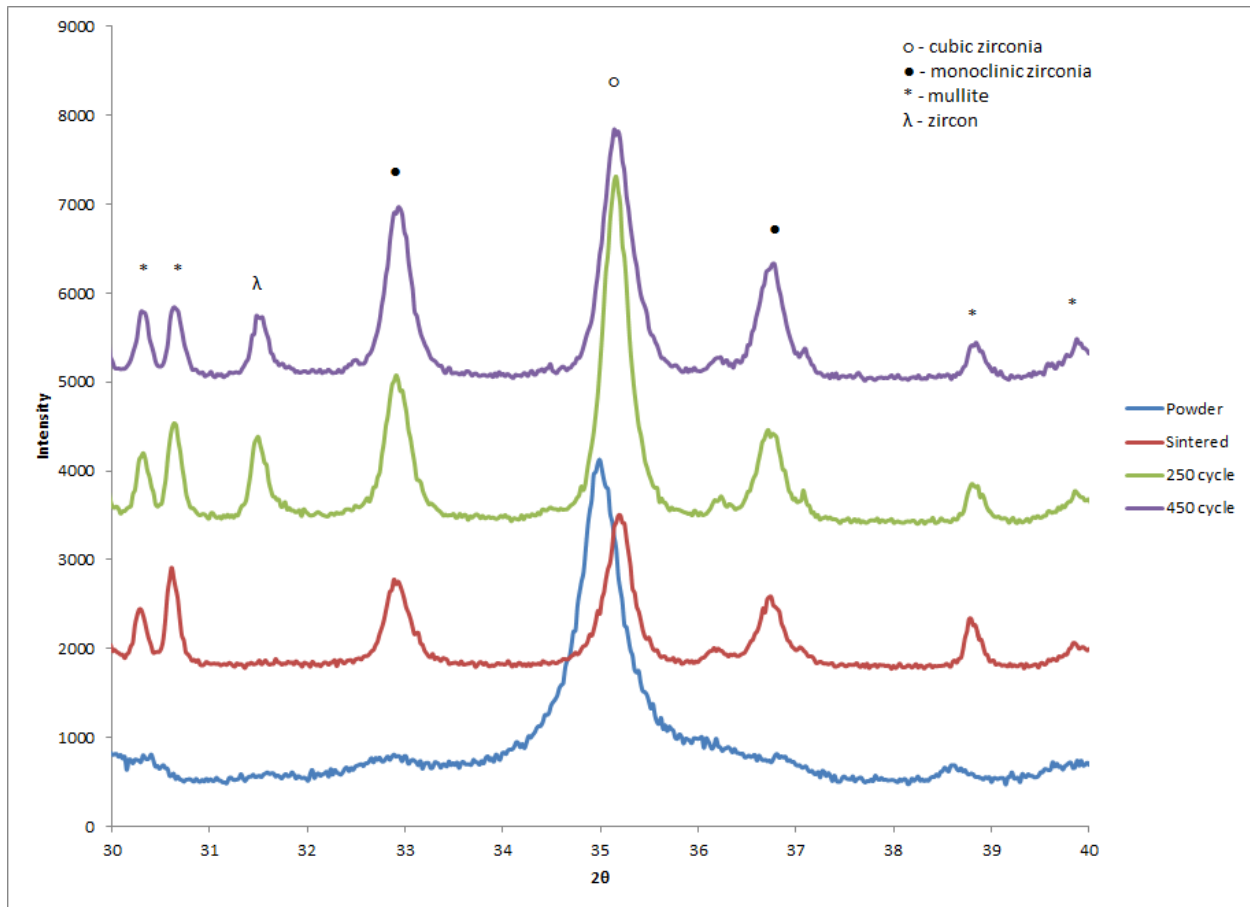


Figure 98: Progression of XRD scans for ZTA_w from powder to 450 thermal cycles with magnification of 30-40 region of 2θ

Figure 98 shows diffraction peaks at $2\theta = 30-40^\circ$; the formation of more monoclinic zirconia during sintering is evident, it also shows the formation of zircon (ZrSiO_4) at the $2\theta=31.5^\circ$. Another region of interest is from $69-74^\circ$. Figure 99 shows mullite peak at $2\theta=72^\circ$, which seems to fade away during thermal cycling. Judging from Figures 97 through 99, silica and zircon are forming during thermal cycling. While there may be some amorphous silica within the system from whisker production, XRD could not conclusively confirm its presence due to the amorphous nature.

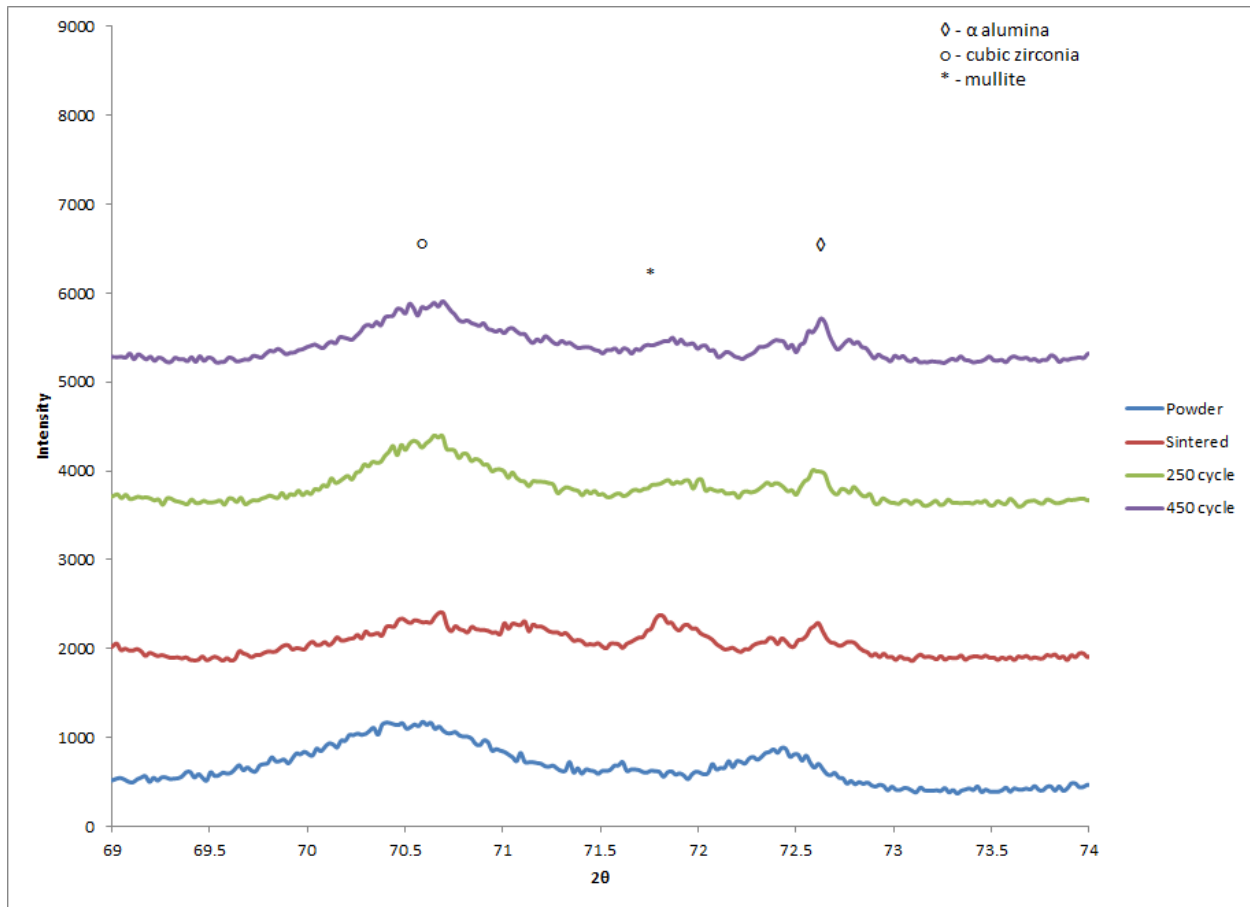


Figure 99: Progression of XRD scans for ZTA_w from powder to 450 thermal cycles with magnification of 69-74 region of 2θ

SEM images in Figure 100 provide a view of large diameter whiskers, which were apparent on all the cyclic samples. These whiskers are present throughout the samples but are visible when located on the surface. When examined at high magnification in Figure 101, it is clear that there is either a recrystallization or new phase formation on the larger diameter mullite whiskers which isn't present on the shorter whiskers shown in Figure 102.

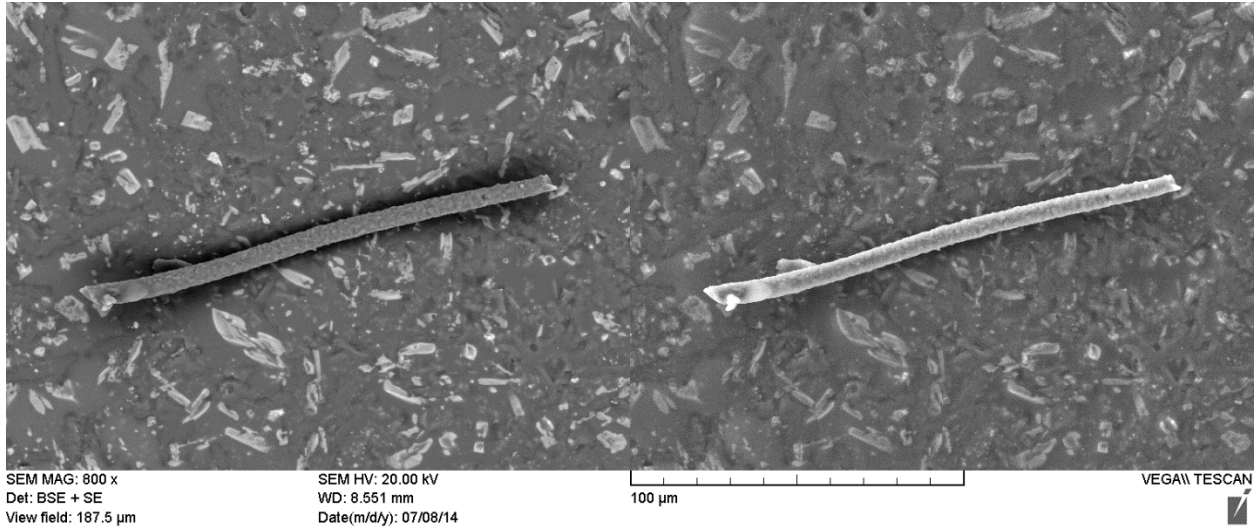


Figure 100: SEM image of ZTA_w after 50 cycles highlighting a large diameter exposed mullite whisker at 800 x magnification

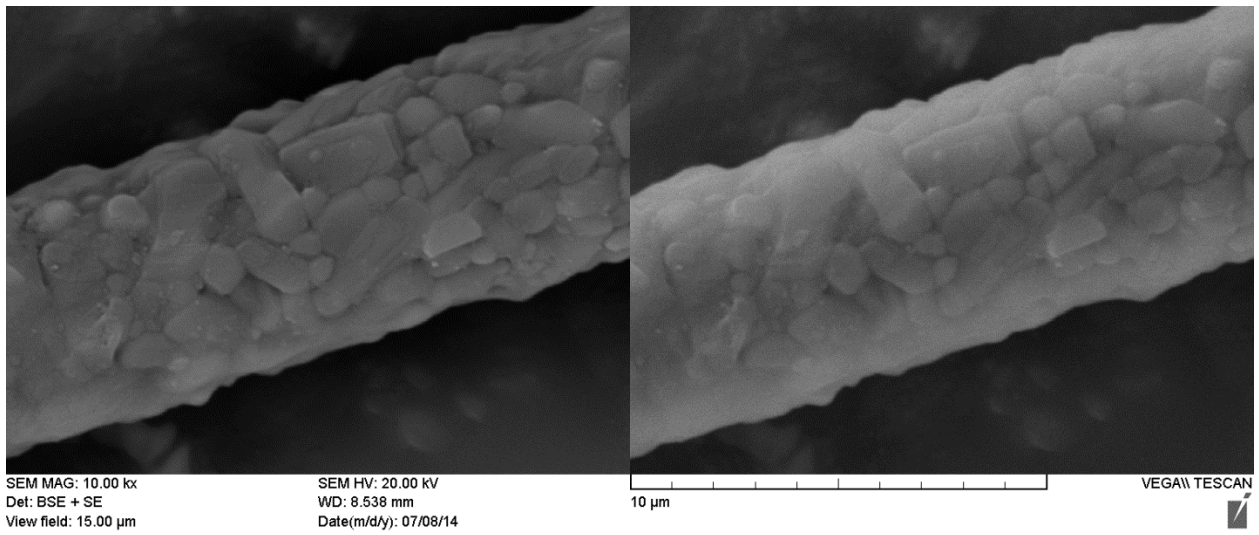


Figure 101: SEM image of ZTA_w after 50 cycles highlighting a large diameter exposed mullite whisker at 10 kx magnification

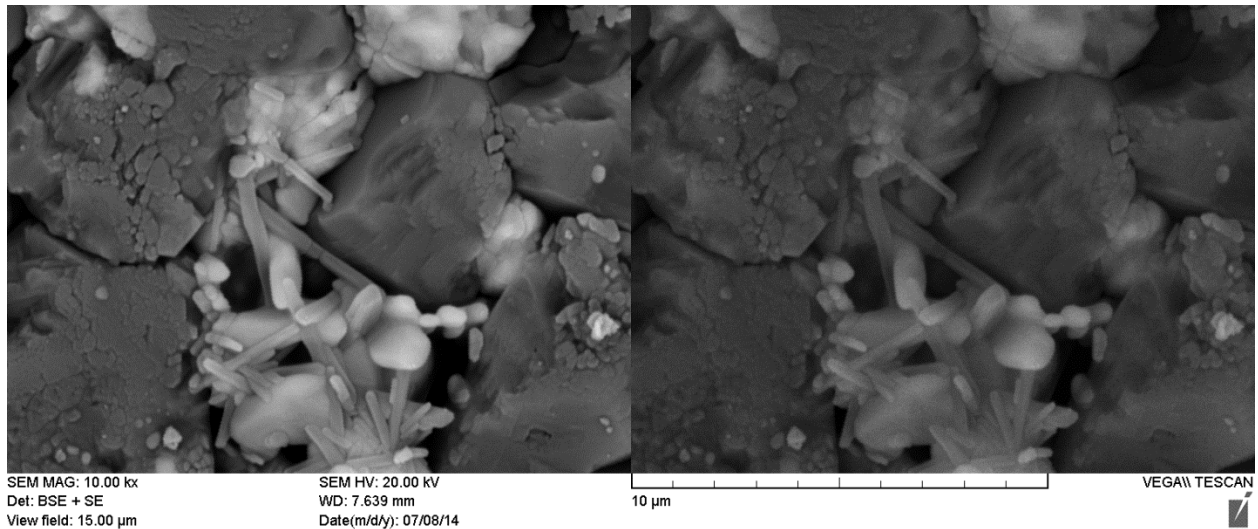


Figure 102: SEM image of ZTA_w after 200 cycles highlighting several small diameter exposed mullite whiskers at 10 kx magnification

Although mullite should be stable at 1200°C, excess silica content and environmental attack under the presence of moisture and alkaline contamination from the molten salt process may induce the formation of silica hydroxide [166] and subsequent evaporation. An EDS scan of whiskers before their addition to the composite has revealed some residual Na and C content. The carbon content is a very small percentage and could be due to carbon deposition by the electron beam.

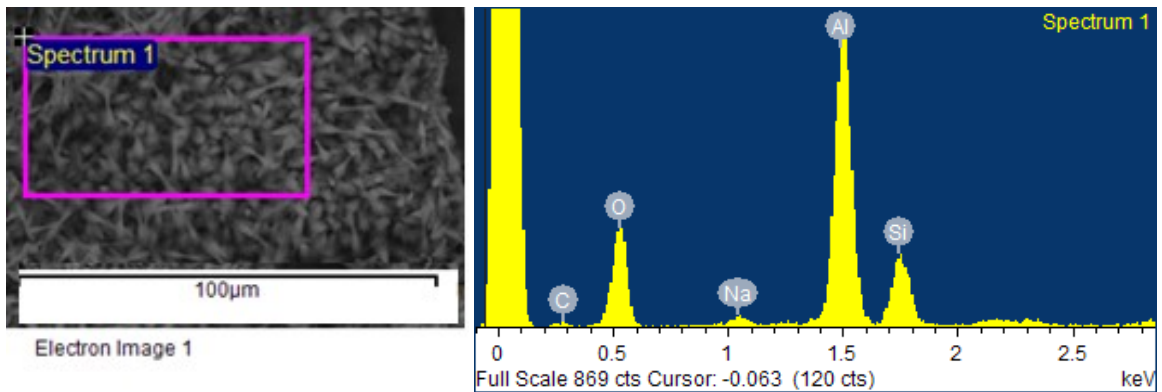
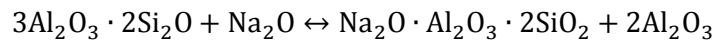
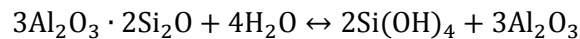


Figure 103: EDS scan of mullite whiskers prior to inclusion in ZTA composite

Neither elements were detected during the EDS analysis of ZTA_w samples; nevertheless, as can be seen in section 5.2.3, none of the large diameter whiskers were specifically scanned. Sodium content has been shown to react with mullite to form alumina and albite, shown in the reaction below. Albite has a lower melting point than alumina and also volatilizes with water vapor content [168].



Studies have also shown corrosion of polycrystalline mullite in water vapor at 1100°C through the following reaction [169].



This corrosion of mullite is concentrated along grain boundaries perpendicular to the c-axis, which would affect whisker bundles but should not harm single crystal whiskers. It is hard to determine whether Al₂O₃ content is increasing in the XRD scans due to the majority of the matrix being Al₂O₃. In a Co based XRD, albite primarily has peaks at 22°, 27° 2θ. This means that the detection of albite may be masked by silica. While Figure 101 shows the degradation of large mullite whiskers on the surface of the composite it is still unclear exactly which path this degradation is taking. Determining the path will be a subject of further work.

If Na contamination is responsible for the degradation of the mullite whiskers then a couple of methods could be employed to prevent this issue in future work. One method would include a second whisker washing stage after ultrasonic separation and filtering of the large whiskers, and a second would be to acquire the mullite whiskers from a new source such as thermal decomposition or an *in-situ* reaction. Vapor degradation of multigrain mullite whiskers won't cause issues beyond whiskers on the surface of the composite or connected to the surface through pore networks.

6.0 Conclusion

In this study, the process to manufacture a mullite whisker enhanced zirconia toughened alumina CMC material was developed. It was found that the ball milling method was effective in mixing the two powders (alumina and zirconia) and reducing the agglomeration of zirconia powders if employed for over 4 hours at 200 rpm. Ball milling did not; however, reduce the grain size of alumina particles in any significant way. The colloidal process using dextrin as a dispersion agent in acidic media was found to be able to suspend the ZTA particle mixture prior to filtering. Issues in the processing occurred during the drying stage after filtration and when PVA binder was added to the dry particles. Agglomerates which formed during these stages carried through to the green compact and became defects which reduced the mechanical properties of the ceramic. Further issues occurred using a vacuum furnace for sintering due to residual carbon remaining in the matrix. This was solved by including a longer organic burn-out stage in an oxygen atmosphere prior to sintering. Excessive porosity encountered in samples fired under the first sintering profile was reduced by increasing the holding time from 4 hours to 20 hours and removing the carbon contamination. Thermal cycling test shows that further sintering would also likely reduce the porosity.

ZTA_n and ZTA_w samples with final porosities of 13.2 % and 3.31 % were tested for room temperature and high temperature mechanical properties. ZTA_n reported a flexural strength of 61.71 ± 0.99 MPa at room temperature and 52.34 ± 15.72 MPa at 1200 °C, a fracture toughness of 5.02 ± 0.21 MPa · m^{1/2} (at room temperature) and a hardness of 10.73 GPa. ZTA_w reported a flexural strength of 135.76 ± 1.30 MPa at room temperature and 80.52 ± 13.18 MPa at 1200°C, a fracture toughness of 8.74 ± 0.24 MPa · m^{1/2} and a hardness of 11.99 GPa. The addition of whiskers to ZTA_n improved room temperature flexural strength by 120.0%, high temperature flexural strength by 53.8%, fracture toughness by 74.1%; but it had little

effect on the hardness. Although high temperature flexural strength was improved by the addition of whiskers, a greater loss of strength from room temperature to high temperature was seen in the whisker samples. It is hypothesized that this is caused by the degradation of large whiskers due to alkali contamination or vapor attack which is covered in more depth in section 5.4.2. ZTA_w samples were cycled between a 40 min at 1200°C and 20 min at room temperature for 450 cycles. A slight increase in normalised mass was noticed during initial cycles followed by a loss of mass between 10 and 400 cycles due to possible formation of volatile silicon hydroxide.

In conclusion, mullite whiskers have been shown to improve several key mechanical properties of a baseline zirconia toughened alumina matrix, although the current ZTA_w has not reached a comparable state to commercial fibre reinforced composites. Further research is required to improve both processing methods and raw material selections.

7.0 Future Work

In order to produce a composite with the desired properties specified in section 2.2 several issues with production will have to be addressed. The particle size and size distribution can be reduced by using a different material source. Further iterations of ZTA will utilize MKN-AL2O3-A100 alumina and MKN-3YSZ-040 zirconia particles from MKNano (Mississauga, Canada). Issues with agglomeration can be resolved by further sifting processes or through the use a gel casting techniques which incorporate PVA addition during slurry process. Whisker agglomeration issues can be resolved by further separation, filtering and washing steps. When these improvements have been implemented, further mechanical testing will take place.

For mechanical testing, a sample size of 30 samples per property will be tested to ensure an accurate statistical distribution for a weibull analysis. Reporting the characteristic strength and weibull modulus determined through a weibull analysis is important for both comparing this material to other ceramic systems as well as giving a better sense of the reliability of the system as described in section 2.2.7. A smaller load cell will be procured for the high temperature test frame to reduce the error in the reported load/strength. The smaller load cell will also allow for load control which is necessary for the creep testing method specified in section 4.4.2. The fracture toughness results will also be verified against pre-cracked beam tests to ensure localized effects are not influencing the toughness values. Finally, an acoustic method of determining elastic modulus specified in ASTM standard C1198-09 will be used to confirm the elastic modulus findings from the flexural test.

Although the mechanical properties may be compromised to certain extent, one of the advantages of using a discontinuous reinforcing phase is the ability to create small, complex near net shape products. A CAD impellor has been designed for a gel casting trail, which was subsequently 3-D printed and used as the negative of a mould (Figure 104). This impellor will serve as a pilot program to determine the

challenges of forming gel cast parts using ZTA_w. This work will also lead to opportunities to investigate the effect of whiskers on the gel casting process.

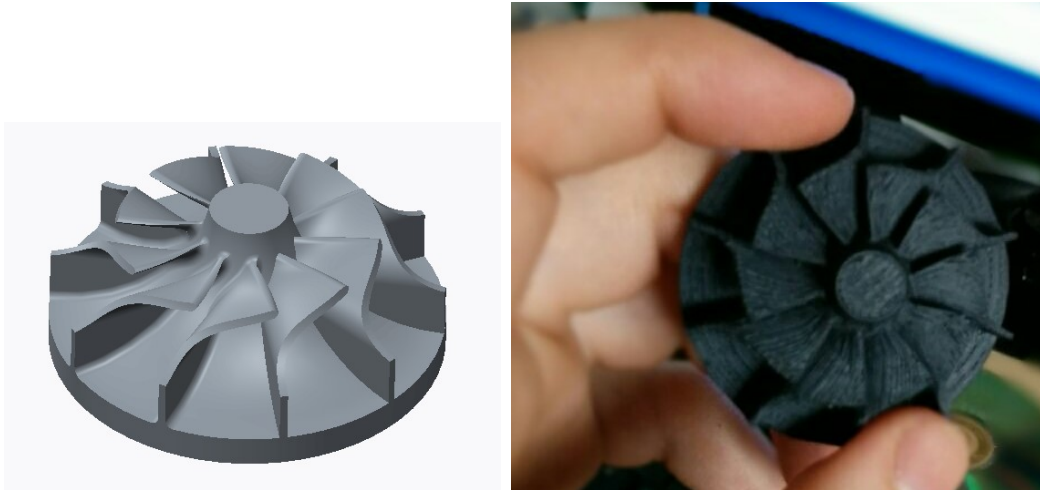


Figure 104: Image of CAD designed impellor and 3-D printed impellor negative

Another area of interest which will be investigated is the suitability of ZTA_w as a component of EBC for future SiC/SiC CFCCs or as insulating layer for the thermal barrier coating (TBC) system. As covered in section 2.3.1 non-oxide/non-oxide CMCs require EBCs to operate in aggressive gas turbine atmospheres. The current generation of EBCs incorporate mullite and zirconia but do not use whiskers as toughening agents. The advantage of using ZTA_w as part of the TBC system is the increased fracture strength which will lead to prolonged cyclic oxidation life. Further work will also be examined to see if a self-healing component can be included within the composite to improve reliability.

8.0 References

- [1] J. Conti, P. Holtberg and e. al., "International Energy Outlook 2011," Department of Energy, Washington D.C., 2011.
- [2] A. F. Ghoniem, "Needs, resources and climate change: Clean and efficient conversion technologies," *Progress in Energy and Combustion Science*, vol. 37, pp. 15-51, 2011.
- [3] M. Bolinger, R. Wiser and W. Golove, "Accounting for fuel price risk when comparing renewable to gas-fired generation: the role of forward natural gas prices," *Energy Policy*, vol. 34, no. 6, pp. 706-720, 2006.
- [4] "The Market for Gas Turbine Electrical Power Generation," Forcast International, Newtown CT, 2011.
- [5] M. P. Boyce, *Gas turbine engineering handbook*, Butterworth-Heinemann, 2012.
- [6] M. Konter and M. Thumann, "Materials and manufacturing of advanced industrial gas turbine components," *Journal of Materials Processing Technology*, vol. 117, pp. 386-390, 2001.
- [7] A. F. McLean and E. A. Fisher, "Brittle Materials Design, High Temperature Gas Turbine," Defense Advanced Research Projects Agency, Watertown Mass., 1981.
- [8] K. L. Luthra and G. S. Corman, *Melt Infiltrated (MI) SiC-SiC Composite for Turbine Applications*, Niskayuna NY: GE Global Research, 2005.
- [9] G. Corman and K. Luthra, "Silicon melt infiltrated ceramic composites (HiPerComp™)," in

Handbook of Ceramic Composites, Springer US, 2005, pp. 99-115.

- [10] J. Brennan, "Interfacial characterization of a slurry-cast melt-infiltrated SiC/SiC ceramic-matrix composite," *Acta Metallurgica*, vol. 48, pp. 4619-4628, 2000.
- [11] G. S. Corman and K. L. Luthra, "Melt infiltrated ceramic composites (HiPerComp) for gas turbine engine applications; Continuous Fiber Ceramic Composites Program; Phase II Final Report," Department of Energy, Washington D.C., 2006.
- [12] "Wikimedia Commons," The Wikimedia Foundation, 2013. [Online]. Available: <http://commons.wikimedia.org>. [Accessed 2013].
- [13] F. Masuyama, "History of Power Plants and Progress in Heat Resistant Steels," *ISIJ International*, vol. 41, no. 6, pp. 612-625, 2001.
- [14] P. R. Sahm and M. O. Speidel, *High-Temperature Materials in Gas Turbines*, Elsevier, 1974.
- [15] Protasova, "Some features of monocrystalline turbine blade regeneration after high temperature treatment," *Aircraft Production Technology*, vol. 1, pp. 58-63, 2011.
- [16] P. Caron and T. Khan, "Evolution of Ni-based superalloys for single crystal gas turbine blade applications," *Aerospace Science Technology*, vol. 3, pp. 513-523, 1999.
- [17] M. van Roode, "Ceramic Gas Turbine Development: Need for a 10 Year Plan," *Journal of engineering for gas turbines and power*, vol. 132, no. 1, 2010.
- [18] H.-C. Liu, S. Kang, F. Prinz and J. Stampfl, "Fabrication of ceramic components for micro gas turbine engines," Rapid Prototyping Lab, Stanford University, Stanford CA.

- [19] Y.-M. Chiang, D. Birnie and W. Kingery, *Physical Ceramics: Principles for Ceramic Science and Engineering*, John Wiley & Sons Inc., 1997.
- [20] H. Ohnabe, S. Masaki, M. Onozuka, K. Miyahara and T. Sasa, "Potential application of ceramic matrix composites to aero-engine components," *Composites: Part A*, vol. 30, pp. 489-496, 1999.
- [21] R. Raj, "Fundamental Research in Structural Ceramics for Service Near 2000 C," *Journal of the American Ceramics Society*, vol. 76, no. 9, pp. 2147-2174, 1993.
- [22] Y. Ji and J. Yeomans, "Processing and mechanical properties of Al₂O₃ 5vol.% Cr nanocomposites," *Journal of European Ceramics Society*, vol. 22, no. 12, pp. 1927-1936, 2002.
- [23] K. Niihara, A. Nakahira and T. Sekino, "New nanocomposite structural ceramics," in *MRS Proceedings*, 1992.
- [24] S. Oh, T. Sekino and K. Niihara, "Fabrication and mechanical properties of 5 vol% copper dispersed alumina nanocomposite," *Journal of the European Ceramic Society*, vol. 18, no. 1, pp. 31-37, 1998.
- [25] C. Anya, "Microstructural nature of strengthening and toughening in Al₂O₃-SiC (p) nanocomposites," *Journal of materials science*, vol. 34, no. 22, pp. 5557-5567, 1999.
- [26] P. Becher and G. Wei, "Toughening Behavior in Sic-Whisker-Reinforced Alumina," *Journal of the American Ceramic Society*, vol. 67, no. 12, pp. C-267, 1984.
- [27] P. Christel, A. Meunier, M. Heller, J. Torre and C. Peille, "Mechanical properties and short-term in-vivo evaluation of yttrium-oxide-partially-stabilized zirconia," *Journal of Biomedical Materials Research*, vol. 23, pp. 45-61, 1989.

- [28] G. Orange, G. Fantozzi, F. Cambier, C. Leblud, M. R. Anseau and A. Leriche, "High temperature mechanical properties of reaction-sintered mullite/zirconia and mullite/alumina/zirconia composites," *Journal of Materials Science*, vol. 20, pp. 2533-2540, 1985.
- [29] Mah, Tai-II and K. Mazdiyasi, "Mechanical properties of mullite," *Journal of the American Ceramic Society*, vol. 66, no. 10, pp. 699-703, 1983.
- [30] Y. Kobayashi, E. Matsuo and K. Kato, "Hot-Gas Spin Testing of Ceramic Radial Turbine Rotor at TIT around 1250C," *SAE Technical Paper*, 1988.
- [31] Y. Kobayashi, E. Matsuo, T. Inagaki and T. Ozawa, "Hot-Gas Spin Testing of Rotor at TIT 1400 C," *SAE technical Paper*, 1991.
- [32] S. Ribeiro and K. Strecker, "Si₃N₄ ceramics sintered with Y₂O₃/SiO₂ and R₂O₃ (ss)/SiO₂: a comparative study of the processing and properties," *Materials Research*, vol. 7, no. 3, pp. 377-383, 2004.
- [33] R. Jurf and S. Butner, "Advances in oxide-oxide CMC," *Transactions-American Society of mechanical engineers journal of engineering for gas turbines and power*, vol. 122, no. 2, pp. 202-205, 2000.
- [34] E. Mouchon and P. Colomban, "Oxide Ceramic matrix/oxide fibre woven fabric composites exhibiting dissipative fracture behaviour," *Composites*, vol. 26, pp. 175-182, 1995.
- [35] A. T. Zehnder, *Fracture mechanics*, Dordrecht, New York: Springer, 2012.
- [36] G. Zhan, J. Kuntz, J. Wan and A. Mukherjee, "Single-wall carbon nanotubes as attractive

- toughening agents in alumina-based nanocomposites," *Nature Materials*, vol. 2, pp. 38-42, 2003.
- [37] X. Liu, Q. Huang, X. Ge and L. Huang, "Microstructure and mechanical properties of silicon nitride ceramics prepared by pressureless sintering with MgO-Al₂O₃-SiO₂ as sintering additive," *Journal of the European Ceramic Society*, vol. 25, no. 14, pp. 3353-3359, 2005.
- [38] Y. Zheng, K. Knowles, J. Vieira, A. Lopes and F. Oliveira, "Microstructure, toughness and flexural strength of self-reinforced silicon nitride ceramics doped with yttrium oxide and ytterbium oxide," *Journal of microscopy*, vol. 201, no. 2, pp. 238-249, 2001.
- [39] M. Bocanegra-Bernal and B. Matovic, "Mechanical properties of silicon nitride-based ceramics and its use in structural applications at high temperatures," *Materials Science and Engineering A*, vol. 527, pp. 1314-1338, 2010.
- [40] G. Lai, High-temperature corrosion and materials applications, ASM International, 2007.
- [41] G. Holcomb and e. al., "Steam turbine materials and corrosion," in *Proceedings of the 21st Annual Conference on Fossil Energy Materials*, 2007.
- [42] S. Nair and K. Jakus, High Temperature Mechanical Behavior of Ceramic Composites, Elsevier, 1995.
- [43] R. Miller, *MECH 5609: Microstructure and Properties of Engineering Materials Lecture*, Ottawa: Carleton University, 2012.
- [44] K. K. Chawla, Composite Materials, New York: Springer New York, 2012.
- [45] Q. Tai and A. Mocellin, "Review: High temperature deformation of Al₂O₃-based ceramic particle or

- whisker composites," *Ceramics International*, vol. 25, pp. 395-408, 1999.
- [46] K. Wakashima and F. Liu, "Unsteady diffusional creep of dual-phase material," *Scripta Materialia*, vol. 36, no. 10, pp. 1081-1087, 1997.
- [47] C. Bathias and A. Pineau, *Fatigue of materials and structures fundamentals*, John Wiley, 2010.
- [48] A. Ural, V. Krishnan and K. Papoulia, "A cohesive zone model for fatigue crack growth allowing for crack retardation," *International Journal of Solids and Structures*, vol. 46, pp. 2453-2462, 2009.
- [49] I. Low, *Ceramic Matrix Composites - Microstructure, Properties and Applications*, Woodhead Publishing, 2006.
- [50] H. Majidian, T. Ebadzadeh and E. Salahi, "Effect of SiC additions on microstructure, mechanical properties and thermal shock behaviour of alumina-mullite-zirconia composites," *Materials Science and Engineering A*, vol. 530, pp. 585-590, 2011.
- [51] O. Vardar and I. Finnie, "An analysis of the Brazilian disk fracture test using the Weibull probabilistic treatment of brittle strength," *International Journal of Fracture*, vol. 11, no. 3, pp. 495-508, 1975.
- [52] W. D. Kingery, "Metal-Ceramic Interactions: I, Factors Affecting Fabrication and Properties of Cermet Bodies," *Journal of the American Ceramic Society*, vol. 36, no. 11, pp. 362-365, 1953.
- [53] M. Randall, S. Pavan and J. P. Seong, "Review: liquid phase sintering," *Journal of materials science*, vol. 44, no. 1, pp. 1-39, 2009.
- [54] J. Wang and R. Stevens, "Review: Zirconia-toughened alumina (ZTA) ceramics," *Journal of*

Materials Science, vol. 24, pp. 3421-3440, 1989.

- [55] B.-H. Yu and D. Chen, "Predictions of pressure-induced structural transition, mechanical and thermodynamic properties of alpha and beta Si₃N₄ ceramics: ab initio and quasi harmonic Debye modeling," *Chinese Physics B*, vol. 21, no. 6, 2012.
- [56] K. Shimoda, T. Hinoki, H. Kishimoto and A. Kohyama, "Enhanced high-temperature performances of SiC/SiC composites by high densification and crystalline structure".
- [57] S. M. Goushegir, P. O. Guglielmi, J. G. P. da Silva, M. P. Hablitzel, D. Hotza, H. A. Al-Qureshi and R. Janssen, "Fiber-Matrix Compatibility in an All-Oxide Ceramic Composite with RBAO Matrix," *Journal of the American Ceramic Society*, vol. 95, no. 1, pp. 159-164, 2012.
- [58] S. Mall and B. Boyer, "Cyclic and sustained loading behaviors of oxide/oxide Nextel 720/alumina composite with double edge sharp notch," *Composites: Part A*, vol. 43, pp. 1153-1159, 2012.
- [59] O. Jadaan and N. Nemethm, "Transient reliability of ceramic structures," *Fatigue Fracture Engineering for Material Structures*, vol. 24, pp. 475-487, 2001.
- [60] A. Bunsell, "Oxide Fibres," in *Handbook of Ceramic Composites*, Boston, Kluwer Academic Publishers, 2005, pp. 3-33.
- [61] P. Mallik, *Fiber-Reinforced Composites* 3rd edition, CRC Press, 2007.
- [62] F. Deleglise, M. Berger, D. Jeulin and A. Bunsell, "Microstructure stability and room temperature mechanical properties of the Nextel 720 fibre," *Journal of the European Ceramic Society*, vol. 21, no. 5, pp. 569-580, 2001.

- [63] M. Ruggles-Wrenn and C. Genelin, "Creep of Nextel 720/alumina-mullite ceramic composite at 1200 C in air, argon, and steam," *Composites Science and Technology*, vol. 69, pp. 663-669, 2009.
- [64] C. J. Armani, "Creep Performance of Oxide Ceramic Fiber Materials at Elevated Temperature in Air and in Steam," Air Force Institute of Technology, Wright-Patterson Air Force Base, Ohio, 2011.
- [65] J. Mehrman, M. Ruggles-Wrenn and S. Baek, "Influence of hold times on the elevated-temperature fatigue behavior of an oxide-oxide ceramic composite in air and in steam environment," *Composites Science and Technology*, vol. 67, pp. 1425-1438, 2007.
- [66] S. Farmer, A. Sayir, P. Dickerson and S. Draper, "Microstructure Stability and Strength Retention in Directionally Solidified Al₂O₃-YAG Eutectic Fibres," *Ceramic Engineering and Science Proceedings*, Vols. Sept.-Oct., pp. 969-976, 1995.
- [67] M. Koopman, S. Duncan, K. Chawla and C. Coffin, "Processing and characterization of barium zirconate coated alumina fibers/alumina matrix composites," *Composites Part A*, vol. 32, pp. 1039-1044, 2001.
- [68] M. Holmquist, R. Lundberg, O. Sudre, A. Razzell, L. Molliex, J. Benoit and J. Adlerborn, "Alumina/alumina composite with a porous zirconia interphase - Processing, properties and component testing," *Journal of the European Ceramic Society*, vol. 20, pp. 599-606, 2000.
- [69] K. Keller, G. Jefferson and R. Kerans, "Oxide-Oxide composites," in *Handbook of Ceramic Composites*, Boston, Kluwer Academic Publishers, 2005, pp. 377-423.
- [70] R. Goettler, S. Sambasivan, V. Dravid and S. Kim, "Interfaces in Oxide Fiber-Oxide Matrix Ceramic Composites," in *Computer Aided Design in High Temperature Materials*, Oxford University Press,

1999, pp. 333-349.

- [71] K. Keller, T.-I. Mah, T. Parthasarathy, E. Boakye, M. P. and M. Cinibulk, "Effectiveness of monazite coatings in oxide/oxide composites after long-term exposure at high temperature," *Journal of the American Ceramic Society*, vol. 86, no. 2, pp. 325-332, 2003.
- [72] M. Lewis, A. Tye, E. Butler and P. Doleman, "Oxide CMCs: interphase synthesis and novel fibre development," *Journal of the European Ceramic Society*, vol. 20, pp. 639-644, 2000.
- [73] A. Rudinger, "Die Entwicklung oxidkeramischer Faserverbundwerkstoffe am Fraunhofer ISC/Zentrum HTL in Zusammenarbeit mit WEC Pritzkow Spezialkeramik," *Keramic Zentrum*, vol. 65, pp. 3-5, 2013.
- [74] W. S. Westby, S. Kooner, P. M. Farries, P. Boother and A. Shatwell, "Processing of Nextel 720/Mullite Composition Composite Using Electrophoretic Deposition," *Journal of Materials Science*, vol. 34, pp. 5021-5031, 1999.
- [75] M. Schmucker and H. Schnieder, "WHIPOX all oxide ceramic matrix composites," in *Handbook of Ceramic Composites*, Boston, Kluwer Academic Publishers, 2005, pp. 423-437.
- [76] M. Halbig, M. Jaskowiak, J. Kiser and D. Zhu, "Evaluation of Ceramic Matrix Composite Technology for Aircraft Turbine Engine Applications," NASA Glenn Research Center, Cleveland, OH, 2011.
- [77] S. Hackemann, F. Flucht and W. Braue, "Creep investigations of alumina-based all-oxide ceramic matrix composites," *Composites: Part A*, vol. 41, pp. 1768-1776, 2010.
- [78] M. Parlier, M.-H. Ritti and A. Jankowiak, "Potential and Perspectives for Oxide/Oxide Composites,"

Aerospace Lab Journal, vol. 1, no. 12, pp. AL03-09, 2011.

- [79] J. DiCarlo and H.-M. Yun, "Non-oxide (Silicon Carbide) Fibers," in *Handbook of Ceramic Composites*, Boston, Kluwer Academic Publishers, 2005, pp. 33-53.
- [80] J. Lamon, "Chemical Vapor Infiltrated SiC/SiC Composites (CVI SiC/SiC)," in *Handbook of Ceramic Composites*, Boston, Kluwer Academic Publishers, 2005, pp. 55-77.
- [81] J. DiCarlo, H.-M. Yun, G. Morscher and R. Bhatt, "SiC/SiC Composites for 1200 C and Above," in *Handbook of Ceramic Composites*, Boston, Kluwer Academic Publishers, 2005, pp. 77-99.
- [82] A. Balazs, "Modeling Self-healing Materials," *Materials Today*, vol. 10, no. 9, pp. 18-23, 2007.
- [83] C. Cluzel, E. Baranger, P. Ladeveze and A. Mouret, "Mechanical behaviour and lifetime modelling of self-healing ceramic-matrix composites subjected to thermomechanical loading in air," *Composites: Part A*, vol. 40, pp. 976-984, 2009.
- [84] M. Ruggles-Wrenn and M. Pope, "Creep Behavior in Interlaminar Shear of a SiC/SiC Ceramic Composite with Self-healing Matrix," *Applied Composite Materials*, vol. 21, pp. 213-225, 2014.
- [85] L. Quemard, F. Rebillat, A. Guette, H. Tawil and C. Louchet-Pouillierie, "Self-healing mechanisms of a SiC fiber reinforced multilayered ceramic matrix composite in high pressure steam environments," *Journal of the European Ceramic Society*, vol. 27, pp. 2085-2094, 2007.
- [86] K. Lee, D. Fox, J. Eldridge, D. Zhu, R. Raymond, N. Bansal and R. Miller, "Upper Temperature Limit of Environmental Barrier Coatings Based on Mullite and BSAS," *Journal of the American Ceramic Society*, vol. 86, no. 8, pp. 1299-1306, 2003.

- [87] S. Ramasamy, S. Tewari, K. Lee, R. Bhatt and D. Fox, "Slurry based multilayer environmental barrier coatings for silicon carbide and silicon nitride ceramics - I. Processing," *Surface and Coatings Technology*, vol. 205, pp. 258-265, 2010.
- [88] S. Rmasamy, S. Tewari, K. Lee, R. Bhatt and D. Fox, "Slurry based multilayer environmental barrier coatings for silicon carbide and silicon nitride ceramics - II. Oxidation resistance," *Surface and Coatings Technology*, vol. 205, pp. 266-270, 2010.
- [89] H. Kim, M. Chen, Q. Yang and T. Troczynski, "Sol-gel alumina environmental barrier coatings for SiC grit," *Materials Science and Engineering A*, vol. 420, pp. 150-154, 2006.
- [90] K. Chawla, *Ceramic Matrix Composites 2nd Ed.*, Boston: Kluwer Academic, 2003.
- [91] R. Naslain, "Desing, preparation and properties of non-oxide CMCs for application in engines and nuclear reactors: an overview," *Composites Science and Technology*, vol. 64, pp. 155-170, 2004.
- [92] J. She, T. Inoue and K. Ueno, "Fracture behavior and mechanical properties of multilayered alumina-based composites with different layer thicknesses," *Journal of Materials Science Letters*, vol. 19, pp. 45-47, 2000.
- [93] E. Ewais, D. Besisa, Z. Zaki and A. Kandil, "Tailoring of functionally graded zirconia-mullite/alumina ceramics," *Journal of the European Ceramic Society*, vol. 32, pp. 1561-1573, 2012.
- [94] H. M. Chan, "Layered Ceramics: Processing and Mechanical Behavior," *Annual Review of Materials Science*, vol. 27, no. 1, pp. 249-282, 1997.
- [95] L. Sun, A. Sneller and P. Kwon, "Powder Selection in Co-Sintering Multi-Layered Functionally Graded Materials Based on the Densification Kinetics Curves," *Journal of Composite Materials*, vol.

43, no. 5, pp. 469-482, 2009.

- [96] M. Borba, M. de Araujo, E. de Lima, H. Yoshimura, P. Cesar, J. Griggs and A. Bona, "Flexural strength and failure modes of layered ceramic structures," *Dental Materials*, vol. 27, no. 12, pp. 1259-1266, 2011.
- [97] M. Hebsur, "MoSi₂-Based Composites," in *Handbook of Ceramic Composites*, Boston, Kluwer Academic Publishers, 2005, pp. 173-197.
- [98] S. Lohfeld and M. Schutze, "Oxidation behaviour of particle reinforced MoSi₂ composites at temperatures up to 1700 C Part 1: Literature Review," *Materials and Corrosion*, vol. 56, no. 2, pp. 93-97, 2005.
- [99] C. McKamey, P. Tortorelli, J. DeVan and C. Carmicheal, "A study of pest oxidation in polycrystalline MoSi₂," *Journal of Materials Research*, vol. 7, no. 10, pp. 2747-2755, 1992.
- [100] M. Bengisu, "Whisker Toughening of Ceramics: Toughening Mechanisms, Fabrication, and Composite Properties," *Annual Review of Materials Science*, vol. 24, pp. 83-124, 1994.
- [101] M. Bohmer and E. Almond, "Mechanical Properties and Wear Resistance of a Whisker-reinforced Zirconia-toughened Alumina," *Materials Science and Engineering*, vol. 105, pp. 105-116, 1988.
- [102] R. Bradley, D. Clark, D. Larsen and J. Stiegler, in *Whisker and Fiber Toughened Ceramics*, Metals Park, OH, ASM International, 1989, pp. 105-108.
- [103] J. R. Porter, "Dispersion Processing of Creep Resistant Whisker-Reinforced Ceramic Matrix Composites," *Materials Science and Engineering*, vol. A107, pp. 127-132, 1989.

- [104] W. Hillig, "Prospects for Ultrahigh Temperature Ceramic Composite," in *Tailoring Multiphase and Composite Ceramics*, New York, Plenum, 1986, pp. 697-712.
- [105] R. Munro, "Evaluated Material Properties for a Sintered alpha-Alumina," *Journal of the American Ceramic Society*, vol. 80, no. 8, pp. 1919-1928, 1997.
- [106] F. Sommer, R. Landfried, F. Kern and R. Gadow, "Mechanical properties of zirconia toughened alumina with 10-24 vol.% 1.5 mol% Y-TZP reinforcement," *Journal of the European Ceramic Society*, vol. 32, no. 15, pp. 3905-3910, 2012.
- [107] M.-T. Weng, W.-C. J. Wei and C.-Y. Huang, "Influence of 3Y-TZP on Microstructure and Mechanical Properties of Al₂O₃-based Composites," *Key Engineering Materials*, vol. 353, no. 358, pp. 1540-1543, 2007.
- [108] M. V. Swain and L. Rose, "Strength Limitations of Transformation Toughened Zirconia Alloys," *Journal of the American Ceramic Society*, vol. 69, no. 7, pp. 511-518, 1986.
- [109] N. Claussen, "Fracture Toughness with an Unstabilized ZrO₂ Dispersed Phase," *Journal of the American Ceramic Society*, vol. 59, no. 1, pp. 49-51, 1976.
- [110] J. Wang and R. Stevens, "Toughening mechanisms in duplex alumina-zirconia ceramics," in *British Ceramics Society*, Stoke-on-Trent, 1987.
- [111] K. Okada and N. Otuska, "Synthesis of Mullite Whiskers and Their Application in Composites," *Journal of the American Ceramics Society*, vol. 74, no. 10, pp. 2414-2418, 1991.
- [112] B. Meng and P. Jinhui, "Effects of in situ synthesized mullite whiskers on flexural strength and fracture toughness of corundum-mullite refractory materials," *Ceramics International*, vol. 39, no.

2, pp. 1525-1531, 2013.

- [113] J. R. Moyer and N. N. Hughes, "A Catalytic Process for Mullite Whiskers," *Journal of the American Ceramics Society*, vol. 77, no. 4, pp. 1083-1086, 1994.
- [114] M. Bronikowski, P. Willis, D. Colbert, K. Smith and R. Smalley, "Gas-phase production of carbon single-walled nanotubes from carbon monoxide via the HiPco process: A parametric study," *Journal of the American Vacuum Society*, vol. 19, no. 4, pp. 1800-1805, 2001.
- [115] J.-P. Salvetat, G. Briggs, J.-M. Bonard, R. Bacsá, A. Kulik, T. Stockli, N. Burnham and L. Forro, "Elastic and Shear Moduli of Single-Walled Carbon Nanotube Ropes," *Physical Review Letters*, vol. 82, no. 5, pp. 944-947, 1999.
- [116] J. Petrovic, J. Milewski, D. Rohr and F. Gac, "Tensile mechanical properties of SiC whiskers," *Journal of Materials Science*, vol. 20, pp. 1167-1177, 1985.
- [117] R. Carvalho, A. Fernandes, F. Oliveira, E. Alves, N. Franco, C. Louro, R. Silva and F. Costa, "Single and polycrystalline mullite fibres grown by laser floating zone technique," *Journal of the European Ceramic Society*, vol. 30, pp. 3311-3318, 2010.
- [118] L. Zhuang, "Micromechanical Stresses in Sapphire Whisker and Alumina Reinforced Mullite and Garnet Ceramic Matrix Composites," *Journal of the European Ceramic Society*, vol. 9, pp. 143-152, 1992.
- [119] S. Jagota and R. Raj, "Producing alpha-alumina whiskers". USA Patent US4806198 A, 21 Feb 1989.
- [120] J. Shackelford and R. Doremus, *Ceramic and Glass Materials: Structure, Properties and Processing*,

Springer, 2008.

- [121] S. Freimann and S. Rahman, "Refinement of the real structures of 2:1 and 3:2 mullite," *Journal of the European Ceramic Society*, vol. 21, pp. 2453-2461, 2001.
- [122] C. Bergeron and S. Risbud, *Introduction to Phase Equilibria in Ceramics*, Columbus, OH: American Ceramic Society, 1984.
- [123] C. Paulmann, "Study of oxygen vacancy ordering in mullite at high temperature," *Phase Trans*, vol. 59, pp. 77-90, 1996.
- [124] J. A. Lewis, "Colloidal Processing of Ceramics," *Journal of the American Ceramic Society*, vol. 83, pp. 2341-2359, 2000.
- [125] M. S. Olhero, I. Ganesh, P. M. C. Torres, F. J. Alves and J. M. Ferreira, "Aqueous Colloidal Processing of ZTA Composites," *Journal of the American Ceramic Society*, vol. 92, no. 1, pp. 9-16, 2009.
- [126] A. Safinajafabadi, R. Sarraf-Mamoory and Z. Karimi, "Effect of organic dispersants on structural and mechanical properties of Al₂O₃/ZrO₂ composites," *Materials Research Bulletin*, vol. 47, pp. 4210-4215, 2012.
- [127] H. Wakily, M. Mehrali and H. S. C. Metselaar, "Preparation of Homogenous Dense Composite of Zirconia and Alumina (ZTA) using Colloidal Filtration," *World Academy of Science, Engineering and Technology*, vol. 46, pp. 140-145, 2010.
- [128] F. Chabert, D. E. Dunstan and G. V. Franks, "Cross-linked Polyvinyl Alcohol as a Binder for Gelcasting and Green Machining," *Journal of the American Ceramics Society*, vol. 91, no. 10, pp.

3138-3146, 2008.

- [129] P. Zhang, J. Liu, H. Du, Z. Li, S. Li and C. Chen, "Influence of silica sources on morphology of mullite whiskers in Na₂SO₄ flux," *Journal of Alloys and Compounds*, vol. 484, pp. 580-584, 2009.
- [130] P. Zhang, J. Liu, H. Du, Z. Li, S. Li, S. Li and R. Xu, "Molten salt synthesis of mullite whiskers from various alumina precursors," *Journal of Alloys and Compounds*, vol. 491, pp. 447-451, 2010.
- [131] W. Wang, H. Li, K. Lai and K. Du, "Preparation and characterization of mullite whiskers from silica fume by using a low temperature molten salt method," *Journal of Alloys and Compounds*, vol. 510, pp. 92-96, 2012.
- [132] T. Tiegs, "SiC whisker reinforced alumina," in *Handbook of Ceramic Composites*, Boston, Kluwer Academic Publishers, 2005, pp. 307-325.
- [133] A. Aguilar-Elguezabal and M. Bocanegra-Bernal, "Alumina Toughened Zirconia Nanocomposite Incorporating Al₂O₃ Whiskers," *Internation Journal of Applied Ceramic Technology*, vol. 10, no. 2, pp. 215-223, 2013.
- [134] E. Holm and M. Cima, "Two-Dimensional Whisker Percolation in Ceramic Matrix Ceramic Whisker Composites," *Journal of the American Ceramic Society*, vol. 72, no. 2, pp. 303-305, 1989.
- [135] M. H. Bocanegra-Bernal, "Review: Hot Isostatic Pressing (HIP) technology and its applications to metals and ceramics," *Journal of Materials Science*, vol. 39, pp. 6399-6420, 2004.
- [136] J. M. Staehler, W. W. Predebon and B. J. Pletka, "Process for producing high strength alumina". USA/Michigan Patent 5443773, 22 August 1995.

- [137] F. Maglia, I. Tredici and U. Anselmi-Tamburini, "Properties and Densification of Bulk Nanocrystalline Functional Ceramics with Grain Size Below 50nm," *Journal of the European Ceramic Society*, vol. 33, pp. 1045-1066, 2013.
- [138] K. Bodisova and P. Sajgalik, "Two-Stage Sintering of Alumina with Submicrometer Grain Size," *Journal of the American Ceramic Society*, vol. 90, no. 1, pp. 330-332, 2007.
- [139] R. Gadow and F. Kern, "Pressureless Sintering of Mold Injected Zirconia Toughened Alumina Nanocomposites," *Journal of the Ceramic Society of Japan*, vol. 114, no. 11, pp. 958-962, 2006.
- [140] N. Loh and K. Sia, "An Overview of Hot Isostatic Pressing," *Journal of Materials Processing Technology*, vol. 30, pp. 45-65, 1992.
- [141] R. German, "Coarsening in Sintering: Grain Shape Distribution, Grain Size Distribution, and Grain Growth Kinetics in Solid-Pore Systems," *Critical Reviews in Solid State and Materials Science*, vol. 35, pp. 263-305, 2010.
- [142] J. Wang and R. Raj, "Activation Energy for the Sintering of Two-Phase Alumina/Zirconia Ceramics," *Journal of the American Ceramics Society*, vol. 74, no. 8, pp. 1959-1963, 1991.
- [143] G. Sarrafi-Nour and T. Coyle, "Temperature Dependence of Crack Wake Bridging Stresses in a SiC-Whisker-Reinforced Alumina," *Acta Materialia*, vol. 49, pp. 3553-3563, 2001.
- [144] D. Mohanty, "Thesis: Effect of holding time on binder burnout, density and strength of green and sintered alumina samples," National Institute of Technology Rourkela, Rourkela, 2011.
- [145] S. Masia, P. Calvert, W. Rhine and H. Bowen, "Effect of oxides on binder burnout during ceramics

- processing," *Journal of Materials Science*, vol. 24, pp. 1907-1912, 1989.
- [146] R. Higgins, "The chemistry of carbon retention during non-oxidative binder removal from ceramic greenware," Massachusetts Institute of Technology, Cambridge, 1990.
- [147] P. Johander and H.-J. Ritzhaupt-Kliesl, *Ceramics processing in microtechnology*, Boca Raton, FL: Whittles, 2009.
- [148] W. Rasband, "ImageJ2," U.S. National Institutes of Health, Bethesda, Maryland, 1997-2014.
- [149] U. Taffner, V. Carle, U. Schafer and M. Hoffmann, "Preparation and Microstructural Analysis of High-Performance Ceramics," in *ASM Handbook*, AMS International, 2004, pp. 1157-1166.
- [150] S. Palmqvist, "Indentation hardness and fracture toughness in single crystal," *Jernkontorets Ann*, vol. 141, pp. 300-306, 1957.
- [151] C. Ponton and R. Rawlings, "Vickers indentation fracture toughness test Part 1 Review of literature and formulation of standardised indentation toughness equations," *Materials Science and Technology*, vol. 5, no. 9, pp. 865-872, 1989.
- [152] A. Evans and E. Charles, "Fracture toughness determination by indentation," *Journal of the American Ceramics Society*, vol. 59, pp. 371-372, 1976.
- [153] J. Gong, "Determining Indentation Toughness by Incorporating True Hardness Into Fracture Mechanics Equations," *Journal of European Ceramic Society*, vol. 19, pp. 1585-1592, 1999.
- [154] G. Rance, D. Marsh, S. Bourne, T. Reade and A. Khlobystov, "van der Waals Interactions between Nanotubes and Nanoparticles for Controlled Assembly of Composite Nanostructures," *American*

Chemical Society Nano, vol. 4, no. 8, pp. 4920-4928, 2010.

- [155] R. Higgins, W. Rhine, M. Cima, H. Bowen and W. Farneth, "Ceramic Surface Reactions and Carbon Retention during Non-Oxidative Binder Removal by Al₂O₃/Poly (methyl methacrylate) at 20 - 700 C," *Journal of the American Ceramic Society*, vol. 77, no. 9, pp. 2243-2254, 1994.
- [156] G. Saada, "Hall-Petch revisited," *Materials Science and Engineering A*, vol. 400, pp. 146-149, 2005.
- [157] N. Miyahara, K. Yamaishi, Y. Mutoh, K. Uematsu and M. Inoue, "Effect of Grain Size on Strength and Fracture Toughness in Alumina," *Journal of the Japanese Society of Mechanical Engineers*, vol. 37, no. 3, pp. 231-237, 1994.
- [158] J. M. Rincon, T. R. Dinger, G. Thomas, J. S. Moya and M. I. Osendi, "Microstructure of mullite/ZrO₂ and mullite/Al₂O₃/ZrO₂ tough ceramic composites," *Acta metall*, vol. 35, no. 5, pp. 1175-1179, 1987.
- [159] K. Luthra and H. Park, "Oxidation of Silicon Carbide-Reinforced Oxide-Matrix Composites at 1375 to 1575 C," *Journal of the American Ceramic Society*, vol. 73, pp. 1014-1023, 1990.
- [160] P. Mogilevsky and A. Zangvil, "Kinetics of oxidation in oxide ceramic matrix composites," *Materials Science and Engineering A*, vol. 354, pp. 58-66, 2003.
- [161] S. Lakiza and L. Lopato, "Stable and Metastable Phase Relations in the System Alumina-Zirconia-Yttria," *Journal of the American Ceramic Society*, vol. 80, no. 4, pp. 893-902, 1997.
- [162] H. G. Scott, "Phase relationships in the zirconia-yttria system," *Journal of Materials Science*, vol. 10, pp. 1527-1535, 1975.

- [163] G. Quinn and R. Bradt, "On the Vickers Indentation Fracture Toughness Test," *Journal of the American Ceramic Society*, vol. 90, no. 3, pp. 673-680, 2007.
- [164] M. Abdullah, J. Ahmad, M. Mehmood, H. Waqas and M. Mujahid, "Effect of deflocculants on hardness and densification of YSZ-Al₂O₃ (whiskers & particulates) composites," *Composites: Part B*, vol. 43, pp. 1564-1569, 2012.
- [165] A. Nevarez-Rascon, A. Aguilar-Elguezabal, E. Orrantia and M. Bocanegra-Bernal, "Compressive strength, hardness and fracture toughness of Al₂O₃ whiskers reinforced ZTA and ATZ nanocomposites: Weibull analysis," *International Journal of Refractory Metals and Hard Materials*, vol. 29, pp. 333-340, 2011.
- [166] S. Ueno, T. Ohji and H. Lin, "Corrosion and recession of mullite in water vapour environment," *Journal of the European Ceramic Society*, vol. 28, no. 2, pp. 431-435, 2008.
- [167] J. Gao, Y. He and D. Wang, "Fabrication and high temperature oxidation resistance of ZrO₂/Al₂O₃ micro-laminated coatings on stainless steel," *Materials Chemistry and Physics*, vol. 123, no. 2-3, pp. 731-736, 2010.
- [168] N. Jacobson and K. Lee, "Corrosion of Mullite by Molten Salts," *Journal of the American Ceramic Society*, vol. 79, no. 8, pp. 2161-2167, 1996.
- [169] M. Schmucker, P. Mechnich, S. Zaefferer and H. Schneider, "Water vapor corrosion of mullite: Single crystals versus polycrystalline ceramics," *Journal of the European Ceramic Society*, vol. 28, no. 2, pp. 425-429, 2008.
- [170] R. Torrecillas, M. Schehl and L. Diaz, "Creep behaviour of alumina-mullite-zirconia nanocomposites

obtained by a colloidal processing route," *Journal of the European Ceramic Society*, vol. 27, pp. 4613-4621, 2007.

[171] I. Tsuji, S. Aoki, Y. Miyazaki, Y. Hara, Y. Furuse and S. Hamada, "Dense and near-net-shape fabrication of Si₃N₄ ceramics," in *ASME Turboexpo 91*, 1991.